



저작자표시-비영리-변경금지 2.0 대한민국

이용자는 아래의 조건을 따르는 경우에 한하여 자유롭게

- 이 저작물을 복제, 배포, 전송, 전시, 공연 및 방송할 수 있습니다.

다음과 같은 조건을 따라야 합니다:



저작자표시. 귀하는 원저작자를 표시하여야 합니다.



비영리. 귀하는 이 저작물을 영리 목적으로 이용할 수 없습니다.



변경금지. 귀하는 이 저작물을 개작, 변형 또는 가공할 수 없습니다.

- 귀하는, 이 저작물의 재이용이나 배포의 경우, 이 저작물에 적용된 이용허락조건을 명확하게 나타내어야 합니다.
- 저작권자로부터 별도의 허가를 받으면 이러한 조건들은 적용되지 않습니다.

저작권법에 따른 이용자의 권리는 위의 내용에 의하여 영향을 받지 않습니다.

이것은 [이용허락규약\(Legal Code\)](#)을 이해하기 쉽게 요약한 것입니다.

[Disclaimer](#)

공학박사학위논문

**ELECTROPLASTICITY  
IN LIGHTWEIGHT ALLOY**

경량 금속에서의 통전 소성 변형 및  
메커니즘 규명에 대한 연구

2016년 02월

서울대학교 대학원

재료공학부

김 문 조

# ELECTROPLSTICITY IN LIGHTWEIGHT ALLOY

경량 금속에서의 통전 소성 변형 및

메커니즘 규명에 대한 연구

지도교수 한 홍 남

이 논문을 공학박사학위논문으로 제출함  
2015년 12월

서울대학교 대학원  
재료공학부  
김 문 조

김문조의 박사학위논문을 인준함  
2015년 12월

위	원	장	<u>오 규 환</u> (인)
부	위	원	<u>한 홍 남</u> (인)
위		원	<u>박 은 수</u> (인)
위		원	<u>홍 성 태</u> (인)
위		원	<u>최 인 석</u> (인)



## **ABSTRACT**

Electrically-assisted forming is a promising alternative forming technique, in which the mechanical property of a metal alloy is altered by simply applying electricity to the target alloy during deformation. The reduced flow stress and increased ductility, which are often called the electroplastic effect, are generally observed in electrically-assisted deformation.

Even though a number of researches have been conducted on the effect of electric current on deformation, the amount of experimental data to clearly understand the phenomenon of electroplasticity is not sufficient yet. Also, the underlying mechanism of electroplasticity is still unclear. The objective of present study is mainly consisted of two part. Firstly, the effect of electric current on lightweight alloy is investigated based on microstructural perspective. Through the understanding of electric current-assisted phenomenon, finally, the underlying mechanism of electroplasticity is investigated.

Firstly, electroplasticity in non-heat treatable aluminum alloy was investigated with subsequent microstructural analysis. Al-Mg alloy was selected as non-heat treatable aluminum alloy. The elongation of both as-received (H32 treated) and cold-rolled specimens increases drastically with softening of flow stress by applying electric current during deformation.

Recrystallization and grain growth were observed after fracture from the pulsed tensile test and it could be expected that thermal effect would be dominant after severe necking. However, increase of formability before severe necking was still observed strongly and it could not be explained by usual thermal effect. It was confirmed that the recovery occurs at a given electric pulsing condition comparing with nonpulsed tensile test. This study proves that the electric current could induce annealing as a distinct role from Joule heating.

Secondly, electroplasticity in precipitation hardened aluminum alloy was investigated with subsequent microstructural analysis. Al-Mg-Si alloy was selected as precipitation hardened aluminum alloy. Specimens with three different heat treatment conditions, solution treated, naturally aged, and artificially aged (as-received) conditions, are prepared. In solution treated specimen, the elongation and flow stress increase by applying pulsed electric current during plastic deformation compared to the result of non-pulsed tension. The Portevin-Le Chaterlier (PLC) phenomenon, which is clearly observed in non-pulsed tensile test, nearly disappears by applying electric current during deformation. For the naturally aged specimen, the flow stress decreases while the elongation significantly increases under a pulsed electric current compared to the result of non-pulsed tensile test. In case of artificially aged specimen, both elongation and flow stress decrease under a pulsed electric current. From XRD analysis, it was observed that thermal and electric current-induced annealing occur in all the specimen under the electric current. Also, the

formation of early stage of precipitation from a supersaturated state might be accelerated by applying electric current with a distinct effect of Joule heating, which causes the increase of flow stress and the disappearance of PLC phenomenon in the solution treated specimen. In addition, the microstructural observation shows that electric current accelerates the formation of microvoid around the precipitates at grain boundary, which results in earlier fracture in the artificially aged specimen.

Lastly, underlying mechanism of electroplasticity was investigated based on effect of electric current on elastic modulus. From the results discussed in Al-Mg alloy and Al-Mg-Si alloy, it was suggested that electric current can enhance the atomic diffusion with a distinct effect of Joule heating. For diffusion, bonding energy of atoms with neighbors is an important factor to activate the diffusion. Bonding energy is closely related to the lattice potential energy. When material is excited by external energy, it will cause the changes in lattice potential energy. Elastic modulus is closely related to the atomic potential energy, which is derived from the second derivative of the potential energy-atomic distance curve. Therefore, the change in potential energy can be expected by measuring an elastic modulus. Laser ultrasonic method was used as a non-contact with high accuracy measuring technique to detect change in elastic modulus. For aluminum and magnesium alloy, electric current can induce additional decrease in elastic modulus more than Joule heating effect. Therefore, it can be suggested that electric current may induce the additional

change in lattice potential energy with a discrete effect of Joule heating, which can cause the enhance of diffusion by weakening the atomic bonding force. Also, effect of grain boundary on electric current ‘itself’ effect in electroplasticity was studied for each alloy with different grain size of specimen. It was confirmed that the decrease in elastic modulus by applying electric increases with increasing the fraction of grain boundary in both aluminum and magnesium alloy. From these results, it can be said that the grain boundary is dominantly influenced by applying electric current to decrease in elastic modulus.

This study provides an important insight to apply electric current-assisted forming. As a positive aspect, recovery occurs due to the electric current-induced annealing as well as the thermal one by applying electric current. This can enlarge the capacity for deformation. In addition, electric current-assisted aging occurs during deformation with less time and lower temperature compared to conventional aging. However, electric current can accelerate the formation of microvoid around the particles, which results in earlier fracture as a negative way in formability. Therefore, electric current should be carefully applied to material considering the microstructural features to obtain enhanced formability without degradation of mechanical property.

From this study, electroplasticity in lightweight alloy was investigated well. Also, the underlying mechanism of electroplasticity, which has not been clear up to now, is suggested. The discussion on electroplasticity and suggested

underlying mechanism can provide insight to apply electrically-assisted manufacturing in real industry as well as academic interests for electroplasticity.

**Keywords:** Lightweight alloy, Aluminum alloy, Magnesium alloy, Electrically-assisted manufacturing (EAM), Electroplasticity, Uniaxial tensile test, flow stress, elongation, Vickers hardness, Digital image correlation (DIC), Electron backscatter diffraction (EBSD), Scanning electron microscope (SEM), Transmission electron microscope (TEM), Focused ion beam (FIB), X-ray diffraction (XRD), Full width half maximum (FWHM), Laser ultrasonics, Dislocation, Annealing, Recovery, Recrystallization, Aging, Precipitation, Fracture, Void, Joule heating, Potential energy, Diffusion, Elastic modulus, Grain boundary.

**Student number:** 2010-20579

# Contents

<b>Abstract .....</b>	<b>I</b>
<b>Table of Contents .....</b>	<b>VI</b>
<b>List of Tables .....</b>	<b>XI</b>
<b>List of Figures .....</b>	<b>XII</b>

## Chapter 1

### Introduction

<b>1.1 Lightweight alloy.....</b>	<b>1</b>
<b>1.2 Electrically-assisted manufacturing (EAM).....</b>	<b>3</b>
<b>1.3 Electroplasticity.....</b>	<b>7</b>
<b>1.4 Thesis motivation.....</b>	<b>10</b>
<b>1.5 References .....</b>	<b>12</b>

## **Chapter 2**

### **Electroplasticity in non-heat treatable aluminum alloy**

#### **(Al-Mg alloy)**

<b>2.1 Introduction</b> .....	16
<b>2.2 Experimental procedures</b> .....	18
2.2.1 Specimen preparation .....	18
2.2.2 Experimental set-up .....	20
2.2.3 Microstructural observation .....	23
<b>2.3 Effect of electric current on mechanical behavior and microstructure</b> .....	24
2.3.1 Electroplasticity in as-received specimen .....	24
2.3.2 Electroplasticity in cold-rolled specimen .....	30
<b>2.4 Electric current-induced annealing</b> .....	34
<b>2.5 Summary</b> .....	44
<b>2.6 References</b> .....	46

## **Chapter 3**

### **Electroplasticity in precipitation-hardened aluminum alloy (Al-Mg-Si alloy)**

<b>3.1 Introduction</b> .....	48
<b>3.2 Experimental procedures</b> .....	49
3.2.1 Specimen preparation .....	49
3.2.2 Experimental set-up .....	52
3.2.3 Microstructural observation .....	54
<b>3.3 Basic properties: Mechanical behavior and microstructure</b> .....	56
3.3.1 Mechanical behavior .....	56
3.3.2 Microstructure .....	58
<b>3.4 Effect of electric current on uniaxial quasi-static tensile behavior</b> .....	63
<b>3.5 Annealing during pulsed tension</b> .....	73

<b>3.6 Effect of electric current on fracture behavior</b> .....	80
<b>3.7 Summary</b> .....	85
<b>3.8 References</b> .....	87

## **Chapter 4**

### **A study on underlying mechanism of electroplasticity**

<b>4.1 Introduction</b> .....	89
<b>4.2 Motivation</b> .....	91
4.2.1 Diffusion kinetics .....	91
4.2.2 Measurement of elastic modulus using a laser based ultrasonic technique .....	98
<b>4.3 Experimental procedures</b> .....	102
4.3.1 Specimen preparation .....	102
4.3.2 Experimental set-up .....	103
<b>4.4 Effect of electric current on elastic modulus</b> .....	106

4.4.1 Temperature dependence on elastic modulus.....	106
4.4.2 Electric current ‘itself’ effect in electroplasticity.....	111
<b>4.5 Origin of decrease in elastic modulus in electroplasticity...</b>	<b>119</b>
4.5.1 Grain boundary and elastic modulus.....	119
4.5.2 Effect of grain boundary on temperature dependence on elastic modulus.....	124
4.5.3 Electric current ‘itself’ effect in electroplasticity under the different grain size.....	127
4.5.4 Effect of grain boundary in electroplasticity.....	132
<b>4.6 Summary .....</b>	<b>136</b>
<b>4.7 References .....</b>	<b>139</b>
<b>Chapter 5</b>	
<b>Total conclusion.....</b>	<b>141</b>

## **LIST OF TABLES**

Table 2.1 Chemical composition of Al-Mg alloy (in wt.%).

Table 3.1 Chemical composition of Al-Mg-Si alloy (in wt.%).

Table 4. 1 Linear relationship of temperature dependence on elastic modulus  
in literature.

Table 4. 2 Volume fraction of grain boundary and matrix.

Table 4. 3 Linear relationship of temperature dependence on elastic modulus of  
Al50, Al100, Mg07 and Mg344.

## LIST OF FIGURES

Figure 1. 1 Conventional hot forming process and electrically-assisted manufacturing process.

Figure 2. 1 (a) Instrumental set-up and (b) pulsing pattern during uniaxial tensile test. Selective pulsing pattern ( $\rho_0 = 110 \text{ A/mm}^2$ ,  $t_d=0.5 \text{ sec}$ ,  $t_p=30 \text{ sec}$ ) was applied to the specimen periodically until fracture. Constant value of electric current was applied during deformation.

Figure 2. 2 Engineering stress-strain curves of nonpulsed (in black)/pulsed (in red) tensile test and measured temperature as a function of engineering strain (in blue) on the as-received specimen.

Figure 2. 3 Inverse pole figure LD(//RD) maps of as-received specimen (a) before tension, (b) after fracture from nonpulsed tension, (c) unloaded right before necking (at engineering strain of 16.4%) from pulsed tension and (d) after fracture from pulsed tension.

Figure 2. 4 Inverse pole figure LD maps of cross sectional area (a) before tensile, (b) at center of the specimen at engineering strain of 16.4%, (c) at side of the specimen at engineering strain of 16.4% and (d) snap shot of specimen during pulsed tensile test from DIC measurement at engineering strain of 16.4%, when necking starts.

Figure 2. 5 Engineering stress-strain curves of nonpulsed (in black)/pulsed (in red) tensile test on 30% cold-rolled specimen.

Figure 2. 6 Inverse pole figure LD ( $\parallel$ RD) maps of 30% cold rolled specimen (a) before tension, (b) after fracture from nonpulsed tension and (c) after fracture from pulsed tension.

Figure 2. 7 (a) Average temperature history for total gauge section by IR camera (in red) and (b) local temperature history by thermocouple (in red) and corresponding heat treatment (in green) using induction heating system.

Figure 2. 8 Inverse pole figure LD maps of cross sectional area at (a) center and

(b) side of the specimen at engineering strain of 5% from nonpulsed tension.

Figure 2. 9 Inverse pole figure LD maps of cross sectional area at (a) center and

(b) side of the specimen at engineering strain of 5% from pulsed tension.

Figure 2. 10 Vickers hardness of as-received specimen, deformed specimens

unloaded at engineering of 5% after nonpulsed/pulsed tension and heat treated

specimen based on temperature history of total gauge section.

Figure 2. 11 Full width and half maximum profiles (symbols, left-axis) and X-

ray diffraction patterns (lines, right-axis) in the range of 35-80°.

Figure 2. 12 Dark field images of specimens from (a) nonpulsed and (b) pulsed

tensile test unloaded at engineering strain of 5%.

Figure 3.1 Three types of specimens based on different heat treatments.

Figure 3. 2 Pulsing pattern during uniaxial tensile test. Selective pulsing pattern

( $\rho_0 = 90 \text{ A/mm}^2$ ,  $t_d=0.5 \text{ sec}$ ,  $t_p=30 \text{ sec}$ ) was applied to the specimen during

plastic deformation after yielding. Constant value of electric current was applied during deformation.

Figure 3. 3 (a) Engineering stress-strain curves and (b) Vickers hardness of Al-Mg-Si alloy for artificially aged, naturally aged and solution treated specimens.

Figure 3. 4 Inverse pole figure (ND) maps of (a) naturally aged and (b) artificially aged specimens. High angle misorientation over  $10^\circ$  is marked as black lines for grain identification. The grain sizes of naturally aged and as-received specimens were 67 and 69  $\mu\text{m}$ , respectively.

Figure 3. 5 TEM bright field image of needle-shaped  $\beta''$  phase in the grain interior including [001] selected area diffraction pattern in artificially aged specimen before uniaxial tension.

Figure 3. 6 (a) TEM bright field image of coarse intermetallic compound at the grain boundary and (b) EDX spectrums on the intermetallic compounds in artificially aged specimen before uniaxial tension.

Figure 3. 7 Engineering stress-strain curves without (black curve) and with (red curve) applying electric current of (a) solution treated, (b) naturally aged and (c) artificially aged Al-Mg-Si alloy. The temperature due to Joule heating was shown below the stress-strain curve as a function of engineering strain (blue curve, right-axis).

Figure 3. 8 The magnified versions of region 1 and 2 in Figure 3. 7 (a) for the observation of serrated flow in solution treated specimen.

Figure 3. 9 (a) Temperature histories by Joule heating during pulsed tension (in red), furnace heat treatment (in green) and induction heat treatment (in blue) and (b) Vickers hardness (HV) of solution treated specimen at engineering strain of 17% from nonpulsed and pulsed tension and after each heat treatment using specimen strained to 17% from nonpulsed tension.

Figure 3. 10 Example of XRD peaks for three case: before tension, tension with/without applying electric current at engineering strain of 14% for solution

treated specimen ((110) diffraction peak) as an normalized diffraction angle ( $2\theta$ , deg). The measured data (symbol) is fitted with Pearson VII function (line).

Figure 3. 11 FWHM profiles of solution treated specimen unloaded at engineering strain of (a) 6% and (b) 14%.

Figure 3. 12 FWHM profiles of naturally aged specimen unloaded at engineering strain of (a) 6% and (b) 14%.

Figure 3. 13 FWHM profiles of artificially aged specimen unloaded at engineering strain of 6%.

Figure 3. 14 Fracture surface after nonpulsed and pulsed tension for solution treated, naturally aged and artificially aged specimens.

Figure 3. 15 Microstructure near fracture surface of artificially aged specimen after pulsed tension: SEM images showing the microvoid (a) along grain boundary and (b) around precipitations.

Figure 3. 16 (a) Sampling region of artificially aged specimen after pulsed tension for TEM observation using FIB and (b) bright field image of microvoid around precipitations.

Figure 4.1 Activation energy for diffusion.

Figure 4. 2 A typical potential well indicating forces and bonding energy.

Figure 4. 3 Elastic rod whose length is much greater than its cross-sectional dimension.

Figure 4. 4 Instrumental set-up for laser based ultrasonic with applying electric current.

Figure 4. 5 Inverse pole figure ND map of (a) Al50 (grain size:  $50 \pm 17 \mu\text{m}$ ) and (b) Mg07 (grain size:  $7 \pm 3 \mu\text{m}$ ) based on critical misorientation angle of  $10^\circ$ .

Figure 4. 6 Temperature dependence on elastic modulus of (a) Al50 and (b)

Mg07.

Figure 4. 7 Rise time of electric current to target value under the various electric current condition.

Figure 4. 8 Measured elastic modulus (in blue triangle, left-axis) and calculated elastic modulus due to Joule heating (in red circle, left-axis) with measured temperature (in red rod, right-axis) under the various electric current density for Al50 specimen.

Figure 4. 9 Measured elastic modulus (in blue triangle, left-axis) and calculated elastic modulus due to Joule heating (in red circle, left-axis) with measured temperature (in red rod, right-axis) under the various measuring position at fixed electric current density of  $250 \text{ A/mm}^2$  for aluminum alloy.

Figure 4. 10 Measured elastic modulus (in blue triangle, left-axis) and calculated elastic modulus due to Joule heating (in red circle, left-axis) with measured temperature (in red rod, right-axis) under the various electric current

density for Mg07 specimen.

Figure 4. 11 Inverse pole figure ND map of (a) Al100 (grain size:  $100 \pm 36$   $\mu\text{m}$ ) and (b) Mg344 (grain size:  $344 \pm 112$   $\mu\text{m}$ ) based on critical misorientation angle of  $10^\circ$ .

Figure 4. 12 A simple model of specimen for calculating  $f_{gb}$  and  $f_m$  ( $f_{gb}$ : volume fraction of grain boundary,  $f_m$ : volume fraction of matrix).

Figure 4. 13 Temperature dependence on elastic modulus of (a) Al50, Al100 and (b) Mg07, Mg344.

Figure 4. 14 Measured elastic modulus (in blue triangle, left-axis) and calculated elastic modulus due to Joule heating (in red circle, left-axis) with measured temperature (in red rod, right-axis) under the various electric current density for Al100 specimen.

Figure 4. 15 Measured elastic modulus (in blue triangle, left-axis) and

calculated elastic modulus due to Joule heating (in red circle, left-axis) with measured temperature (in red rod, right-axis) under the various electric current density for Mg344 specimen.

Figure 4. 16 Normalized elastic modulus of Al50 and Al100. The measured values (Al50 : ▲, Al100 : ⊙) and the calculated values due to Joule heating (Al50 : ▲, Al100 : ●) are represented.

Figure 4. 17 Normalized elastic modulus of Mg07 and Mg344. The measured values (Mg07 : ▲, Mg344 : ⊙) and the calculated values due to Joule heating (Mg07 : ▲, Mg344 : ●) are represented.

# Chapter 1

## Introduction

### 1.1 Lightweight alloy

Aluminum and magnesium alloy have the potential as representative lightweight alloy to play a significant enabling role in future energy savings across a wide range of applications, including transportation, power production, industrial processing, and structures (U.S. Geological Survey, 2013). Especially in automotive industry, the high strength-to-weight ratio of these metals means that their use in automotive industry produces more fuel efficient vehicles with no reduction in performance or safety. Under the stringent legislative regulations on CO<sub>2</sub> emissions globally, a reduction of vehicle mass is mandatory as the most effective measures to reduce CO<sub>2</sub> considering that 100 kg saved on the mass of a car can save about 9 grams of CO<sub>2</sub> per kilometer (Cheah, 2010).

By light-weighting with aluminum alloy, weight savings of parts up to 50% can be achieved. Full aluminum bodies allow weight saving of 70 to 140 kg (i.e. 30–40%) depending on the size of the car (Hirsch, 2011). In case of magnesium alloy, it is 35% less dense than aluminum alloy and 75% lighter than steel components. It is also easier to manufacture, having a lower latent heat, and

being easier to machine (Kulekci, 2008).

Despite of a growing effort to application of lightweight alloy to automotive component, however, the commercial applications of aluminum and magnesium alloy are still limited due to their poor formability at room temperature compared with conventional ferrous alloys (Kahn and Liu, 2012; Klusemann *et al.*, 2015; Pogatscher *et al.*, 2013).

## **1.2 Electrically-assisted manufacturing (EAM)**

Forming at elevated temperature is an effective method to counter the poor formability of aluminum and magnesium alloy. Warm and hot forming have been generally conducted at elevated temperature up to the recrystallization temperature with the range of 200-350 °C. However, heating strategies to increase forming temperature may cause inhomogeneous thermal distribution on the material, surface oxidation and adhesion between the die and the alloy sheet (Toros *et al.*, 2008; Hirsch, 2013). Hydroforming and incremental forming process also have been investigated to be applied to forming of aluminum alloy sheets. The hydroforming process makes it possible to manufacture a complex shape with fewer components leading cost-saving (Hartl, 2005). Incremental forming process is a flexible process in which wide range of shapes can be formed by a progression of localized deformation (Ambrogio *et al.*, 2012; Nimbalkar and Nandedkar, 2013). However, these forming processes require excessive time and high cost of initial capital investment. Therefore, a new forming method, which can increase the formability of lightweight alloys at relatively low forming temperature comparing with warm and hot forming without excessive time and capital investment, is still desired.

Electrically-assisted forming is a promising alternative forming technique, in which the mechanical property of a metal alloy is altered by simply applying

electricity to alloys during deformation. The reduced flow stress and increased ductility, which are often called the electroplastic effect, are generally observed in electrically-assisted deformation (Troitskii, 1969; Conrad, 2000; Salandro *et al.*, 2010).

By comparing with conventional hot forming process, electrically-assisted manufacturing has a lot of advantages. For conventional hot forming process, it needs large area for heating furnace, while electrically-assisted manufacturing needs relatively small space for power supply as shown in Figure 1. 1. Also, conventional hot forming process needs excess time to heat up the furnace and forming sheet with additional excess energy to maintain the temperature of the furnace and mold. However, electrically-assisted manufacturing can heat up the sheet with a rapid heating with no need to maintain temperature of furnace and mold. Therefore, it is possible to save the cost in space and energy by applying electrically-assisted manufacturing than conventional hot forming process.

Using these beneficial effects of electrically-assisted deformation, the effect of electric current on mechanical behavior has been studied actively for practical use in industries. It was reported that manufacturing process can be enhanced by reducing forming load and/or increasing formability in bending (Salandro *et al.*, 2011; Jordan and Kinsey, 2012), blanking (Kim *et al.*, 2014c), drawing (Zimniak *et al.*, 2008; Wang, 2009) and forging (Perkins *et al.*, 0007; Hong *et al.*, 2015). It was also reported that the springback during sheet metal

forming can be effectively reduced by applying electric current during process  
(Green *et al.*, 2009; Kim *et al.*, 2014b).

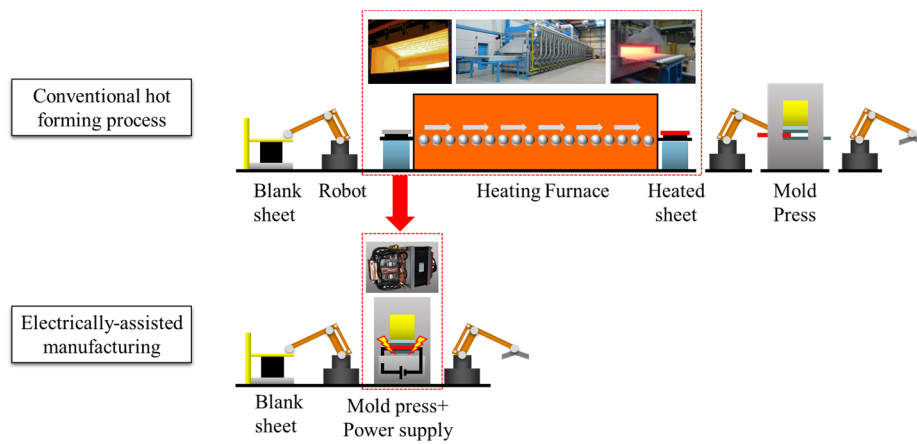


Figure 1. 1 Conventional hot forming process and electrically-assisted manufacturing process.

### 1.3 Electroplasticity

A possible influence of electric current on mechanical behavior was indicated for the first time by Machlin in 1959 (Machlin, 1959). According to Machlin (1959), applying an electric current showed a significant effect on flow stress, ductility and yield strength of group 1A salt (NaCl). Troitskii also reported that a pulsed electric current reduced the flow stress of zinc, tin, lead, and indium alloy.

In early researches to improve formability of metal alloys by applying an electric current during deformation, the electric current was generally applied continuously. According to Ross *et al.* (2007), Perkins *et al.* (2007) and Andrawes *et al.* (2007), the flow stress decreased with the presence of a continuous electric current during plastic deformation of aluminum, brass, copper, titanium alloys and stainless steel. However, a continuous electric current during tension generally lead to earlier fracture due to the local heating in neck of specimen.

To overcome the disadvantage of reduced elongation under a continuous electric current, applying a pulsed electric current during deformation has been considered. Roth *et al.* (2008) applied a pulsed electric current to aluminum 5754 alloy during tension and achieved elongation close to 400% of the gauge length. Effect of pulse duration and current density was investigated to reliably achieve the optimal specimen elongation (Salandro *et al.*, 2009). Salandro *et al.*

(2010) also investigated the effect of pulsed electric current on the mechanical behavior of tensile specimens of aluminum 5xxx alloys with different heat treatments.

Based on the positive effects of electric current on the plastic deformation, efforts have been also made to quantify the effect of electric current on mechanical behavior. Kronenberger *et al.* (2009) developed a finite element analysis model for aluminum 6061 alloy in compression. The model can accurately predict the temperature rise due to resistive heating during an electrical compression test. However, the reduction of flow stress under an electric current may not be fully demonstrated by considering only the effect of resistive heating. To account for the additional effect caused by applying electric current, the electroplastic effect coefficient was introduced (Bunget *et al.*, 2010). For the electrically-assisted tension (Bunget *et al.*, 2010) and bending (Salandro *et al.*, 2011) of metal alloys, closed-form solutions including electroplastic coefficients were suggested to describe the stress and strain during deformation with different electric current parameters and the performance of each model was evaluated based on experimental results. Recently, an empirical expression to describe the contour of tensile behavior of aluminum 5052 alloy under a pulsed electric current was also suggested (Roh *et al.*, 2014). In the empirical expression, electroplastic coefficients were introduced to account for the electric current effect of given material and electric current parameters. In the study of Hariharan *et al.* (2015), electro-

thermo-mechanical finite element study was conducted by decoupling the thermal effect from pulsed tensile behavior and the electric current affecting the mechanical behavior was quantified.

Based on the positive effects of electric current on the plastic deformation, some researchers have examined the effect of electric current on the mechanical behavior based on microstructural observations. Heigel *et al.* (2005) found that electric current affects the number and size of precipitates of Al-Mg-Si alloy. The relationships between grain size and reduction of flow stress under an electric current also have been investigated (Siopis and Kinsey, 2010; Fan *et al.*, 2013). In addition, Kim *et al.* (2014a) observed the annihilation of dislocation by applying a pulsed electric current during uniaxial tension. According to Kim *et al.* (2014a), electric current-induced annealing occurs due to the annihilation of dislocation with a distinct role from joule heating.

## 1.4 Thesis motivation

Various theories have been suggested to explain the mechanism of electroplasticity. In some cases, the mechanical behavior under an electric current may be nicely described based on thermal effect caused by resistive heating without considering the electroplasticity theory (Goldman *et al.*, 1981; Klimov *et al.*, 1984; Magargee *et al.*, 2013). However, it also has been reported that the mechanical behavior under an electric current may not be clearly explained without considering the athermal electroplastic effect. A popular hypothesis to explain athermal effect of electroplasticity is the electron wind effect (Sprecher *et al.*, 1986; Conrad, 2000b; Antolovich *et al.*, 2004). In this hypothesis, the electric current density over  $10^{4-6}$  A/mm<sup>2</sup> may cause atoms to move, which results in interaction between electrons and dislocations. However, the underlying material mechanism associated with electroplasticity still remains controversial.

Even though a number of researches have been conducted on the effect of electric current on deformation, the amount of experimental data to clearly understand the phenomenon of electroplasticity is not sufficient yet. Also, the underlying mechanism of electroplasticity is still unclear. The objective of present study is mainly consisted of two part. Firstly, the effect of electric current on lightweight alloy is investigated based on microstructural analysis. Two kinds of alloy system are selected, which are Al-Mg alloy as a non-heat

treatable alloy system and Al-Mg-Si alloy as a representative age hardening alloy system. Based on understanding of electric current-assisted phenomenon, finally, the underlying mechanism of electroplasticity is investigated. It can be expected that this study can provide insight to apply electrically-assisted manufacturing in real industry as well as academic interests for electroplasticity.

## 1.5 References

- Ambrogio, G., Filice, L., Gagliardi, F., *Mater. Des.* 34 (2012) 501.
- Andrawes, J.S., Kronenberger, T.J., Perkins, T.A., Roth, J.T., Warley, R.L., *Mater. Manuf. Proc.* 22 (2007) 91.
- Antolovich, S.D., Conrad, H., *Mater. Manuf. Proc.* 19 (2004) 587.
- Bunget, C., Salandro, W., Mears, L., Roth, J. T., *Trans. North Am. Manuf. Res. Inst. SME* 38 (2010) 647.
- Cheah, L. W., Ph.D. Thesis, Massachusetts Institute of Technology, (2010).
- Conrad, H., *Mater. Sci. Eng. A* 287 (2000) 276..
- Demir, H., Gündüz, S., *Mater. Des.* 30 (2009) 1480.
- Donati, L., Segatori, A., Mehtedi, M.E., Tomesani, L., *Int. J. Plast.* 46 (2012) 70.
- Dutta, I., Allen, S.M., *J. Mater. Sic. Lett.* 10 (1991) 323.
- Fan, R., Magargee, J., Hu, P., Cao, J., *Mater. Sci. Eng. A* 574 (2013) 218.
- Goldman, P.D., Motowidlo, L.R., Galligan, J.M, *Scr. Metall.* 15 (1981) 353.
- Green, C. R., McNeal, T. A., Roth, J. T., *Trans. North Am. Manuf. Res. Inst. SME* 37 (2009) 403.
- Hariharan, K., Lee, M.-G., Kim, M.-J., Han, H.N., Kim, D., Choi, S., *Metall. Mater. Trans. A* 46 (2015) 3043.
- Hartl, C., *J. Mater. Process. Tech.* 167 (2005) 383.
- Heigel, J.C., Andrawes, J.S., Roth, J.T., *Trans. North Am. Manuf. Res. Inst. SME.* 33 (2005) 145.

- Hirsch, J., *Acta Mater.* 61 (2013) 818.
- Hirsch, J., *Mater. Trans A.*, 52 (2011) 818.
- Hong, S.-T., Jeong, Y.-H., Chowdhury, M.N., Chun, D.-M., Kim, M.-J., Han, H.N., *CIRP Annals Manuf. Tech.*, 64 (2015) 277.
- Jobba, M., Mishra, R.K., Niewczas, M., *Int. J. Plast.*, 65 (2015) 43.
- Jordan, A., and Kinsey, B.L., *Proceedings of the 7th International Conference on Micro Manufacturing (ICOMM 2012)*, Evanston, IL, March 12–14 (2012) 254.
- Khan, A.S., Liu, H., *Int. J. Plast.* 36 (2012) 1.
- Khan, A.S., Liu, H., *Int. J. Plast.* 36 (2012) 1.
- Kim, M.-J., Han, H.N., Lee, K.H., Oh, K.H., Lee, W.-B., Choi, I.-S., Hong, S.-T., *Scr. Mater.* 75 (2014a) 58.
- Kim, M.-S., Vinh, N.T., Yu, H.-H., Hong, S.-T., Lee, H.-W., Kim, M.-J., Han, H.N., *Int. J. Precis. Eng. Manuf.* 15 (2014b) 1207.
- Kim, W., Yeom, K.-H., Thien, N.T., Hong, S.-T., Min, B.-K., Ik Oh, S., Kim, M.-J., Han, H.N., Lee, H.-W., *CIRP Annals Manuf. Tech.* 63 (2014c) 273.
- Klimov, K.M., Novikov, I.I., *Strength Mater.* 16 (1984) 270.
- Klusemann, B., Fischer, G., Böhlke, T., Svendsen, B., *Int. J. Plast.* 67 (2015) 192.
- Klusemann, B., Fischer, G., Böhlke, T., Svendsen, B., *Int. J. Plast.* 67 (2015) 192.
- Kronenberger, T. J., Johnson, D.H., Roth, J.T., *J. Manuf. Sci. Eng.* 131 (2009) 031003-1-8.

- Kulekci, M.K., *Int. J. Adv. Manuf. Technol.* 39 (2008) 851.
- Machlin, E.S., *J. Appl. Phys.* 30 (1959) 1109.
- Magargee, J., Morestin, F., Cao, J., *ASME J. Eng. Mater. Technol.* 135 (2013) 041003-1-10.
- Nimbalkar, D.H., Nandedkar, V.M., *Int. J. Eng. Res. App.* 3 (2013) 39.
- Ozturk, F., Sisman, A., Toros, S., Kilic, S., Picu, R.C., *Mater. Des.* 31 (2010) 972.
- Perkins, T. A., Kronenberger, T.J., Roth, J.T., *J. Manuf. Sci. E-Trans. ASME.* 129 (2007) 84.
- Pogatscher, S., Antrekowitsch, Leitner, H., Sologubenko, A.S., Uggowitzerd, P.J., *Scr. Mater.* 68 (2013) 158.
- Pogatscher, S., Antrekowitsch, Leitner, H., Sologubenko, A.S., Uggowitzerd, P.J., *Scr. Mater.* 68 (2013) 158.
- Roh, J.-H., Seo, J.-J., Hong, S.-T., Kim, M.-J., Han, H.N., *Int. J. Plast.* 58 (2014) 84.
- Ross, C.D., Irvin, D.B., Roth, J.T., *J. Manuf. Sci. E-Trans. ASME.* 129 (2007) 342.
- Roth, J.T., Loker, I., Mauck, D., Warner, M., Golovashchenko, S.F., Krause, A., *Trans. NAMRI/SME.* 36 (2008) 405.
- Salandro, W.A., Bunget, C., Mears, L., *J. Manuf. Sci. E-Trans. ASME* 133 (2011) 041008-1-10.
- Salandro, W.A., Jones, J.J., McNeal, T.A., Roth, J.T., Hong, S.-T., Smith, M.T., *J. Manuf. Sci. E-Trans. ASME.* 132 (2010) 051016-1-11.

- Salandro, W.A., Khalifa, A., Roth, J.T., *Trans. NAMRI/SME*. 37 (2009) 387.
- Siopis, M.S., Kinsey, B.L., *ASME J. Manuf. Sci. Eng.* 132 (2010) 021004-1-7.
- Spitsyn, V.I., Troitskii, O.A., *Dokl. Akad. Nauk. S.S.S.R. Ser. Metallic.* 216 (1974) 1266.
- Sprecher, A.F., Mannan, S.L., Conrad, H., *Acta Metall.* 34 (1986) 1145.
- Stachenko, V.I., Troitskii, O.A., *Fiz. Met. Metalloved.* 53 (1982) 180.
- Stachenko, V.I., Troitskii, O.A., Spitsyn, V.I., *Phys. Status. Solidi. A* 79 (1983) 549.
- Toros, S., Ozturk, F., Kacar, I., *J. Mater. Process. Tech.* 207 (2008) 1.
- Troitskii, O.A., *Pis'ma Zhurn. Experim. Teoret. Fiz.* 10 (1969) 18.
- U.S. Geological Survey, *Mineral Commodity Summaries*, E. Lee Bray, 2013.
- Wang, S.N., Master thesis, Tshihua University, Beijing, China (2009).
- Zimniak, Z., Radkiewicz, G., *Arch. Civ. Mech. Eng.* 8 (2008) 173.

## **Chapter 2**

# **Electroplasticity in non-heat treatable aluminum alloy (Al-Mg alloy)**

### **2.1 Introduction**

Recently, industry have consistently attempted to improve fuel efficiency. The use of light materials such as aluminum alloys is one way to satisfy this requirement. However, the commercial application of aluminum alloys is still restricted because of their poor formability compared with conventional ferrous alloys (Pogatscher et al., 2013; Kim *et al.*, 2012). In order to overcome this drawback, hot or warm forming and incremental forming have frequently been considered. However, the elevated-temperature forming methods have significant drawbacks, such as the adhesion between the die and the metal, surface oxidation and the thermal gradient of materials (Miller *et al.*, 2000; Toros *et al.*, 2008).

Electrically assisted forming is a promising alternative technique, in which the mechanical property of a metal can be modified by simply applying electricity to the metal during deformation. It is known that applying an electric current through a metal can enhance plastic deformation (often called

“electroplasticity”) by reducing the flow stress and increasing the ductility (Conrad *et al.*, 2000; Salandro *et al.*, 2010). However, the underlying material mechanism associated with electroplasticity remains unclear. Although various possibilities, such as thermal effects due to Joule heating (Goldman *et al.*, 1981; Li *et al.*, 2012; Jones *et al.*, 2013), electron wind (Xu *et al.*, 1988; Troitskii *et al.*, 1984; Conrad, 2002; Andrawes *et al.*, 2007) and electrostatic field (Conrad *et al.*, 1989; Lu *et al.*, 1992, Miaoquan *et al.*, 1998), have been suggested, only a few studies have focused on microstructural observation with regard to the combined electrical and mechanical loading (Salandro *et al.*, 2010; Fan *et al.*, 2013, Roh *et al.*, 2013) to elucidate the mechanism of electroplasticity.

In the present work, electric current effects on the mechanical behavior of Al-Mg alloy, which is a non-heat treatable alloy system, was investigated from a microstructural perspective. The microstructural observations of the specimens from a nonpulsed/pulsed tensile test were performed using electron backscatter diffraction (EBSD), X-ray diffraction (XRD) and transmission electron microscopy (TEM). The deformation behavior associated with electroplasticity was then discussed based on the microstructural changes of the specimens.

## **2.2 Experimental procedures**

### **2.2.1 Specimen preparation**

A commercial Al-Mg alloy (Al-2.5Mg in wt.%) sheet in H32 treated state (as-received) was selected. For cold rolled specimen, cold rolling operation is used to reduce the thickness of a sheet 4 mm down to 3.2 mm in a reversing two-high mill. Tensile specimens with a thickness of 2 mm, a gauge width of 9 mm and a gauge length of 50 mm were prepared along the rolling direction of the sheet which is parallel to the loading direction (LD).

<i>Al</i>	<i>Mg</i>	<i>Cr</i>	<i>Si</i>	<i>Fe</i>
95.7	2.2-2.8	0.15-0.35	Max 0.25	Max 0.4

Table 2.1 Chemical composition of Al-Mg alloy (in wt.%)

### 2.2.2 Experimental set-up

The quasi-static uniaxial tensile test was conducted using the experimental set-up described in Figure 2. 1 (a) with a constant crosshead speed of 2.5 mm/min (corresponding to the initial strain rate of 0.05/min) at room temperature. The universal testing machine was insulated by inserting insulation made of bakelite between the grip and the crosshead of the machine to apply electric current only to the specimen during testing.

The displacement of the specimen was measured by ARAMIS Digital Image Correlation (DIC) system (GOM, Germany), which provides a non-contact measurement technique based on the principle of digital image correlation. The DIC system was calibrated using an extensometer during a tensile test without electric current. A stochastic black spot pattern in a white background was applied on one side of the tensile specimen for digital image correlation. The load history during a tensile test was measured using a 100 kN load cell (INSTRON, USA) attached to the universal testing machine and linked to ARAMIS system.

For a tensile test with a pulsed electric current, electric current was generated by a Vadal SP-1000U DC power supply (Hyosung, South Korea). During the test, the specimen was periodically pulsed with a constant amplitude of electric current over a selected duration while the specimen was continuously deformed by tensile displacement as schematically shown in Figure 2. 1 (b). The amplitude of electric current was selected to induce the electric current

density of  $110 \text{ A/mm}^2$  based on the initial cross sectional area of the specimen. Note that the first electrical pulse was applied right before the movement of the cross-head for all tests under a pulsed electric current. Electric current was periodically applied to the specimen with a duration ( $t_d$ ) of 0.5 sec and a period ( $t_p$ ) of 30 sec until fracture as schematically shown in Figure. 2. 1b.

Temperature of a specimen during a tensile test with a pulsed electric current was measured using both a k-type thermocouple attached at 20 mm above the center of the specimen and a FLIR-E40 infra-red (IR) thermal imaging camera (FLIR, Sweden). The other side of the specimen was sprayed with black thermal paint to stabilize the emissivity and thus to improve the accuracy of temperature measurement. The emissivity was calibrated by comparing the measured temperature using a K-type thermocouple.

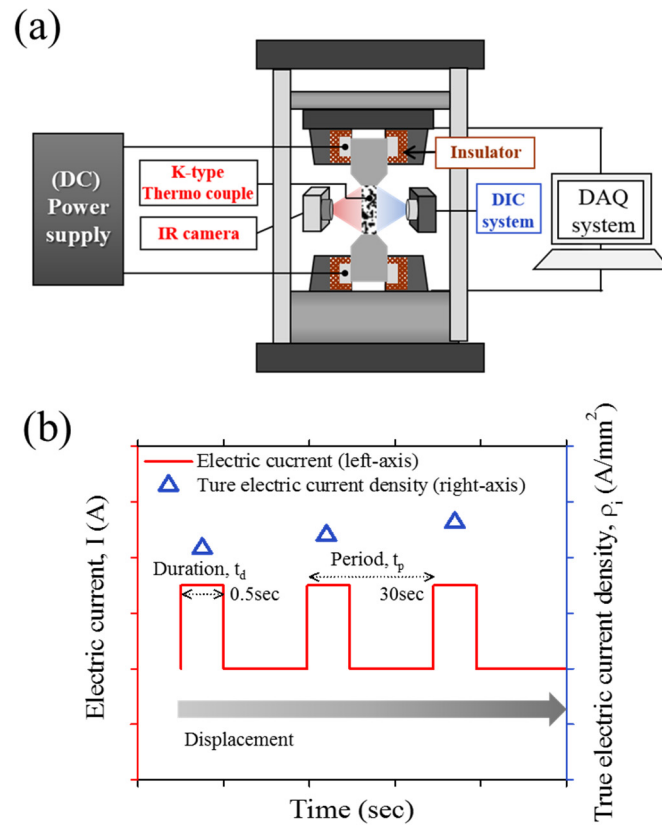


Figure 2. 1 (a) Instrumental set-up and (b) pulsing pattern during uniaxial tensile test. Selective pulsing pattern ( $\rho_0 = 110 \text{ A/mm}^2$ ,  $t_d=0.5 \text{ sec}$ ,  $t_p=30 \text{ sec}$ ) was applied to the specimen periodically until fracture. Constant value of electric current was applied during deformation.

### 2.2.3 Microstructural observation

The specimens for microstructural analysis were prepared perpendicular to the normal direction (ND). All microstructures were observed at the center of the specimen in terms of gage length. The crystallographic orientation maps were obtained using an EBSD (Oxford Instruments/HKL Nordlys Channel 5). Specimens were prepared by a standard metallographic grinding and polishing procedure, finishing with 1  $\mu\text{m}$  diamond suspension followed by electropolishing with a 10% perchloric acid. The EBSD scan step size was 1  $\mu\text{m}$  and the critical misorientation angle in the sample was confirmed as  $10^\circ$  for grain identification.

To check the change of dislocation density during the electrically-assisted deformation, the full width at half maximum (FWHM) of the diffraction peak was measured from XRD (BRUKER MILLER Co./D8-ADVANCED) using  $\text{CuK}\alpha$  radiation ( $\lambda = 0.15406 \text{ nm}$ ) operating at 40 kV. The diffraction peaks could be fit well with Pearson VII function. For the direct observation of dislocation by TEM, thin foils of pulsed and nonpulsed specimens at the same strain were prepared as 3 mm diameter disks using a twin jet polisher with a 30%  $\text{HNO}_3$  + 70% Methyl alcohol solution. Dark field images were obtained by TEM (JEOL/JEM-3000F) operating at 300 kV.

## **2.3 Effect of electric current on mechanical behavior and microstructure**

### 2.3.1 Electroplasticity in as-received specimen

Figure 2. 2 describes engineering stress-strain curves for a pulsed tensile test compared to a nonpulsed tensile test on as-received specimen. The selected pulsed electric current ( $\rho_0 = 110 \text{ A/mm}^2$ ,  $t_d=0.5 \text{ sec}$ ,  $t_p=30 \text{ sec}$ ) led to extreme increase in elongation. Once the pulsed electric current was applied, the flow stress instantly decreased (a stress-drop). Immediately on eliminating the pulsed electric current, the flow stress increased rapidly and showed strain hardening until the next pulse of electric current. Note that all the flow stresses of the pulsed tensile test except the region between the initial pulse and the second pulse decreased compared to the nonpulsed tensile test. This may suggest that the annealing of the material occurred under the pulsed electric current. In the same way, the sharp stress-drop at the application of each individual pulse of electricity may be explained by the combined effect of an instantaneous annealing of the material due to the electric current, a thermal expansion and a softening due to Joule heating.

To take into account the possible effect of Joule heating, the corresponding temperature of the specimen from the pulsed tensile test is measured as shown in Figure 2. 2 below the engineering strain-stress curve. The temperature increased instantly due to Joule heating when the pulsed electric current was

applied, and reduced rapidly due to heat transfer when the current was removed. The maximum temperature before the necking obtained from the thermal image was less than 270 °C. It should be noted that all the measured temperatures before the necking point are considerably lower than the usual range of annealing temperature for non-heat-treatable Al alloys (335-405 °C), and the holding time at higher temperature is also remarkably short (The Aluminum association, 2007) so that Joule heating is not likely to be a source of possible annealing.

The inverse pole figure LD maps are presented in Figure 2. 3. Figure 2. 3 (a) shows the microstructure of as-received specimen prior to the initiation of the test and Figure 2. 3 (b) describes microstructure obtained from nonpulsed tension after fracture. Figures 2. 3 (c) and (d) are obtained right before the necking (engineering strain=16.4%) and after the failure, respectively, of the pulsed tensile test.

The EBSD orientation (LD) map of the specimen from the nonpulsed tensile test at the failure strain shows that  $\langle 111 \rangle // LD$  and  $\langle 001 \rangle // LD$  orientations increased, which are stable orientations of FCC metal under the uniaxial tension mode (Pandey *et al.*, 2013), while  $\langle 101 \rangle // LD$  orientation decreased compared with the initial microstructure in Figure 2. 3 (a). This trend for the deformation-controlled microstructural change is still strongly observed in the specimen from the pulsed tensile test right before the necking as shown

in Figure 2. 3 (c). Even in the center of the cross sectional area of the specimen when necking starts at engineering strain of 16.4%, the microstructure shows the same trend with that from the side of the cross sectional area of the specimen, which is a deformation-controlled microstructural change with no recrystallization as shown in Figure 2. 4. The grain size of initial specimen on cross sectional area before tensile was  $30\ \mu\text{m}$  with an aspect ratio of  $0.288 \pm 0.125$  (Figure 2. 4 (a)). The grain size of the specimen unloaded at engineering strain of 16.4% on cross sectional area at center and side position were  $31\ \mu\text{m}$  with a aspect ratio of  $0.252 \pm 0.132$  and  $35\ \mu\text{m}$  with a aspect ratio of  $0.245 \pm 0.127$ , respectively (Figures 2. 4 (b) and (c)). However, the specimen from the pulsed tensile test after the failure, the recrystallization and grain growth were observed as shown in Figure 2. 3 (d). This suggests that the true electric energy density based on the actual cross sectional area of the deformed specimen reached sufficiently high to induce a significant thermal effect after the necking, causing recrystallization and grain growth.

From the stress and strain curves, the temperature measurement, and the microstructural observation by EBSD for the as-received specimen under a pulsed electric current, it was found that the elongation is drastically increased before the necking without the significant microstructural change such as recrystallization and grain growth due to Joule heating.

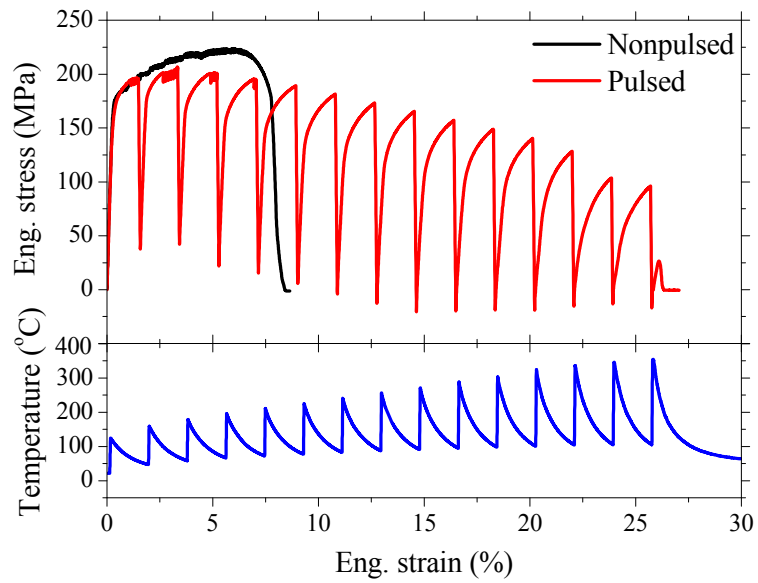


Figure 2. 2 Engineering stress-strain curves of nonpulsed (in black)/pulsed (in red) tensile test and measured temperature as a function of engineering strain (in blue) on the as-received specimen.

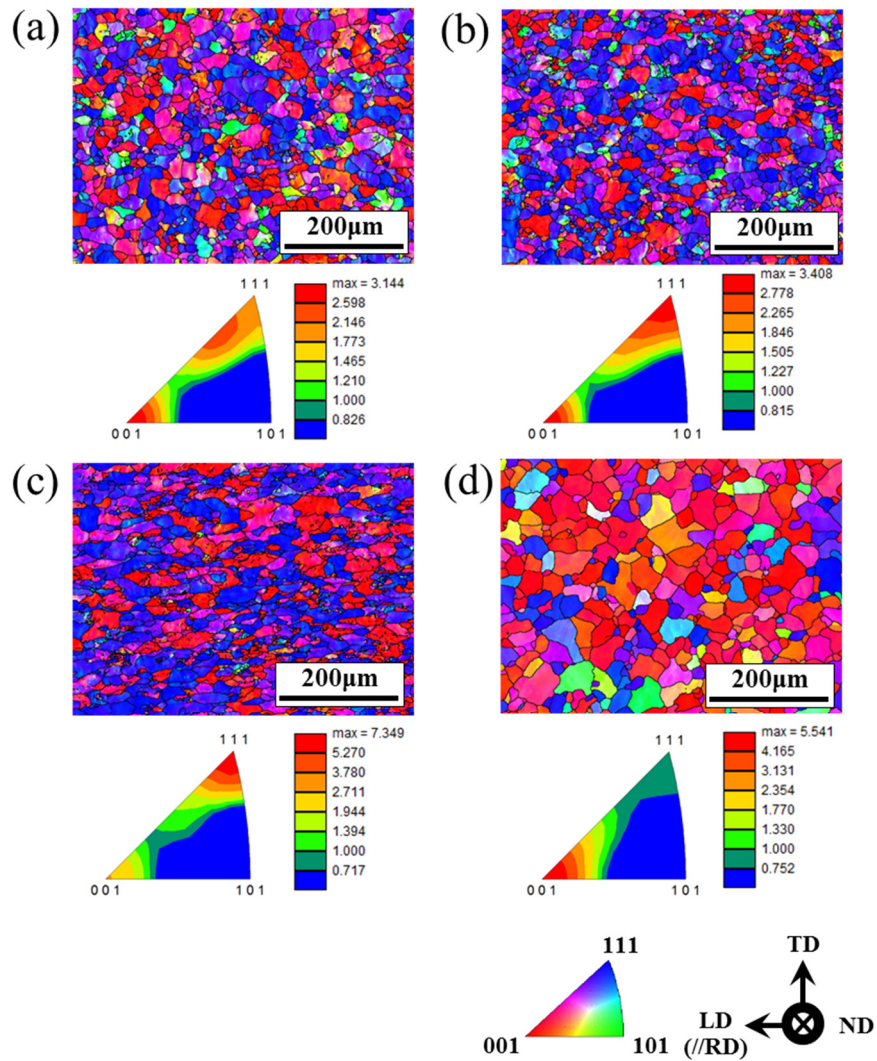


Figure 2. 3 Inverse pole figure LD(//RD) maps of as-received specimen (a) before tension, (b) after fracture from nonpulsed tension, (c) unloaded right before necking (at engineering strain of 16.4%) from pulsed tension and (d) after fracture from pulsed tension.

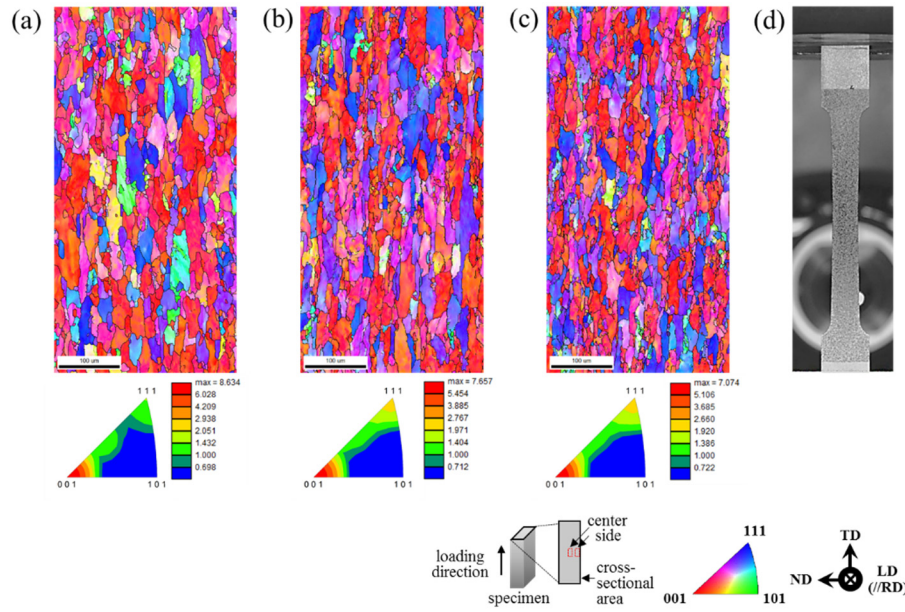


Figure 2. 4 Inverse pole figure LD maps of cross sectional area (a) before tension, (b) at center of the specimen at engineering strain of 16.4%, (c) at side of the specimen at engineering strain of 16.4% and (d) snap shot of specimen during pulsed tensile test from DIC measurement at engineering strain of 16.4%, when necking starts.

### 2.3.2 Electroplasticity in cold-rolled specimen

In order to confirm the hypothesis of the instantaneous annealing by a pulsed electric current, a uniaxial tensile test for 30% cold-rolled specimen was conducted under the same pulsing pattern. As shown in Figure 2. 5, the cold-rolled specimen shows the heavily work-hardened behavior with higher flow stress and shorter elongation compared with the as-received specimen from the nonpulsed tensile test due to the accumulation of dislocation by cold rolling. When a pulsed electric current was applied to the cold-rolled specimen during tensile deformation, however, it was observed that the elongation at fracture increased twice with softening of flow stress compared to the results of nonpulsed tensile test on 30% cold-rolled specimen. Finally, the total elongation of the pulsed tensile test on the cold-rolled specimen became almost the same as that of the nonpulsed tensile test on the as-received specimen. Like the as-received specimen, the temperature of the cold-rolled specimen from the pulsed tensile test was not over 300 °C until failure without the significant temperature rise.

After cold rolling, the microstructure is strongly elongated along the rolling direction as shown in Figure 2. 6 (a). Likewise the microstructure after fracture from nonpulsed tension, the dramatic microstructural change to the failure is not observed after fracture from pulsed tension on the cold-rolled specimen.

Therefore, it was found that the elongation of pulsed tension is still increased almost twice with clearly observed softening of flow stress compared to that of nonpulsed tension without the significant microstructural change such as recrystallization and grain growth due to Joule heating for the cold rolled specimen.

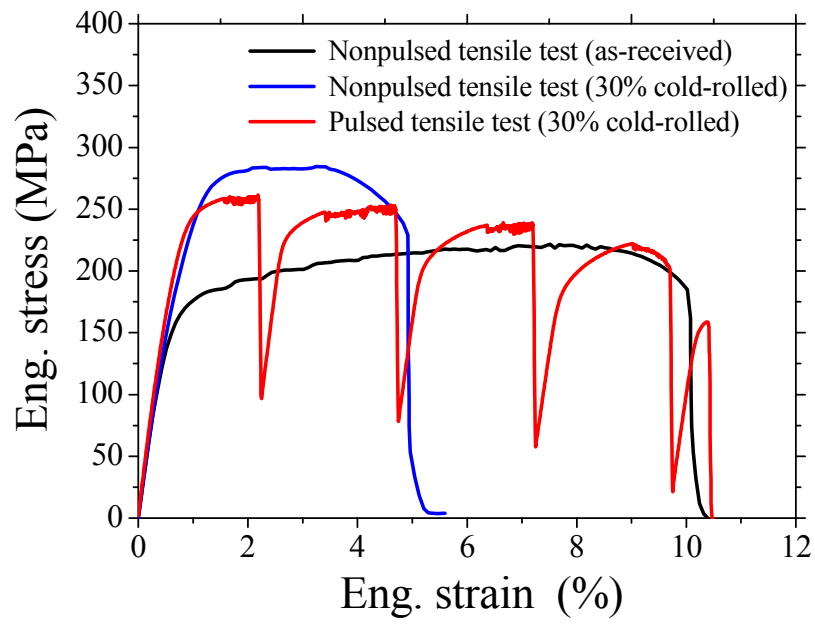


Figure 2. 5 Engineering stress-strain curves of nonpulsed (in black)/pulsed (in red) tensile test on 30% cold-rolled specimen.

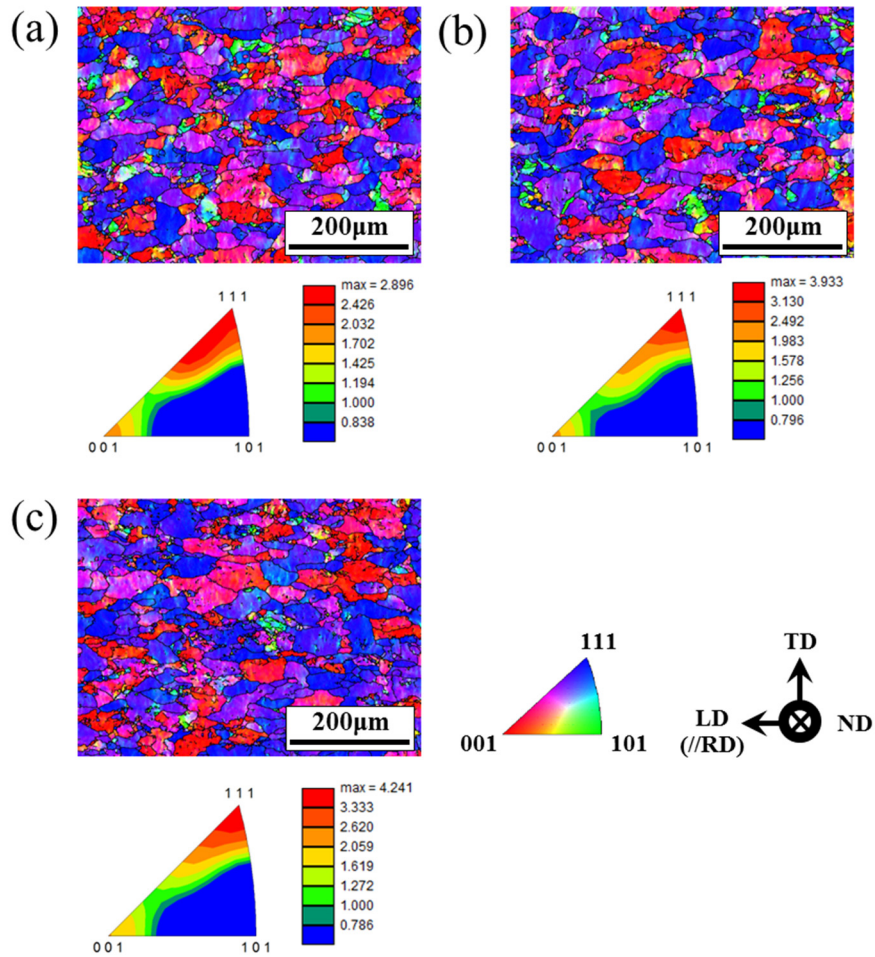


Figure 2. 6 Inverse pole figure LD(//RD) maps of 30% cold rolled specimen (a) before tension, (b) after fracture from nonpulsed tension and (c) after fracture from pulsed tension.

## **2.4 Electric current-induced annealing**

To clarify the origin of the annealing induced by a pulsed electric current, the dislocation density of the specimens was measured by Vickers hardness, XRD and TEM observations. Four kinds of specimens were prepared to compare the dislocation density. Deformed specimens were unloaded at engineering strain of 5% from nonpulsed and pulsed tension to compare the effect of electric current with as-received specimen before tension. To distinguish the Joule heating effect from applied electric current, two kinds of heat treatment were conducted using unloaded specimen at engineering strain of 5% from nonpulsed tension. From the measurement by K-type thermocouple, temperature history can be obtained at local position where the thermocouple is attached. By using IR camera, the average temperature of the gauge section can be considered. By preparing two kinds of heat treated specimens based on temperature history of thermocouple and IR camera as shown in Figure 2. 7 (in red curve), Joule heating effect can be considered by both local and average temperature of the specimen. Heat treatment was conducted using a dilatometer which controls the temperature of the specimen by an induction heater in a vacuum (in green curve).

Before comparing the dislocation density of each specimen mentioned above, the microstructure of the cross sectional area of deformed specimen unloaded at engineering strain of 5% from nonpulsed and pulsed tension was

observed to check the homogeneity in microstructure between center and side region of the cross sectional area (Figures 2. 8 and 9). The microstructure from pulsed tension shows deformation-controlled microstructural change with no recrystallization in both center and side region of the cross sectional area with a grain size of 35  $\mu\text{m}$  (aspect ratio:  $0.246 \pm 0.132$ ) and 32  $\mu\text{m}$  (aspect ratio:  $0.256 \pm 0.137$ ), respectively, which is the same microstructure shown in that from nonpulsed tension in both center and side region of the cross sectional area with a grain size of 36  $\mu\text{m}$  (aspect ratio:  $0.237 \pm 0.131$ ) and 30  $\mu\text{m}$  (aspect ratio:  $0.269 \pm 0.129$ ), respectively. Therefore, homogeneity in microstructure between center and side region of the cross sectional area was confirmed in both nonpulsed and pulsed tension at the engineering strain of 5%.

The result of Vickers hardness is presented in Figure 2. 10. Due to the plastic deformation, the value of Vickers hardness of nonpulsed specimen is higher than that of as-received specimen. The value of Vickers hardness of heat treated specimen is decreased due to the thermal recovery compared to that of nonpulsed specimen. However, it is still higher value than that of pulsed specimen even though the heat treatment was conducted identically based on temperature history of pulse specimen. It can be expected that electric current can induce additional recovery to deformed specimen.

To check dislocation density, XRD analysis was also performed. It is known that the X-ray diffraction peaks broaden when lattice defects such as

dislocation are present in large amounts in the crystal (Ungar, 2004). FWHM refers to microstructural broadening due to lattice defects under the same instrumental condition and finite crystallite size. In the present study, since the instrumental effect could be assumed to be the same at every measurement due to the identical operational condition, and the finite crystallite size was also almost similar under the nonpulsed/pulsed tensile test at the same strain, the FWHM is closely related to the dislocation density of the specimen. Figure 2. 11 shows the FWHM for the specimen from the nonpulsed/pulsed tensile test at the engineering strain of 5% as a function of  $2\theta$ , where  $\theta$  is the Bragg angle. As shown in Figure 2. 11, in the case of the specimen from the pulsed tensile test, the degree of line broadening, i.e. the value of FWHM, is far less than that from the nonpulsed tensile test. It is noted that the value of FWHM obtained from the specimen subjected to a pulsed electric current at the engineering strain of 5% is even less than that from the as-received specimen before deformation.

Figure 2. 12 shows dark field images of the specimen unloaded at engineering strain of 5% from nonpulsed/pulsed tension, respectively. More than fifty images of each specimen were observed for the validity on the distribution of dislocation. Dislocation density in the specimen from the pulsed tensile test is somewhat less than that from the nonpulsed tensile test. This clearly suggests that the specimen was annealed due to the annihilation of dislocation when a pulsed electric current was applied during deformation.

In order to clearly show the thermal annealing is not major attribution to the recovery process, a more severe thermal history, 10°C higher than the temperature measured at local position was applied to the specimen as shown in Figure 2. 7 (b), which had undergone the engineering strain of 5%. Interestingly, the FWHM of both two kinds of specimen, which represent the temperature history of local position and total gauge section, are still much higher than that of the specimen obtained from the pulsed tensile test at the same strain. This means that the temperature rise due to Joule heating at this experimental condition is not sufficient to cause thermal recovery in the specimen. From the results, it could be confirmed that the dislocation was annihilated not because of Joule heating but of a pulsed electric current applied during plastic deformation.

Finally, it can be said that ‘electric current-induced annealing (EIA)’ takes place when a pulsed electric current is applied to the specimen during plastic deformation without elevating the critical annealing temperature. This can be related to the electric current may enhance the atomic diffusion (Bertolino *et al.*, 2001; Mizubayashi *et al.*, 1989; Samuel *et al.*, 2010). In addition, the increase of serration in the stress-strain curves from the pulsed tensile test shown in Figures 2. 2 and 2. 5 would be studied in the future in terms of the diffusion enhancement of the solute atom due to electric current.

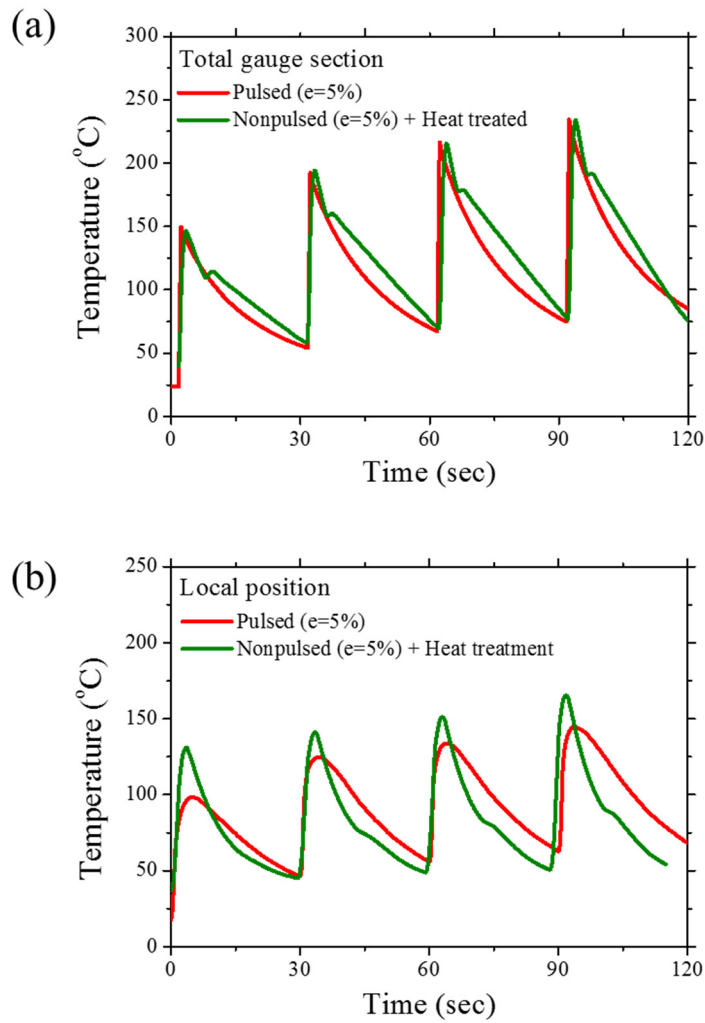


Figure 2. 7 (a) Average temperature history for total gauge section by IR camera (in red) and (b) local temperature history by thermocouple (in red) and corresponding heat treatment (in green) using induction heating system.

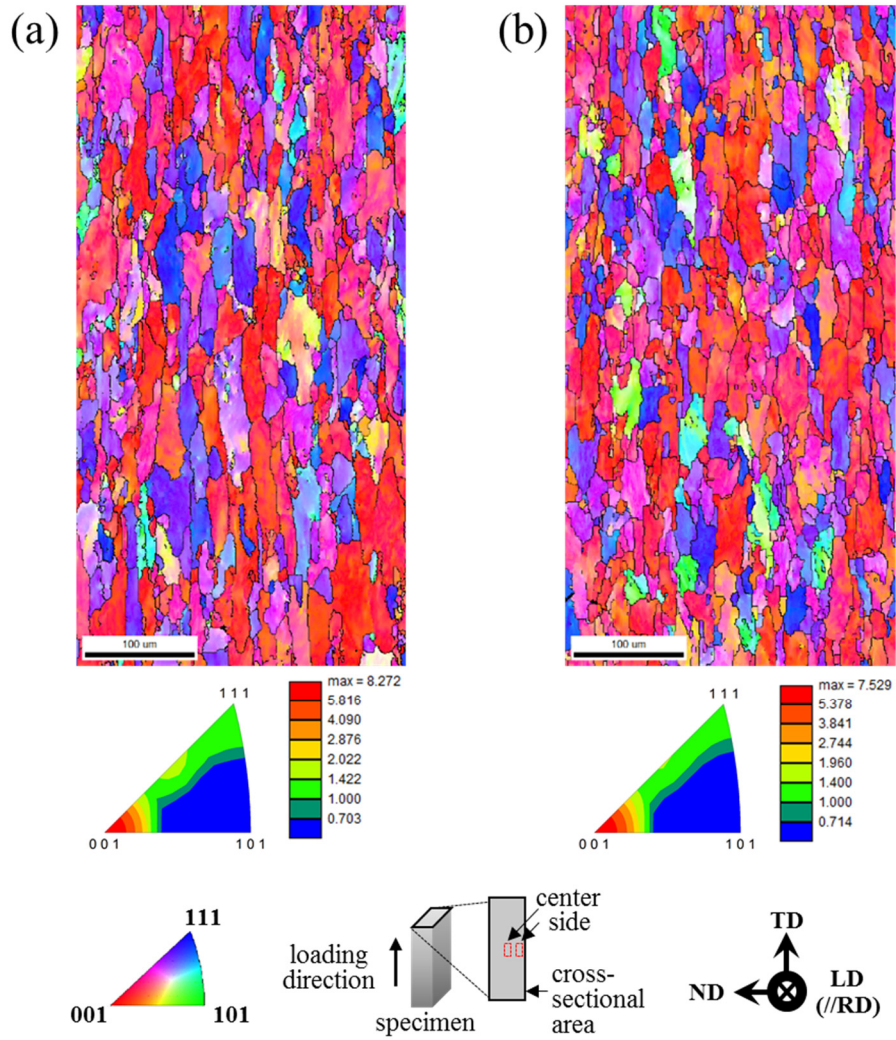


Figure 2. 8 Inverse pole figure LD maps of cross sectional area at (a) center and (b) side of the specimen at engineering strain of 5% from nonpulsed tension.

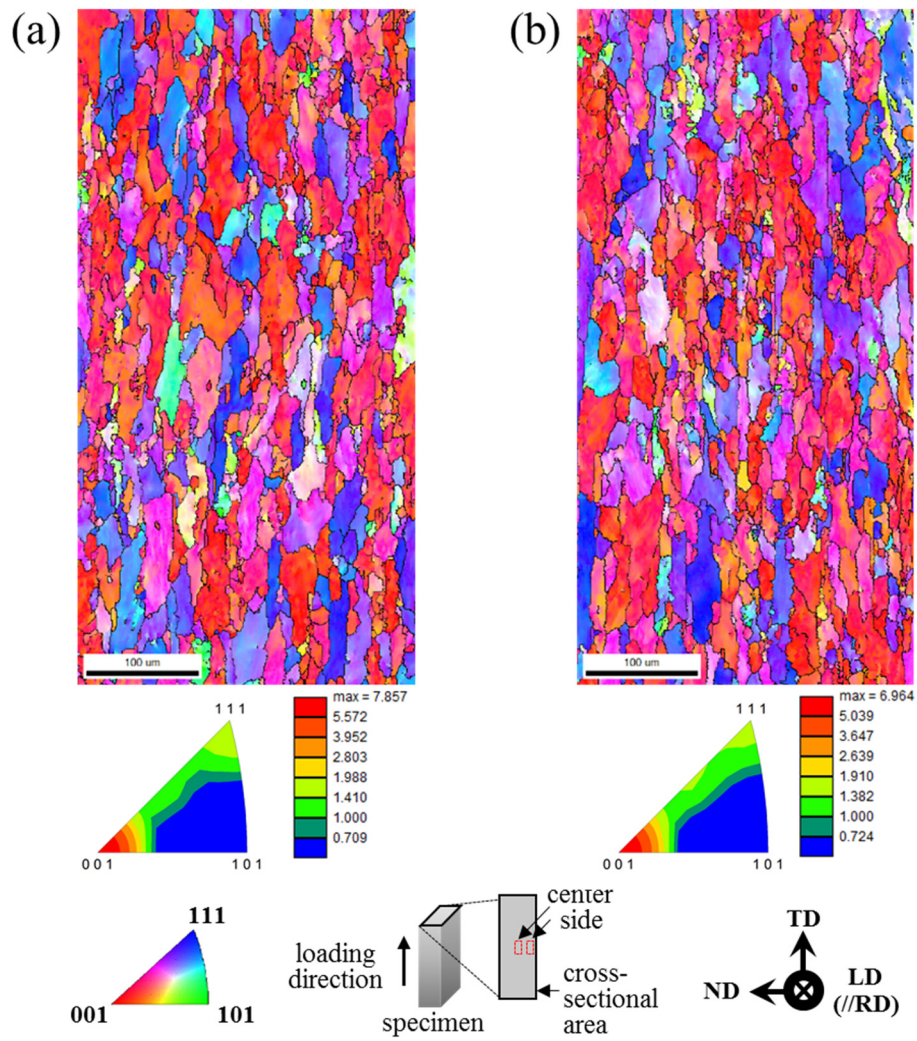


Figure 2. 9 Inverse pole figure LD maps of cross sectional area at (a) center and (b) side of the specimen at engineering strain of 5% from pulsed tension.

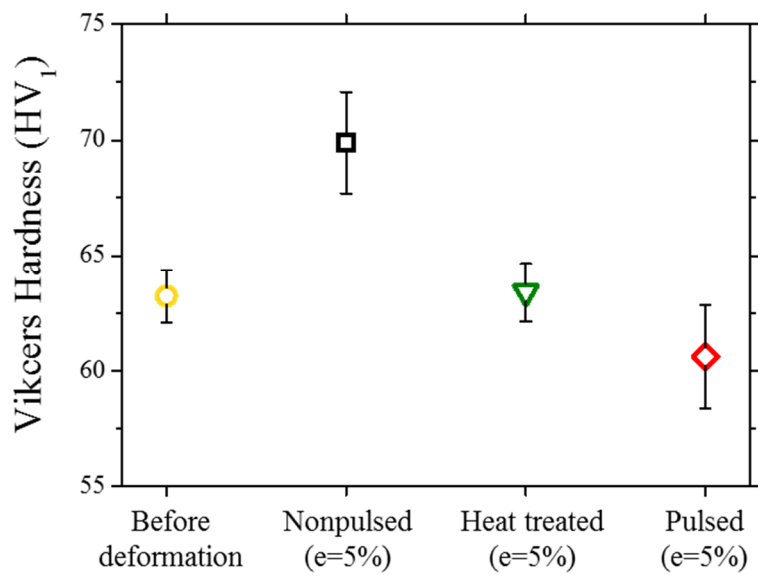


Figure 2. 10 Vickers hardness of as-received specimen, deformed specimens unloaded at engineering of 5% after nonpulsed/pulsed tension and heat treated specimen based on temperature history of total gauge section.

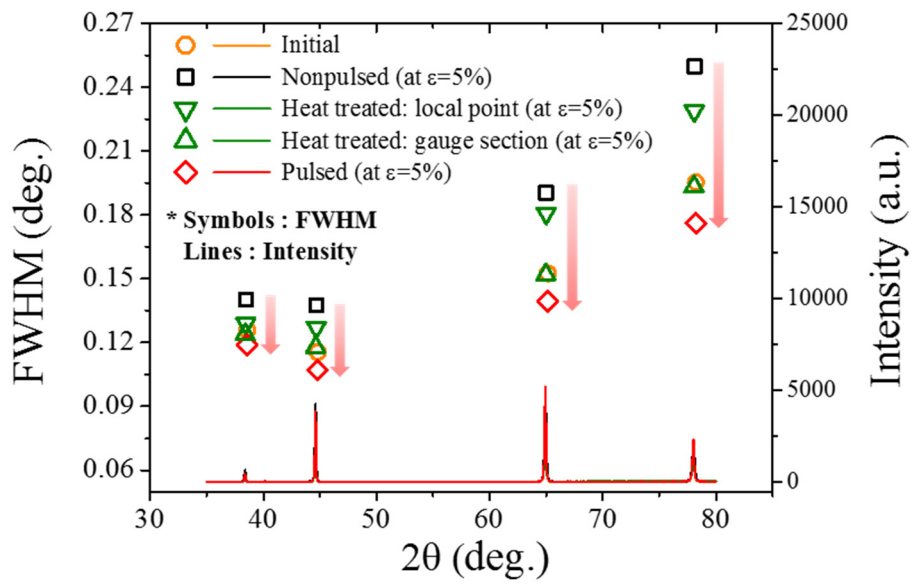


Figure 2. 11 Full width and half maximum profiles (symbols, left-axis) and X-ray diffraction patterns (lines, right-axis) in the range of 35-80°.

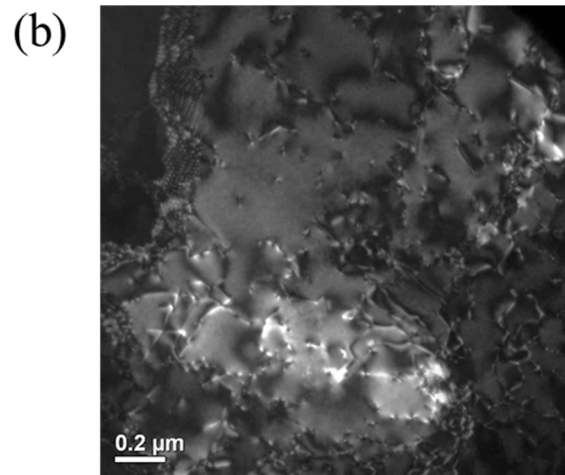
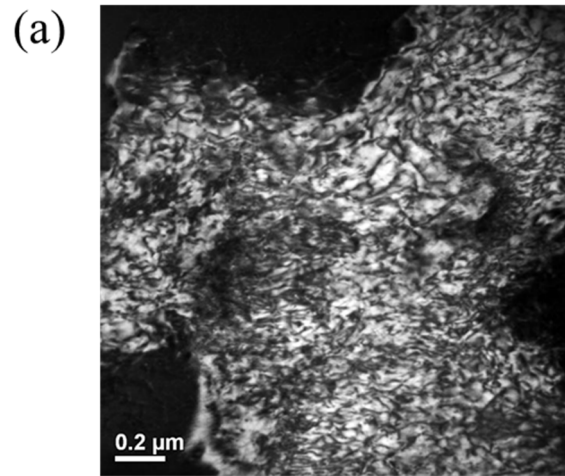


Figure 2. 12 Dark field images of specimens from (a) nonpulsed and (b) pulsed tensile test unloaded at engineering strain of 5%.

## 2.5 Summary

Mechanical behavior of Al-Mg alloy under a pulsed electric current was investigated by uniaxial tension combined with the subsequent microstructural observation using EBSD, XRD and TEM.

The elongation of both as-received and cold-rolled specimens increases drastically with softening of flow stress from the pulsed tensile test. Recrystallization and grain growth were observed after fracture from the pulsed tensile test and it could be expected that thermal effect would be dominant after severe necking. However, increase of formability before severe necking was still observed strongly and it could not be explained by usual thermal effect. It was confirmed that the recovery occurs at a given electric pulsing condition comparing with nonpulsed tensile test.

From the results of Vickers hardness, XRD, and TEM analysis, it could be confirmed that the dislocation was annihilated not because of Joule heating but of a pulsed electric current applied during plastic deformation. Finally, it can be said that ‘electric current-induced annealing (EIA)’ takes place when a pulsed electric current is applied to the specimen during plastic deformation without elevating the critical annealing temperature.

This study proves important conclusion that the electric current could induce additional annealing as a distinct role from Joule heating. Further studies are required to clarify the correlation of electric current with dislocation motion

in view of diffusion enhancement of atoms.

## 2.6 References

- Andrawes, J.S., Kronenberger, T.J., Perkins, T.A., Roth, J.T., Warley, R.L., Mater. Manuf. Process 22 (2007) 91.
- Bertolino, N., Garay, J., Anselmi-Tamburini, U., Munir, Z., Scripta Mater. 44 (2001) 737.
- Conrad, H., Cao, W.-D., Lu, X.-P., Sprecher, A., Scr. Metall. 23 (1989) 697.
- Conrad, H., Mater. Sci. Eng. A 287 (2000) 276.
- Conrad, H., Mater. Sci. Eng. A 322 (2002) 100.
- Fan, R., Magargee, J., Hu, P., Cao, J., Mater. Sci. Eng. A 574 (2013) 218.
- Goldman, P.D., Motowidlo, L.R., Galligan, J.M., Scripta Metall. 15 (1981) 353.
- Jones, J.J., Mears, L., J. Manuf. Sci. Eng. 135 (2013) 021011.
- Kim, J.H., Jo, J.S., Sim, J.S., Im, H.J., Korea. J. Met. Mater. 50 (2012) 669.
- Li, C., Jiang, S., Zhang, K., Int. J. Adv. Manuf. Technol 63 (2012) 931.
- Lu, X.-P., Cao, W.-D., Sprecher, A., Conrad, H., J. Mater. Sci. 27 (1992) 2243.
- Miaoquan, L., Yanyum, C., Dengjun, C., J. Mater. Process. Technol. 73 (1998) 264.
- Miller, W.S., Zhuang, L., Bottema, J., Wittebrood, A.J., Smet, P., Haszler, A., Vieregge, A., Mater. Sci. Eng. A 280 (2000) 37.
- Mizubayashi, H., Okuda, S., Phys. Rev. B 40 (1989) 8057.
- Pandey, A., Khan, A.S., Kim, E.-Y., Choi, S.-H., Gnaupel-Herold, T., Int. J. Plast. 41 (2013) 165.

Pogatscher, S., Antrekowitsch, H., Leitner, H., Sologubenko, A.S., Uggowitzer, P.J., *Scripta Mater.* 68 (2013) 158.

Roh, J.-H., Seo, J.-J., Hong, S.-T., Kim, M.-J., Han, H.N., Roth, J.T., *Int. J. Plast.* 58 (2014) 84.

Salandro, W. A., Jones, J.J., Mcneal, T.A., Roth, J.T., Hong, S.-T., Smith, M.T., *J. Manuf. Sci. Eng.* 132 (2010) 051016.

Salandro, W.A., Roth, J.T., *Electrically Assisted Manufacturing*, in: W. Zhang, *Intelligent energy field manufacturing*, CRC Press, Boca Raton, (2010) 505.

Samuel, E.I., Bhowmik, A., *J. Mater. Res.* 25 (2010) 1020.

The Aluminum Association, *Rolling Aluminum: From the mine through the mill*, in: *Purposes of annealing*, The Aluminum Association, Arlington, 2007, 3rd Edition.

Toros, S., Ozturk, F., Kacar, I., *J. Mater. Process. Tech.* 207 (2008) 1.

Troitskii, O.A., *Strength of Mater.* 16 (1984), 277.

Ungar, T., *Scripta Mater.* 51 (2004) 777.

Xu, A.S., Lai, Z.H., Chen, Y.X., *Scr. Metall.* 22 (1988) 187.

## **Chapter 3**

# **Electroplasticity in precipitation-hardened aluminum alloy (Al-Mg-Si alloy)**

### **3.1 Introduction**

In chapter 2, electroplasticity in non-heat treatable aluminum alloy was investigated based on mechanical behavior and microstructural analysis. Even though a number of researches have been conducted on the effect of electric current on deformation, the amount of experimental data to clearly understand the phenomenon of electroplasticity is not sufficient yet. For example, the electroplasticity of age hardening nonferrous metal alloys has not been well studied yet. The objective of present study is to investigate the effect of electric current on the mechanical behavior of Al-Mg-Si alloy, which is a representative age hardening alloy system, based on microstructural perspective. The microstructural observations of the specimens from a nonpulsed/pulsed tensile test were performed using optical microscopy (OM), X-ray diffraction (XRD), scanning electron microscopy (SEM) and transmission electron microscopy (TEM). The deformation behavior associated with electroplasticity was then discussed based on the microstructural changes of the specimens.

## **3.2 Experimental procedures**

### **3.2.1 Specimen preparation**

A commercial Al-Mg-Si alloy (Al-0.87Mg-0.66Si-0.23Cu in wt.%) sheet with a thickness of 2 mm in artificially aged state (T6 temper, as-received) was used. Tensile specimens with a gauge width of 12.5 mm and a gauge length of 50 mm were prepared along the rolling direction of the sheet according to the ASTM E8 standard (ASTM, 2010). Three different heat treatment conditions, solid solution treated (or simply, solution treated), naturally aged, and artificially aged, were considered in the present study as shown in Fig. 1. For the solution treatment, artificially aged (as-received) tensile specimens were placed in a furnace at a temperature of 530 °C for 1 hour and quenched in cold water. To avoid aging effect of the solution treated specimens even in room temperature, tensile tests of the solution treated specimens were conducted within a few minutes after quenching. To prepare naturally aged (T4 temper) specimens, solution treated specimens were placed at room temperature for 4 days after quenching according to ASTM B918 (ASTM, 2001). Finally, the as-received specimens were directly used as artificially aged specimens without additional heat treatment.

<i>Al</i>	<i>Mg</i>	<i>Si</i>	<i>Fe</i>	<i>Cu</i>	<i>Cr</i>
95.7	0.87	0.66	0.43	0.23	0.17

Table 3.1 Chemical composition of Al-Mg-Si alloy (in wt.%)

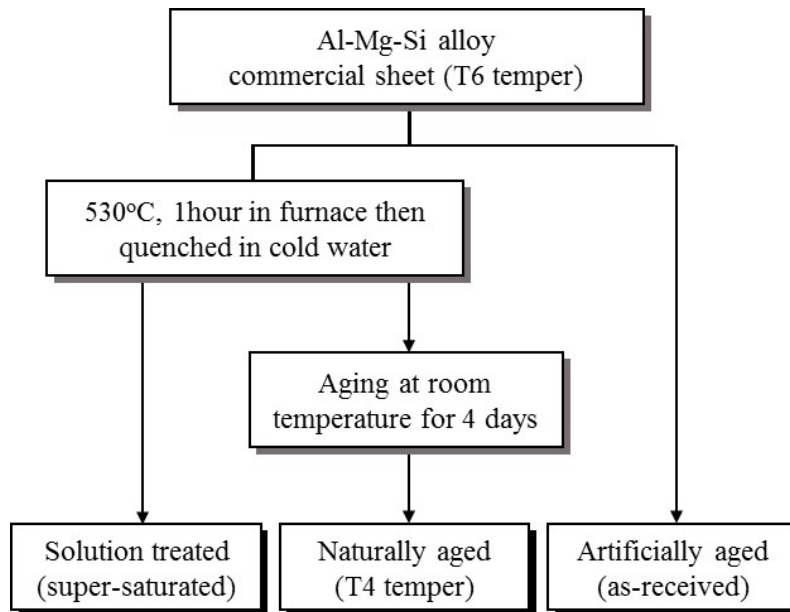


Figure 3.1 Three types of specimens based on different heat treatments.

### 3.2.2 Experimental set-up

The experimental set-up to measure the strain, stress and temperature of the specimen was carefully described in 2.2.2. The instrumental set-up was the same with previous work. Only the pulsing pattern in Al-Mg-Si alloy was different compared to that in Al-Mg alloy.

Electric current was periodically applied to the specimen with a duration ( $t_d$ ) of 0.5 sec and a period ( $t_p$ ) of 30 sec until fracture as schematically shown in Figure 3. 2. For all the three heat treatment conditions selected in the present study, the first pulse of electric current was applied after yielding. The amplitude of electric current was kept constant through the whole tensile test with a pulsed electric current to induce a constant nominal electric current density of ( $\rho_0$ ) 90 A/mm<sup>2</sup> based on the initial cross sectional area of the specimen. Note that as the specimen is continuously deformed by tension, the cross sectional area of the gage continuously decreases. Therefore, with the constant amplitude of electric current, the true electric current density ( $\rho_i$ ) based on the actual cross sectional area at each pulse of electric current continuously increases and is always higher than the constant nominal electric current density in tension.

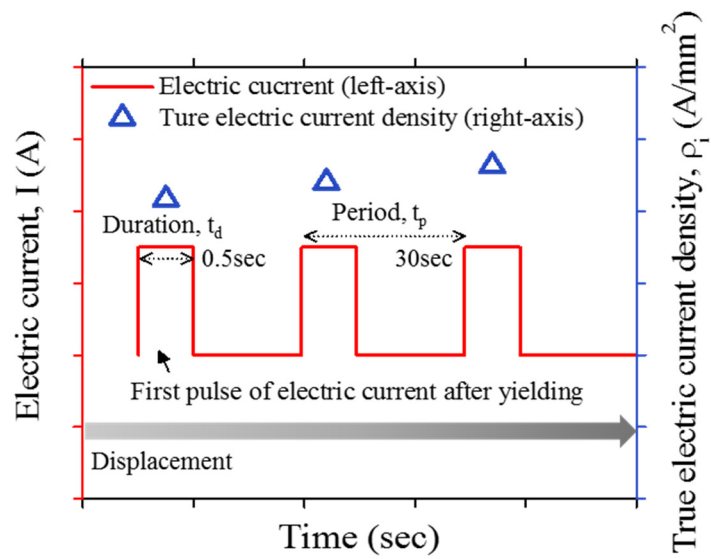


Figure 3. 2 Pulsing pattern during uniaxial tensile test. Selective pulsing pattern ( $\rho_0 = 90 \text{ A/mm}^2$ ,  $t_d=0.5 \text{ sec}$ ,  $t_p=30 \text{ sec}$ ) was applied to the specimen during plastic deformation after yielding. Constant value of electric current was applied during deformation.

### 3.2.3 Microstructural observation

Microstructures of the tested specimens with the three different heat treatment conditions were observed by FE-SEM equipped with EBSD system (FE-SEM: SU70, Hitachi, Japan and EBSD: Hikari EBSD detector with TSL OIM 6.1 software, EDAX/TSL, USA). Samples for microstructural analysis were prepared by a standard metallographic grinding technique. After grinding and polishing, they were electropolished with an electrolyte consisting of 10% perchloric acid and 90% ethanol at a temperature of about -20°C and a voltage of 20 V. For EBSD observation, the accelerating voltage of 15 kV and the working distance of 15 mm were used. The mapping grid was a regular square in 1  $\mu\text{m}$ , and critical misorientation angle was set to 10° for grain identification.

Thin-foil specimens for TEM were prepared by mechanical grinding followed by electropolishing in a Tenupol-3 double jet thinner (Struers, Denmark) with an electrolyte consisting of 30% nitric acid and 70% methanol at a temperature of -20°C and a voltage of 6 V. Also, focused ion beam (FIB, Nova Nanolab 200) micromachining (FEI, USA) was used to observe the specific region. TEM investigation was carried out in a JEM-2100F (JEOL, USA) operated at 200 kV. The chemical composition of precipitates was investigated by EDX in TEM and FE-SEM.

The topography of the fracture surface was also examined using a SU 70 FE-SEM operated at 15 kV. In addition, Vickers hardness measurement was conducted with a 1 kg load and the hardness was measured at least 10 times for

each specimen. Finally, XRD line profiles were measured with a D8-advanced diffractometer (BRUKER MILLER Co., Germany) using Cu K $\alpha$  radiation ( $\lambda=0.15406$  nm) operating at 40 kV. The diffraction lines were recorded in the region of  $2\theta=30-140^\circ$  with a scan rate of  $3^\circ/\text{min}$ . The measured diffraction peaks are fitted with Pearson VII function in the present analysis.

### **3.3 Basic properties: Mechanical behavior and microstructure**

#### 3.3.1 Mechanical behavior

As expected, the engineering stress-strain curve without electric current (or simply, baseline) shows significantly different yield stress and elongation depending on the heat treatment conditions (solution treated, naturally aged, and artificially aged) as shown in Figure 3. 3 (a). The solution treated specimen shows the highest elongation (about 20%) with a minimal yield stress among three types of specimens tested in this study. One very interesting phenomenon is that the serration, so-called Portevin-Le Chaterlier (PLC) phenomenon, is clearly observed until fracture only in solution treated specimen. For the naturally aged specimen, the yield stress is higher than that of the solution treated specimen, while the elongation is slightly lower than that of the solution treated specimen. The artificially aged specimen shows the highest yield stress with the lowest elongation less than 10% among the specimens with the three different heat treatment conditions. The results of Vickers hardness indicate the same trends with those of yield strength for the three types of specimens as shown in Figure 3. 3 (b).

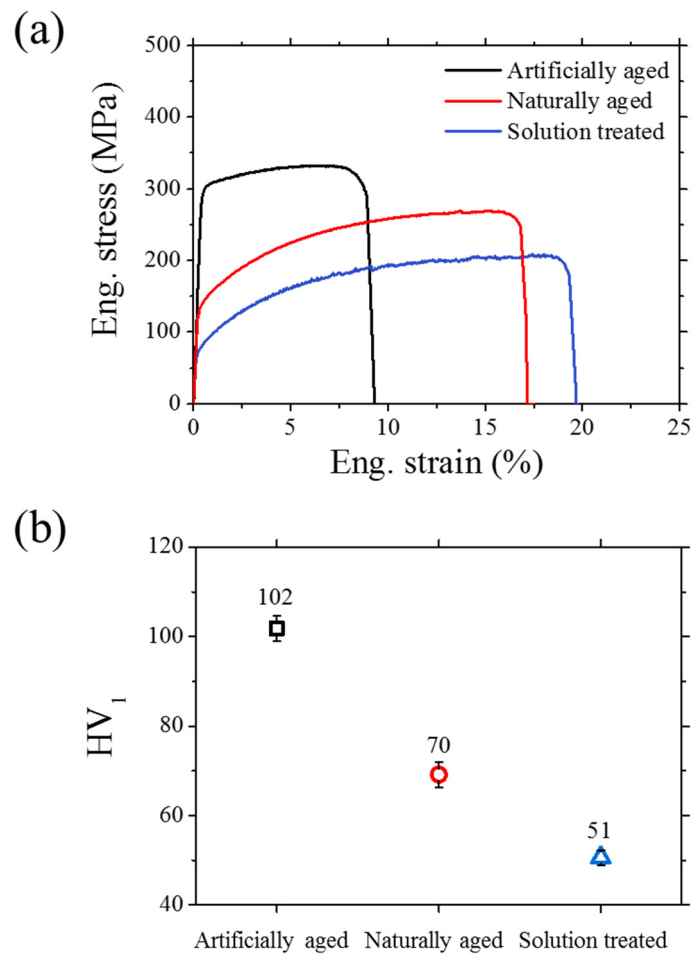


Figure 3. 3 (a) Engineering stress-strain curves and (b) Vickers hardness of Al-Mg-Si alloy for artificially aged, naturally aged and solution treated specimens.

### 3.3.2 Microstructure

The grain sizes of the naturally aged and artificially aged specimens are quite similar with each other (67 and 69  $\mu\text{m}$ , respectively), as shown in Figure 3. 4. Therefore, the grain size has the negligible effect on the dissimilar mechanical behaviors shown in Figure 3. 3. It is clear that the different mechanical behaviors shown in Figure 3. 3 are mainly due to the different precipitation states of the specimens caused by the three different heat treatment conditions.

It is well known that Al-Mg-Si alloys can be strengthened by precipitation hardening during aging (Edwards *et al.*, 1998). It was reported that there is no evidence for specific precipitation immediately after solution treatment followed by quenching (Gracio *et al.*, 2004). It is expected that the dissolved solute atoms by solution treatment exist as a supersaturated state rather than forming precipitates immediately after quenching. Through natural aging at room temperature (T4 temper) after solution treatment, it is known that the supersaturated Mg and Si solutes form atomic clusters or Guinier-Preston (GP) zones as an early stage of precipitates (Murayama *et al.*, 1998, Banhart *et al.*, 2010).

Upon artificial aging process (T6 temper), the early stage of precipitates begin to develop into needle/lath-like precipitates ( $\beta''$ ) and finally form stable precipitates ( $\beta$ ,  $\text{Mg}_2\text{Si}$ ) (Murayama *et al.*, 1999). In Figure 3. 5, high density of short needle shaped  $\beta''$  precipitates can be seen with the  $\langle 001 \rangle_{\text{Al}}$ -direction in

the artificially aged specimen. These precipitates exist inside the grain with the length of 30-100 nm, which affect the hardening property of the alloy. Also, the grain boundaries are decorated by intermetallic compounds as shown in Figure 3. 6 (a). The size distribution of this intermetallic phase is about 150-300 nm, which is coarser than those of  $\beta''$  precipitates. An EDX analysis confirms that its composition type is Al-Si-Cu, which is different from the composition of  $Mg_2Si$  as hardening phase in Al-Mg-Si alloy. It is important to note that the intermetallic phase containing Si and Cu are segregated at grain boundary and the intermetallic phase does not have a significant effect on hardening property of the alloy like  $\beta''$  precipitates. This intermetallic compound was not observed in the solid solution treated and the naturally aged specimens.

These microstructural features of Al-Mg-Si alloy suggest that the lowest yield stress of the solution treated specimen is due to the absence of hardening phase. Also, the clear PLC phenomenon was observed only in solution treated specimen caused by the interaction between supersaturated solute atom and dislocation. In naturally aged specimen, the increased yield stress compared to that of the solution treated specimen is caused by the formation of the early stage of precipitates, such as atomic cluster or GP zones during natural aging. In case of the artificially aged specimen, tens of nanometer sized  $\beta''$  precipitates shown in Figure 3. 5 are believed to act as obstacles to dislocation movement. As a result, the artificially aged specimen shows the highest yield stress among the specimens with three different heat treatment conditions.

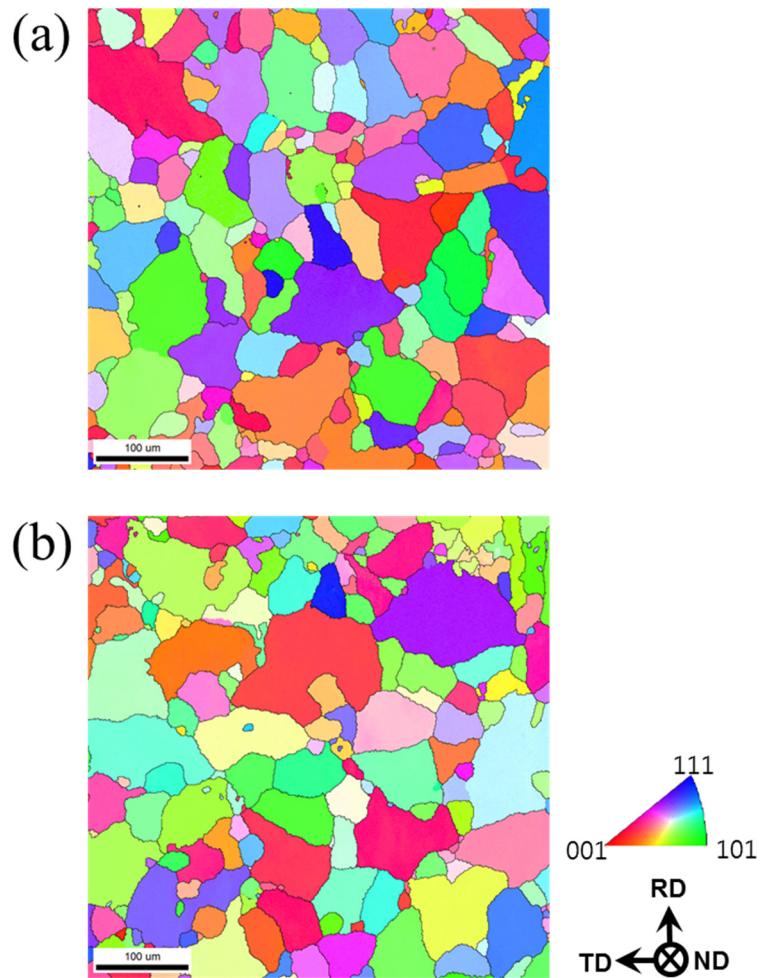


Figure 3. 4 Inverse pole figure (ND) maps of (a) naturally aged and (b) artificially aged specimens. High angle misorientation over  $10^\circ$  is marked as black lines for grain identification. The grain sizes of naturally aged and as-received specimens were 67 and 69  $\mu\text{m}$ , respectively.

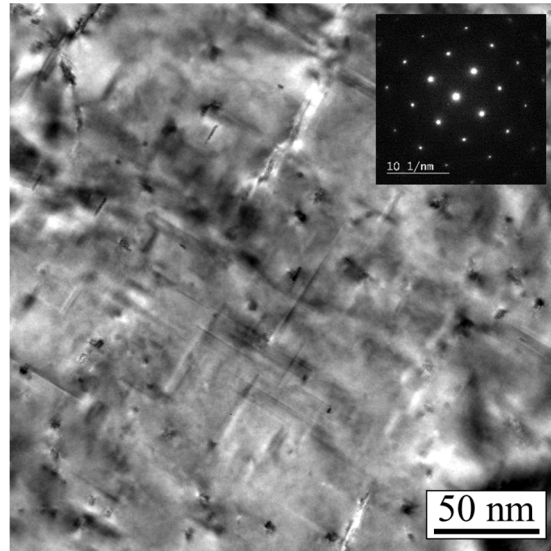


Figure 3. 5 TEM bright field image of needle-shaped  $\beta''$  phase in the grain interior including [001] selected area diffraction pattern in artificially aged specimen before uniaxial tension.

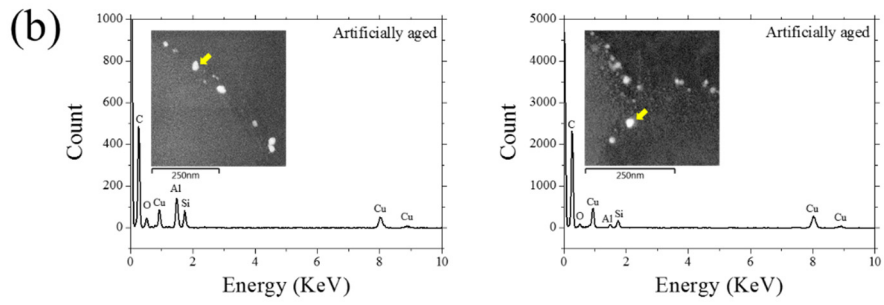
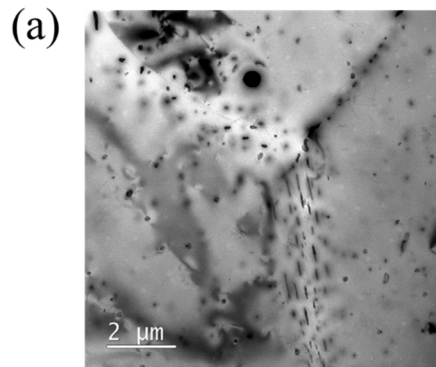


Figure 3. 6 (a) TEM bright field image of coarse intermetallic compound at the grain boundary and (b) EDX spectrums on the intermetallic compounds in artificially aged specimen before uniaxial tension.

### **3.4 Effect of electric current on uniaxial quasi-static tensile behavior**

Figure 3. 7 presents engineering stress-strain curves with a pulse electric current (in red) compared to the baseline (in black). When electric current was applied to the specimen with a duration of 0.5 sec during plastic deformation, the flow stress decreased nearly instantly for all tested specimens. After each pulse of electric current, the flow stress showed strain hardening until the next pulse of electric current (so called local stress-strain curve) (Roh *et al.*, 2014). The sharp stress-drop at the application of each individual pulse of electric current have been explained by the combined effect of an instantaneous annealing of the material due to the electric current, a thermal expansion and a softening due to Joule heating (Roth *et al.*, 2008; Salandro *et al.*, 2009; Roh *et al.*, 2014).

Since the electric current parameters, which are the duration, the period, and the electric current density were fixed through the whole tensile test, the measured temperature histories were almost same with each other for the specimens with different heat treatment conditions as expected as shown in blue in Figure 3. 7. The temperature increased instantly by Joule heating and rapidly decreased by air cooling until the next pulse of electric current. For all the specimens, the peak temperature shows a steady increase due to the continuously decreasing cross-sectional area during deformation.

As shown in Figure 3. 7, the electric current parameters selected in the present study led to different tensile behaviors depending on the heat treatment conditions. For the solution treated specimen, the elongation under a pulsed electric current increases in comparison with baseline in Figure 3. 7 (a). As an electric current applied to specimen repeatedly during deformation, the local stress-strain curve starts to deviate from the baseline. The peak stress of local stress-strain curve is higher than that of base line stress-strain curve and the deviation of peak stress between local and baseline stress-strain curve increases as plastic deformation proceeds. The PLC phenomenon, which is clearly observed in the baseline, becomes weaker and finally disappears after the engineering strain of 8% under the given pulsed electric current for the solution treated specimen. The magnified views of these serrations (regions 1 and 2) are shown in the right side of Figure 3. 8.

For the natural aged specimen, the elongation under a pulsed electric current significantly increased about 1.4 times in comparison with the baseline as shown in Figure 3. 7 (b). The local stress-strain curve also begins to deviate from the baseline and the difference of peak stress between local and baseline stress-strain curve increases. However, the peak stress of local stress-strain curve is lower than that of baseline, which is contrary to the result observed in solution treated specimen as shown in Figure 3. 7 (a). Also, serration in flow stress was not observed for the naturally aged specimens in both nonpulsed and pulsed tensile test.

It is interesting to note that the solution treated and naturally aged specimens show similar deformation behavior after the engineering strain of 15%, by applying electric current during plastic deformation, even though the baseline curve of solution treated and naturally aged specimen show different mechanical behavior in flow stress and elongation. The difference of flow stress after engineering strain of 15% between solution treated and naturally aged specimens is less than 5%, when electric current was applied. Also, the fracture elongation from pulsed tensile test is also similar as 23% for solution treated specimen and 24% for naturally aged specimen. These results indicate that the tensile behavior of the solution treated specimen becomes gradually similar to that of the naturally aged specimen under the given pulsing pattern.

The disappearance of PLC phenomenon, which is not observed in naturally aged specimen as mentioned before, in solution treated specimen with a pulsed electric current is another feature of similar mechanical behavior between solution treated and naturally aged specimens. If supersaturated solute atoms are not existed sufficiently to interrupt the movement of dislocation due to the formation of precipitates, PLC phenomenon may be getting weaker. Therefore, the increase of flow stress together with the disappearance of PLC phenomenon with a pulsed electric current compared the baseline in solution treated specimen may be caused by the formation of early stage precipitates from supersaturated solute atoms by applying electric current. In other words, the solution treated specimen undergoes an aging under a given electric current

during deformation by formation of the early stage precipitates from supersaturated solute atoms.

In order to investigate the effect of electric current on aging, Vickers hardness test was also conducted as shown in Figure 3. 9 (b). The Vickers hardness of the solution treated specimen before tension was  $50.5 \pm 1.7$  HV. The hardness increased as  $82.8 \pm 2.3$  HV due to the accumulation of plastic deformation after engineering strain of 17% from nonpulsed tensile test. The hardness of the specimen strained to 17% from pulsed tension is  $97.5 \pm 3.2$  HV, which is clearly higher than from nonpulsed tension. It means that aging takes place during deformation by applying electric current.

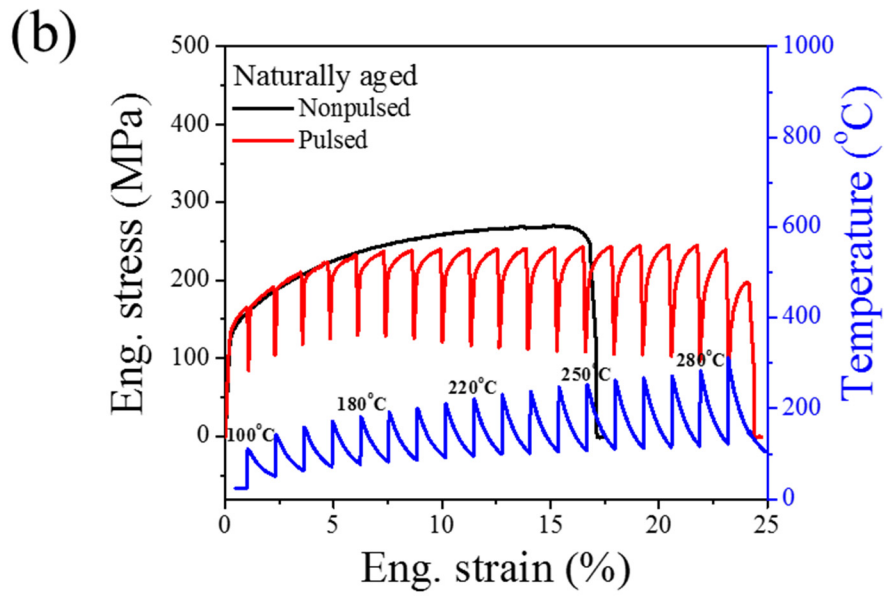
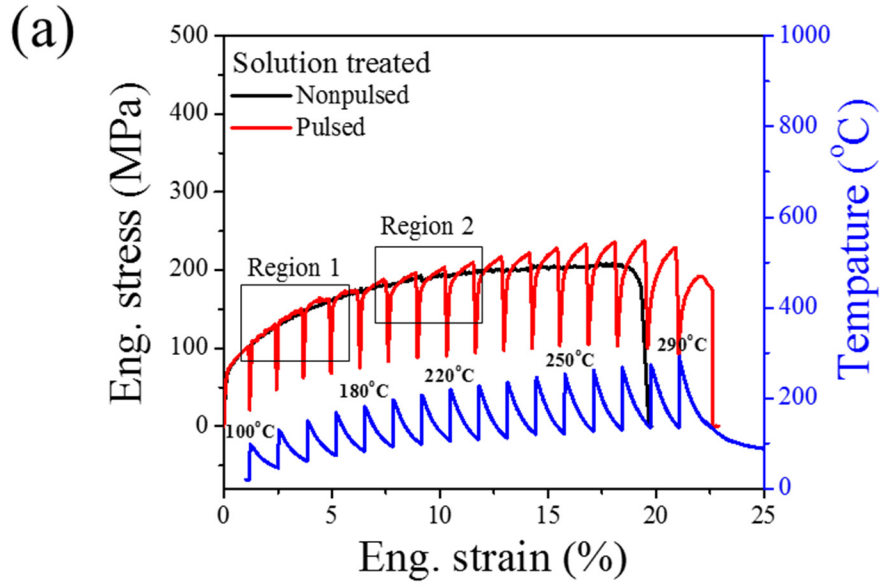
To classify the distinct effect of electric current on aging apart from Joule heating, the Vickers hardness measurement was performed for solution treated specimen which had undergone an engineering strain of 17% from nonpulsed tension followed by various heat treatment conditions. Heat treatments were conducted using both furnace and dilatometer which enables the temperature of specimen to be controlled rapidly by an induction heater in a vacuum. The total time over the 100 °C until the engineering strain of 17% is about 250 sec in pulsed tensile test as shown in Figure 3. 9 (a) (red line). Therefore, the holding time for furnace heat treatment of the specimen strained to 17% was set as 250 sec. The temperatures for heat treatment were chosen as 100, 150 and 200°C as shown in Figure 3. 9 (a) (green lines). In case of heat treatment using

dilatometer, the same temperature history in pulsed tension was applied as shown in Figure 3. 9 (a) (blue line).

There is no increase in hardness through heat treatment at 100°C for 250 sec compared to the result before heat treatment. This means that this heat treatment condition is not enough to obtain an aging effect. However, it can be seen that the hardness increases by elevating the temperature to 150 and 200 °C. Especially, the hardness of the specimen through the heat treatment at 200 °C ( $97.4 \pm 2.7$  HV) is almost same with that of the specimen strained to 17% from pulsed tension ( $97.5 \pm 3.2$  HV). Note that this heat treatment condition is much stronger than the temperature history of specimen during pulsed tension. The hardness of induction heat treated specimen is  $88.5 \pm 4.2$  HV, which is much lower than that of the specimen strained to 17% under a pulsed electric current, even though the heat treatment was conducted almost identically with the temperature history during pulsed tension. Based on these results of various heat treatments, it can be said that the aging might be accelerated by applying electric current with a distinct effect of Joule heating.

In artificially aged specimen, as shown in Figure 3. 7 (c), the flow stress under the electric current decreases compared to the baseline, which is the similar trend as observed in naturally aged specimen. However, in contrast to other two heat treatments (solution treated and naturally aged specimens), the elongation under the electric current decreases compared to the baseline. The

reason for earlier fracture of artificially aged specimen by applying electric current will be discussed in detail in section 3.6.



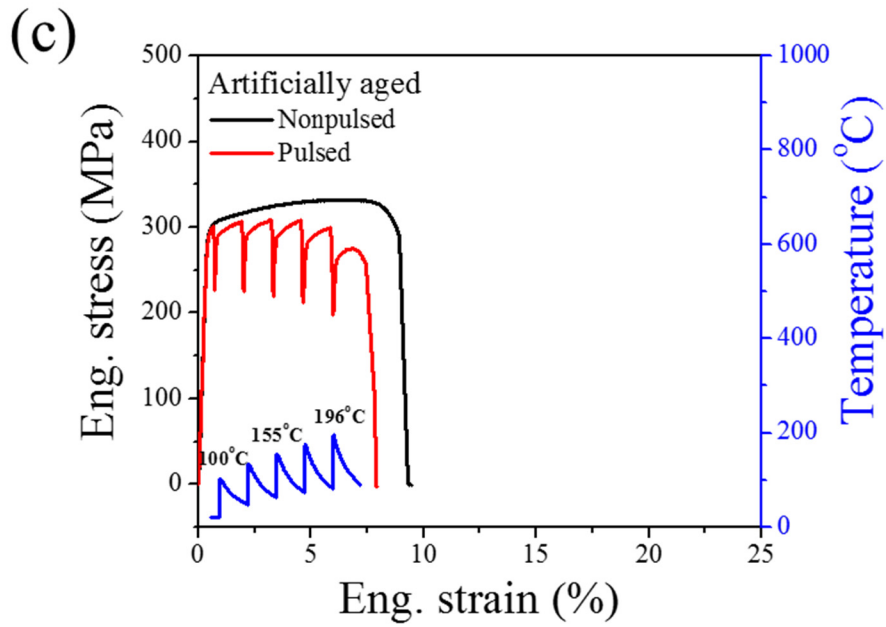


Figure 3. 7 Engineering stress-strain curves without (black curve) and with (red curve) applying electric current of (a) solution treated, (b) naturally aged and (c) artificially aged Al-Mg-Si alloy. The temperature due to joule heating was shown below the stress-strain curve as a function of engineering strain (blue curve, right-axis).

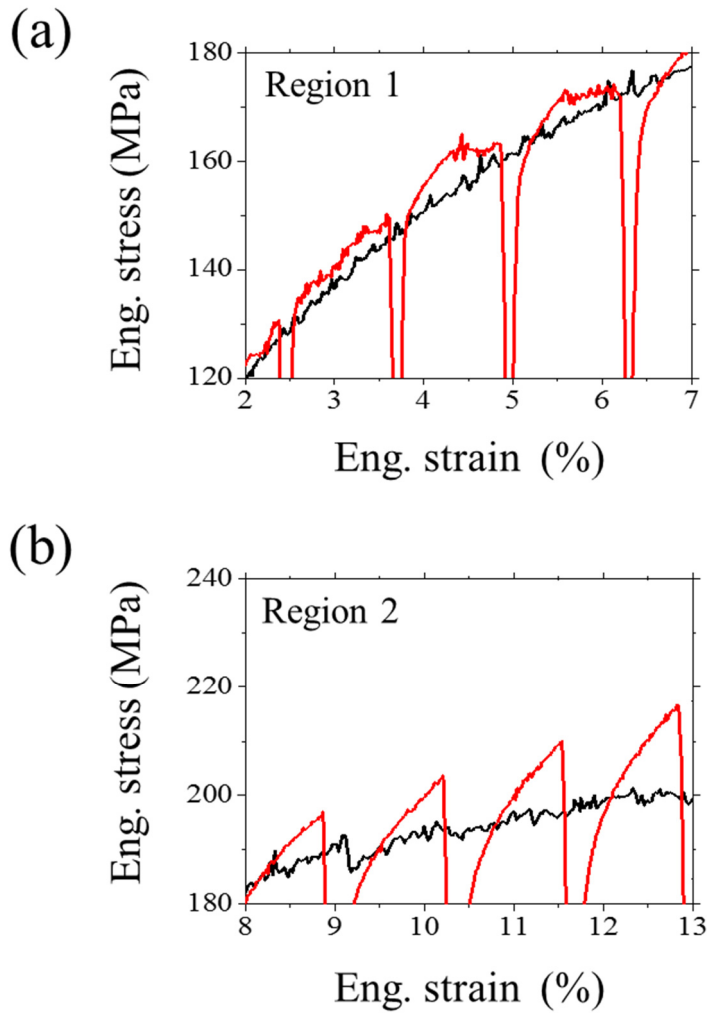


Figure 3. 8 The magnified versions of region 1 and 2 in Figure 3. 7 (a) for the observation of serrated flow in solution treated specimen.

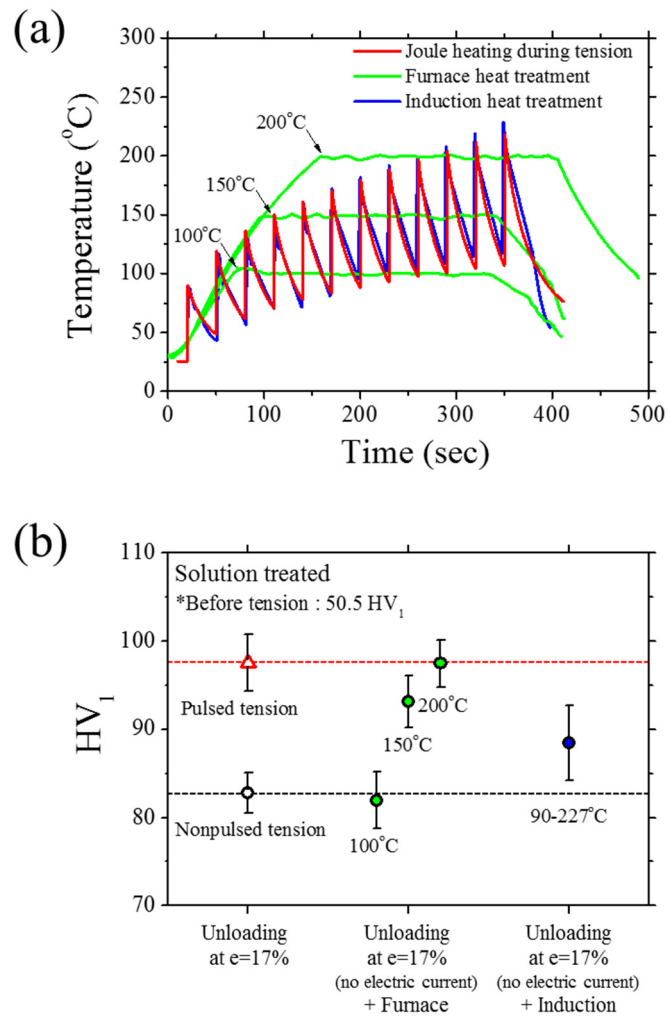


Figure 3. 9 (a) Temperature histories by Joule heating during pulsed tension (in red), furnace heat treatment (in green) and induction heat treatment (in blue) and (b) Vickers hardness (HV) of solution treated specimen at engineering strain of 17% from nonpulsed and pulsed tension and after each heat treatment using specimen strained to 17% from nonpulsed tension.

### **3.5 Annealing during pulsed tension**

In the study of Kim *et al.* (2014a), it was reported that the Al-Mg alloy was annealed due to the annihilation of dislocations when a pulsed electric current was applied during deformation. For this annealing by applying electric current, two kinds of effect were suggested, which are Joule heating effect and electric current effect (electric current-induced annealing) apart from Joule heating. In the present study for the Al-Mg-Si alloy, the flow stress under electric current decreases compared to the baseline in both naturally aged and artificially aged specimens as shown in Figure 3. 7. It can be expected that the annealing could occur by applying electric current during deformation like previous work in Al-Mg alloy. The annealing might also occur in solution treated specimen by applying electric current, even though the flow stress under electric current even increases compared to the baseline due to the formation of early stage of precipitation. Therefore, it should be needed to be checked that the annealing would take place in three types of specimens.

X-ray diffraction is a well-established technique to determine the dislocation density in crystalline materials. X-ray diffraction peak profile is broaden due to the instrumental effect, lattice strain and lattice defects such as dislocation, stacking faults and twin (Wilkins, 1970; Ungár, 2001). In the present study, instrumental effect is assumed to be the same at every measurement with neglecting minor effect of stacking faults and twins. The

dislocation density of the specimen was then qualitatively compared based on the full width at half maximum (FWHM) analysis.

The variation of the diffraction peaks is shown in Figure 3. 10 as an example for FWHM analysis. The three different types of symbols respectively represent the experimental results of the solution treated specimens with the three deformation conditions, which are undeformed, unloaded at the engineering strain of 14% without electric current and unloaded at the engineering strain of 14% with a pulsed electric current. XRD line profiles of deformed cases (red, black lines) are broadened due to deformation-induced dislocation compared to that of undeformed case (blue line). However, the broadening is weaker in specimen with a pulsed electric current compared to that without electric current, which means deformation-induced dislocation is annihilated when electric current was applied. In this way, the dislocation density of the solution treated and naturally aged specimens was compared for the different deformation conditions, which are undeformed, unloaded at the engineering strain of 6 and 14% without electric current and unloaded at the engineering strain of 6 and 14% with a pulsed electric current. For the artificially aged specimen, the elongation at fracture was less than 14%. Therefore, the analysis of dislocation density was conducted for undeformed, unloaded at the engineering strain of 6 % without electric current and unloaded at the engineering strain of 6 % with a pulsed electric current.

The degree of line broadening, i.e. the value of FWHM in all deformed specimens obtained from both nonpulsed and pulsed tensile tests is increased as shown in Figures 3. 11-13. This is caused by the accumulation of plastic deformation in the specimens. It is noted that the values of FWHM of the specimens subjected to pulsed electric current are always lower than those from the nonpulsed tensile test. The deviation of FWHM between nonpulsed and pulsed tension is significantly increased at higher deformation region as shown in Figures 3. 11-12. This suggests that the specimens were annealed due to the annihilation of dislocations when a pulsed electric current was applied during deformation. Note that the annealing is still observed in the solution treated specimen as shown in Figure 3. 11, even though the flow stress under pulsed electric current (Figure 3. 7 (a)) is higher than that in baseline. The deviation of FWHM between nonpulsed and pulsed tension of this alloy is smaller than that obtained from previous work in Al-Mg alloy [25]. This can be understood that the FWHM is also affected by the precipitation as well as the dislocation density during pulsed tension.

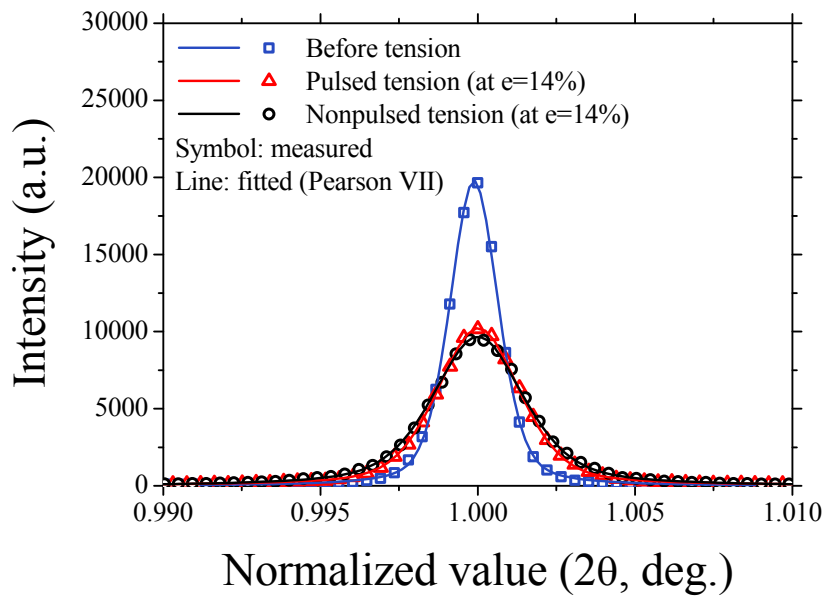


Figure 3. 10 Example of XRD peaks for three case: before tension, tension with/without applying electric current at engineering strain of 14% for solution treated specimen ((110) diffraction peak) as an normalized diffraction angle ( $2\theta$ , deg). The measured data (symbol) is fitted with Pearson VII function (line).

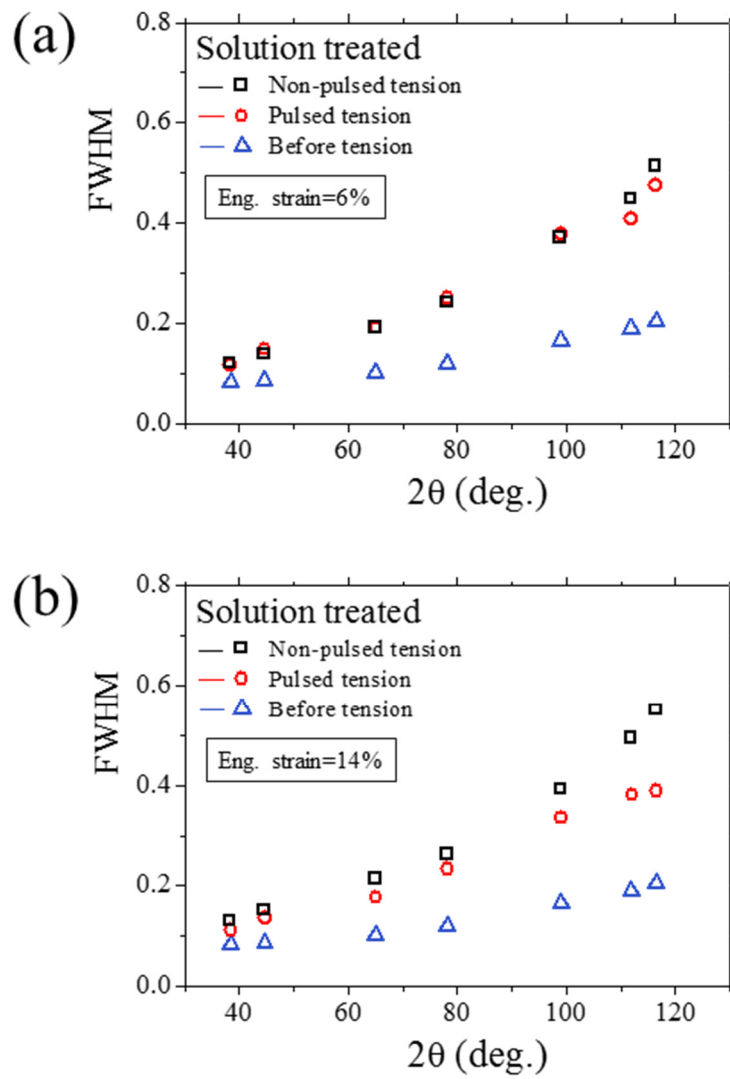


Figure 3. 11 FWHM profiles of solution treated specimen unloaded at engineering strain of (a) 6% and (b) 14%.

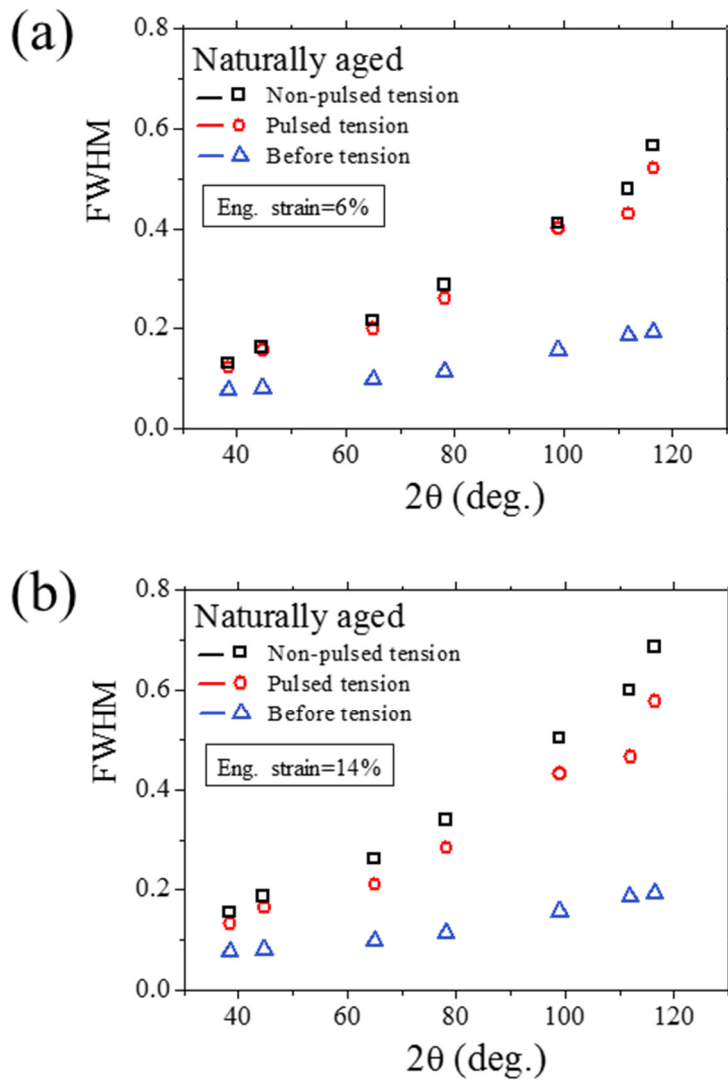


Figure 3. 12 FWHM profiles of naturally aged specimen unloaded at engineering strain of (a) 6% and (b) 14%.

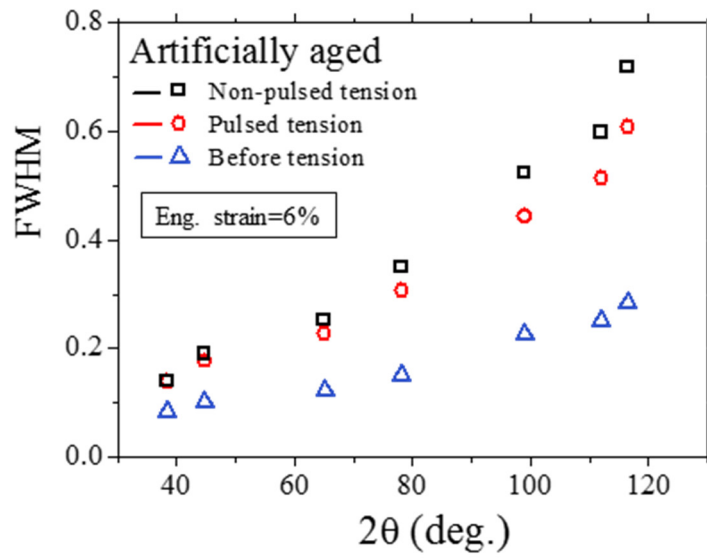


Figure 3. 13 FWHM profiles of artificially aged specimen unloaded at engineering strain of 6%.

### **3.6 Effect of electric current on fracture behavior**

Fractographs after the nonpulsed/pulsed tensile tests for all specimens are described in Figure 3. 14. The fractographs of solution treated and naturally aged specimens shown in Figures 3. 14 (a)-(d) indicate that dimples cover the whole fracture surface after tension in both nonpulsed tensile test and pulsed tensile test. However, brittle intergranular separation in artificially aged specimen was observed after fracture in both nonpulsed and pulsed tension as shown in Figures 3. 14 (e) and (f). The feature of intergranular separation is caused by the formation of void around intermetallic compounds along the grain boundaries, which pre-exist in the artificially aged specimen as shown in Figure 3. 6. Note that the intergranular separation with river line patterns in grain was clearly seen in pulsed tensile specimen as shown in Figure 3. 14 (f). These results suggest that the formation of microvoid around precipitates at grain boundary is accelerated by applying electric current during deformation. This microvoid around precipitates may considerably reduce the bonding force between particles and matrix, which in turn allows the formation of river line pattern thorough grain interior as a crack path. As a result, it may induce earlier fracture in the artificially aged specimen under a pulsed electric current.

In order to observe the microvoid around precipitation, additional microstructural observations of the artificially aged specimens after pulsed tensile test were performed using SEM and TEM. As shown in Figures 3. 15-

16, microvoids exist along grain boundary and around precipitations near the region of fracture surface. In the region right below the fracture surface shown in Figure. 3. 14 (f), the formation of microvoid around precipitations is clearly observed in the specimen.

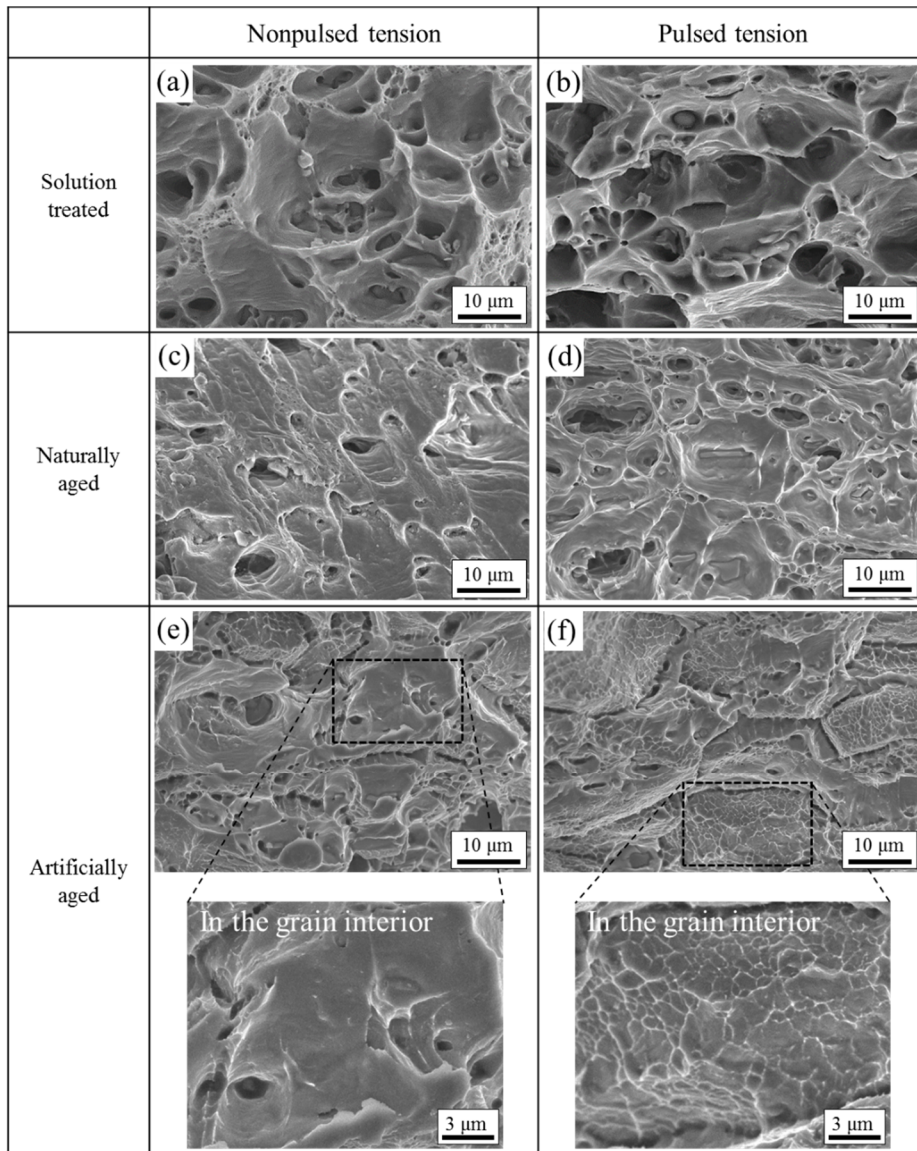


Figure 3. 14 Fracture surface after nonpulsed and pulsed tension for solution treated, naturally aged and artificially aged specimens.

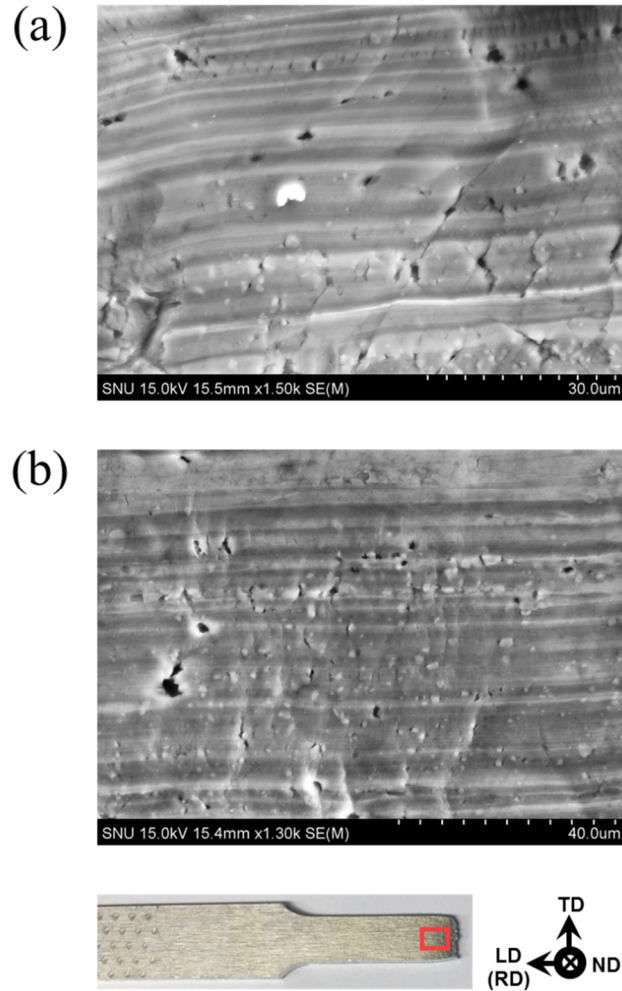
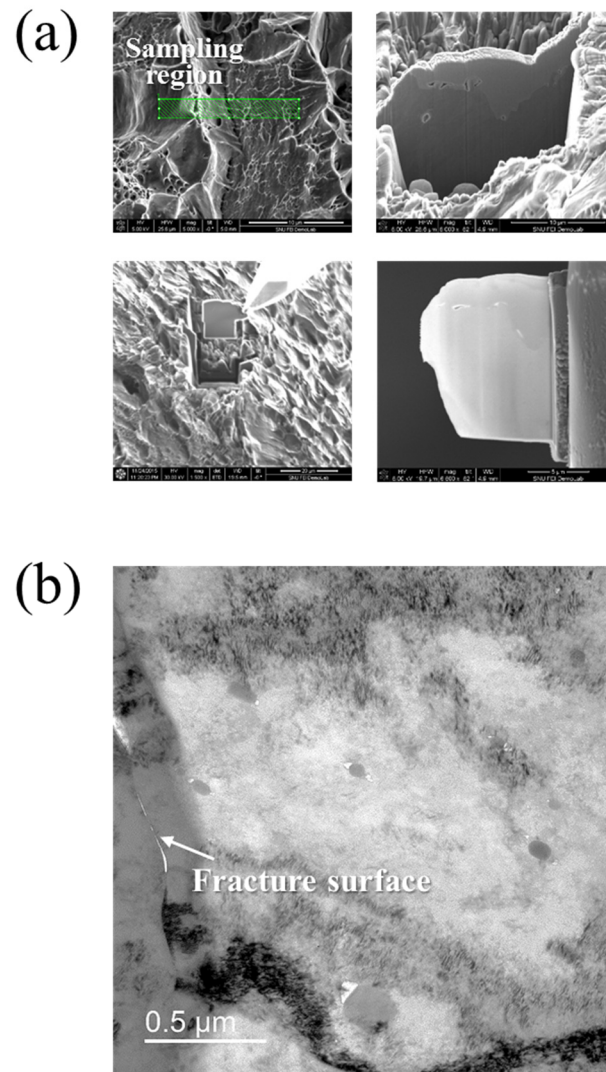


Figure 3. 15 Microstructure near fracture surface of artificially aged specimen after pulsed tension: SEM images showing the microvoid (a) along grain boundary and (b) around precipitations.



### **3.7 Summary**

The electric current-induced deformation behavior of Al-Mg-Si alloy was investigated by uniaxial tension combined with subsequent microstructural observation using SEM, EBSD, XRD and TEM. Three heat treatments of solution treated, naturally aged, and artificially aged conditions were considered. When a pulsed electric current was applied during deformation to solution treated specimen, the elongation increases compared to the result of nonpulsed tension. The flow stress also increases with disappearance of PLC phenomenon by applying electric current. For naturally aged specimen, the elongation increases drastically with softening of the flow stress from the pulsed tensile test. In case of artificially aged specimen, both elongation and flow stress decrease under a pulsed electric current. From XRD analysis, it was observed that thermal and electric current-induced annealing occur in all the specimen at given pulsing condition. Also, the formation of early stage of precipitation from a supersaturated state might be accelerated by applying electric current with a distinct effect of Joule heating, which causes the increase of flow stress and the disappearance of PLC phenomenon in the solution treated specimen. Last, the electric current can accelerate the formation of microvoid around the precipitates. It may induce earlier fracture in the artificially aged specimen under a pulsed electric current, even though thermal and electric current-induced annealing occur by applying electric current. These

experimental observations might be related to the hypothesis that the electric current may enhance the atomic diffusion (Bertolino *et al.*, 2001; Samuel *et al.*, 2010; Kim *et al.*, 2014).

This study provides an important insight to apply electric current-assisted forming. As a positive aspect, recovery occurs due to the electric current-induced annealing as well as the thermal one by applying electric current. This can enlarge the capacity for deformation. In addition, electric current-assisted aging occurs during deformation with less time and lower temperature compared to conventional aging. However, electric current can accelerate the formation of microvoid around the particles, which results in earlier fracture as a negative way in formability. Therefore, electric current should be carefully applied to material considering the microstructural features to obtain enhanced formability without degradation of mechanical property.

### 3.8 References

ASTM B918, 2001. Standard test methods for heat treatment of wrought aluminum alloys, American Society for Testing and Materials ASTM International, West Conshohocken, PA.

Banhart, J., Chang, C.S.T., Liang, Z., Wanderka, N., Lay, M.D.H., Hill, A.J., 2010. Natural ageing in Al-Mg-Si alloys –a process of unexpected complexity. *Adv. Eng. Mater.* 12, 559-571.

Edwards, G.A., Stiller, K., Dunlop, G.L., Couper, M.K., 1998. The precipitation sequence in Al-Mg-Si alloys. *Acta Mater.* 46, 3893-3904.

Gracio, J.J., Barlat, F., Rauch, E.F., Jones, P.T., Neto, V.F., Lopes, A.B., 2004. Artificial aging and shear deformation behavior of 6022 aluminum alloy. *Int. J. Plast.* 20, 427-445.

Kim, M.-J., Han, H.N., Lee, K.H., Oh, K.H., Lee, W.-B., Choi, I.-S., Hong, S.-T., 2014a. Electric current-induced annealing during uniaxial tension of aluminum alloy. *Scr. Mater.* 75, 58–61.

Murayama, M., Hono, K., 1999. Pre-precipitate clusters and precipitation processes in Al-Mg-Si alloys. *Acta Mater.* 47, 1537-1548.

Murayama, M., Hono, K., Saga, M., Kikuchi, M., 1998. Atom probe studies on the early stages of precipitation in Al-Mg-Si alloys. *Mater. Sci. Eng. A* 250, 127-132.

Roh, J.-H., Seo, J.-J., Hong, S.-T., Kim, M.-J., Han, H.N., 2014. The mechanical behavior of 5052-H32 aluminum alloys under a pulsed electric current. *Int. J. Plast.* 58, 84-99.

Roth, J.T., Loker, I., Mauck, D., Warner, M., Golovashchenko, S.F., Krause, A., 2008. Enhanced formability of 5754 aluminum sheet metal using electric pulsing. *Trans. NAMRI/SME*. 36, 405-412.

Salandro, W.A., Khalifa, A., Roth, J.T. 2009. Tensile formability enhancement of magnesium AZ31B-0 alloy using electrical pulsing. *Trans. NAMRI/SME*. 37, 387-394.

Ungár, T., 2001. Dislocation densities, arrangements and character from X-ray diffraction experiments. *Mater. Sci. Eng. A* 309-310, 14-22.

Wilkins, M., *Phys. Status Solidi*. A 2 (1970) 359.

## **Chapter 4**

# **A study on underlying mechanism of electroplasticity**

### **4.1 Introduction**

Recently, various theories have been suggested to explain the mechanism of electroplasticity. In some cases, the mechanical behavior under an electric current may be nicely described based on thermal effect caused by Joule heating without considering the electroplasticity theory (Goldman *et al.*, 1981; Klimov *et al.*, 1984; Magargee *et al.*, 2013). However, it also has been reported that the mechanical behavior under an electric current may not be clearly explained without considering the athermal electroplastic effect. A popular hypothesis to explain athermal effect of electroplasticity is the electron wind effect (Sprecher *et al.*, 1986; Conrad, 2000b; Antolovich *et al.*, 2004). In this hypothesis, the electric current density over  $10^{4-6}$  A/mm<sup>2</sup> may cause atoms to move, which results in interaction between electrons and dislocations. However, the underlying material mechanism associated with electroplasticity still remains controversial.

In previous chapters, electric current-induced phenomena are still clearly observed without surpassing the electric current density region of

electron wind theory. Also, it was confirmed that Joule heating effect cannot solely demonstrate the electroplasticity. Therefore, the objective of present study is to investigate the underlying mechanism of electroplasticity.

## 4.2 Motivation

### 4.2.1 Diffusion kinetics

To sum up all results discussed in previous chapters, electric current can induce the annihilation of dislocation, acceleration of aging process and void formation with a distinct effect of Joule heating. In other words, it can be said that electric current can enhance the diffusion with a distinct effect of Joule heating. To approach the idea to study underlying mechanism of electroplasticity related to diffusion process, diffusion equation is introduced in detail.

Diffusion is a process of movement of molecules or atoms. To jump from lattice site to lattice site, atoms need energy to break bonds with neighbors, and to cause the necessary lattice distortions during jump. In case of vacancy diffusion mechanism, this energy necessary for the jump,  $\Delta G_m^v$ , is called the activation free energy for vacancy motion as shown in Figure 4. 1. It comes from the thermal energy of atomic vibrations. For a simple one-dimensional case, the probability of such fluctuation or frequency of jumps,  $R_j$ , can be described by the Arrhenius equation:

$$R_j = v_0 \exp(-\Delta G_m^v / k_B T)$$

where  $v_0$  is an attempt frequency related to the frequency of atomic vibrations.

The value of  $\nu_0$  is of the order of the mean vibrational frequency of an atom about its equilibrium site (usually taken to be equal to the Debye frequency).

$$R_j = [\text{Frequency of atom vibrations in the diffusion direction } \nu_0] \times [\text{Probability that a given oscillation will move the atom to an adjacent site}]$$

To relate this to the diffusion of atoms, the jump frequency of a given atom in a 3D crystal have to be considered. Moreover, for an atom to jump, there must be a vacancy next to it. The probability for any atom in a solid to move is the product of the probability of finding a vacancy in an adjacent lattice site (fraction of atoms that have a vacancy as a neighbor):

$$\frac{n_{eq}}{N} z = z \exp(-\Delta G_f^v / k_B T)$$

and the rate of jumps of a vacancy (defined by a probability of a thermal fluctuation needed to overcome the energy barrier for vacancy motion):

$$R_j = \nu_0 \exp(-\Delta G_m^v / k_B T).$$

Therefore the rate at which atom jumps from place to place in the crystal is

$$R_j^{atom} = \frac{1}{\tau_j} \approx v_0 z \exp(-\Delta G_f^v/k_B T) \exp(-\Delta G_m^v/k_B T)$$

where  $\tau_j$  is the average time between jumps for atoms.

If the distance atoms cover in each jump is  $a$ , the Einstein relation  $\langle \overrightarrow{\Delta r_i(t)^2} \rangle = 6Dt$  can be used to estimate the diffusion coefficient from the average time between jumps:

$$\begin{aligned} D &= \frac{a^2}{6\tau_j} = \frac{a^2 v_0 z}{6} \exp\left(-\frac{\Delta G_f^v + \Delta G_m^v}{k_B T}\right) \\ &= \frac{a^2 v_0 z}{6} \exp\left(-\frac{\Delta S_f^v + \Delta S_m^v}{k_B}\right) \exp\left(-\frac{\Delta H_f^v + \Delta H_m^v}{k_B T}\right) = D_0 \exp\left(-\frac{E_d}{k_B T}\right) \end{aligned}$$

where  $D_0$  is a parameter of material (both matrix and diffusing species) and is independent of temperature.  $E_d$  is activation energy for diffusion:

$$E_d = \Delta H_f^v + \Delta H_m^v.$$

In the case of interstitial atomic diffusion, activation energy for diffusion is:

$$E_d = \Delta H_m^v.$$

To activate diffusion to occur, the temperature should be high enough to

overcome energy barriers of  $E_d$  for atomic motion. From this derivation of diffusion equation, it can be said that bonding energy of atoms with neighbors is an important factor to activate the diffusion process (Shewmon, 1989).

Now, let's discuss the physical meaning of the atomic bonding energy in detail. Atomic bonding energy is predicted based on interatomic forces that bind the atoms together. Atomic bonding energy is defined from potential energy-atomic distance curve. Consider the interaction of two isolated atoms as they are getting closer from an infinite separation. The net force  $F$  is sum of both attractive force ( $F_A$ ) and repulsive force ( $F_R$ ). When  $F_A$  and  $F_R$  balance, there is no net force i.e.,  $F_A + F_R = 0$ . Then a state of equilibrium exists. This corresponds to equilibrium spacing as indicated in Figure 4. 2. At equilibrium spacing,  $r_0$ , net force is zero and net energy corresponds to atomic bonding energy,  $E_0$ . Finally, the minimum energy  $E_0$  can be derived as the binding energy required to separate two atoms from their equilibrium spacing to an infinite distance apart (Padmavathi, 2011).

On an atomic scale, macroscopic elastic strain is manifested as small changes in the interatomic spacing and the stretching of interatomic bonds. As a consequence, the magnitude of elastic modulus is a measure of the resistance to separation of adjacent atoms i.e., interatomic bonding energy. When material is excited by external energy, it will cause the changes in lattice potential energy state and the average interatomic distance which is decided by the width of the

curve at corresponding energy state. Elastic modulus is closely related to the atomic potential energy, which is derived from the second derivative of the potential energy-atomic distance curve (Padmavathi, 2011; Lian et al., 2013). Therefore, the change in potential energy can induce the change in elastic modulus. In other words, change in potential energy state can be expected by measuring a change in elastic modulus, inversely. Finally, the activation of atomic diffusion related to potential energy state can be discussed by measuring a change in elastic modulus.

Based on this motivation, underlying mechanism is investigated by measuring an elastic modulus during pulsing. Therefore, the change in potential energy state can be expected by measuring a change in elastic modulus, when electric current is applied. Also, the effect of Joule heating is considered separately to investigate the electric current ‘itself’ effect on electroplasticity.

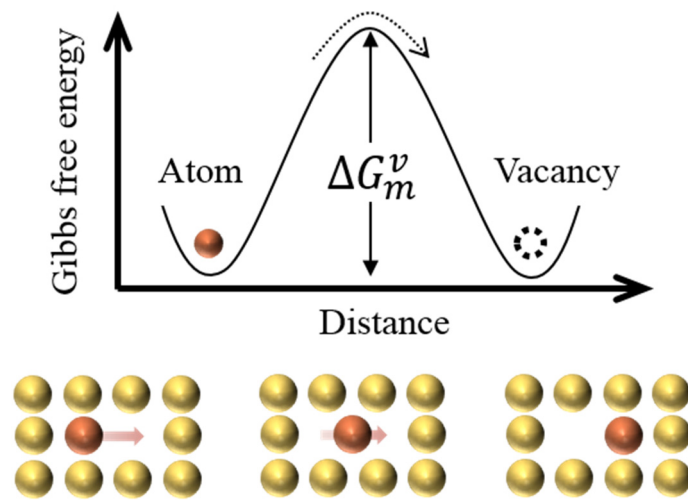


Figure 4.1 Activation energy for diffusion.

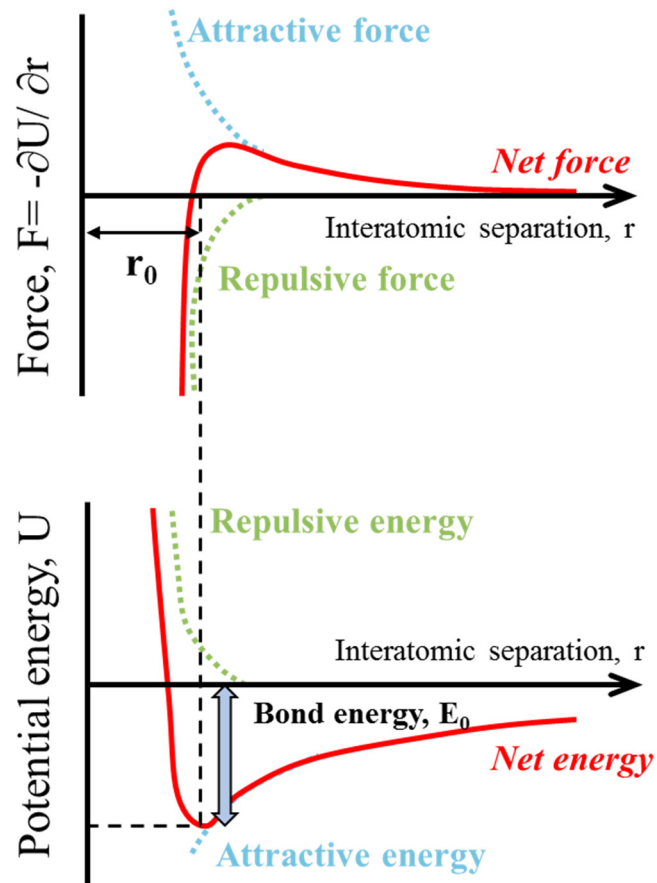


Figure 4. 2 A typical potential well indicating forces and bonding energy.

#### 4.2.2 Measurement of elastic modulus using a laser based ultrasonic technique

In order to measure elastic modulus with a high accuracy, several methods have been frequently considered. When elastic modulus derived from stress-strain curve, an error is introduced by the fact that tensile machine can be deflected under the stress state (Motra et al., 2014). To avoid artifact from tensile machine, there are other well-known methods to measure elastic modulus experimentally including ultrasonic method, resonance frequency method and so on. In present study, electric current is applied to the specimen directly. Therefore, non-contact with a high accuracy measuring technique to detect change in elastic modulus is needed due to insulation problem.

Laser ultrasonics, with optical acoustic generation and detection, has unique advantages over other ultrasonic methods: it is non-contacting, requires no couplant or invasive sample preparation (other than that used in metallurgical analysis), and has the demonstrated capability to probe microstructure on a micron scale (Hurley *et al.*, 2006). As a consequence, laser techniques are highly reproducible, enabling sophisticated data analysis that reveals the state of material microstructure.

The equation of motion in ultrasonic wave is described in detail. The longitudinal wave motion in an elastic body whose length is much greater than its cross-sectional dimension, i.e. rod, is considered. Also, it is assumed that plane cross-sections of the rods remain plane and parallel during the deformation associated with the wave motion. Consider a section of an elastic

rod as shown in Figure 4. 3. Let  $\sigma$  be the normal stress in the  $x$ -direction and  $u$  be the longitudinal displacement of any cross-section in the  $x$ -direction. Both  $\sigma$  and  $u$  depend only on the variables  $x$  and  $t$ .

Summing forces in the  $x$ -direction gives

$$(\sigma + d\sigma)(A + dA) - \sigma A = \rho \bar{A} dx \frac{\partial^2 u}{\partial t^2} \quad (4.1)$$

where  $\rho$  is the mass density of the material, and  $\bar{A}$  is the average cross-sectional area. Equation (4. 1) reduces to

$$\sigma dA + Ad\sigma = \rho \bar{A} dx \frac{\partial^2 u}{\partial t^2}$$

or

$$\frac{\sigma dA + Ad\sigma}{dx} = \rho \bar{A} \frac{\partial^2 u}{\partial t^2} .$$

Taking the limit as  $dx \rightarrow 0$  yields

$$\frac{\partial}{\partial x} (A\sigma) = \rho A \frac{\partial^2 u}{\partial t^2} . \quad (4.2)$$

For  $A = \text{constant}$ , we would have

$$\frac{\partial \sigma}{\partial x} = \rho \frac{\partial^2 u}{\partial t^2}.$$

Now from strength of material theory with small deformations

$$\sigma = E\varepsilon$$

$$\varepsilon = \frac{\partial u}{\partial x},$$

where  $\varepsilon$  is the normal strain in the  $x$ -direction and  $E$  is modulus of elasticity.

Combining (4.3) and (4.4) gives

$$E \frac{\partial^2 u}{\partial x^2} = \rho \frac{\partial^2 u}{\partial t^2},$$

or

$$u_{xx} = \frac{1}{c_L^2} u_{tt}$$

where  $c_L = \sqrt{\frac{E}{\rho}}$  is the velocity of propagation of the longitudinal disturbance

(Rose, 2000).

From this relation, elastic modulus can be derived by measuring a velocity of propagation of the longitudinal wave.

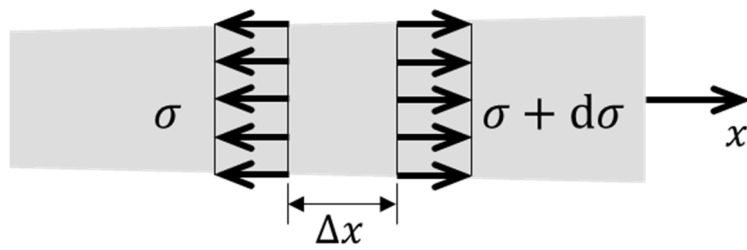


Figure 4. 3 Elastic rod whose length is much greater than its cross-sectional dimension.

## 4.3 Experimental procedures

### 4.3.1 Specimen preparation

A commercial Al-Mg alloy (Al-0.87Mg-0.66Si in wt.%) and Mg-Al-Zn alloy (Mg-3Al-1Zn in wt.%) were selected. For laser based ultrasonic measurement, the specimen was prepared as a rod shape of 1×1×200 mm for Al-Mg alloy and 1.4×1.4×200 mm for Mg-Al-Zn alloy.

To prepare the two kinds of grain size for each alloy, heat treatment was conducted at a temperature of 450°C during 7 hour with a furnace cooling for Al-Mg alloy and at a temperature of 510°C during 1 hour with a furnace cooling for Mg-Al-Zn alloy.

Microstructures were observed by FE-SEM equipped with EBSD system (FE-SEM: SU70, Hitachi, Japan and EBSD: Hikari EBSD detector with TSL OIM 6.1 software, EDAX/TSL, USA). Samples for microstructural analysis were prepared by a standard metallographic grinding technique. After grinding and polishing, they were electropolished with an electrolyte consisting of 10% perchloric acid and 90% ethanol at a temperature of about -20°C and a voltage of 20 V. For EBSD observation, the accelerating voltage of 15 kV and the working distance of 15 mm were used. Critical misorientation angle was set to 10° for grain identification.

#### 4.3.2 Experimental set-up

Mesurement of elastic modulus using laser based ultrasonic was conducted using the experimental set-up described in Figure 4. 4.

Electric current was generated by a NEO-500PS DC power supply (Hyundai, South Korea). Electric current was applied to the rod shaped specimen under a various electric current density based on initial cross sectional area. One side of the specimen was fixed for measure the laser ultrasonic wave accurately and the other side of the specimen was put flexible state to release the thermal expansion to avoid thermal stress in the specimen by applying electric current. At each electric current density, measurement was repeated more than 4 times to obtain average value.

For the generation of ultrasonic wave, Q-switched Nd:YAG laser (Cynosure, USA) was used as shown in Figure 4. 4. Also, the laser ultrasonic detector OFV-505 laser doppler vibrometer system (Ploytec, German) is loacated at the opposite position of the laser pulse shot in order to detect the ultrasonic wave transmitted through the specimen. The accuracy in the wave travel time measurement was few  $\mu$ -sec. The wave signal detected by laser doppler vibrometer system is recorded in the digital oscilloscope (Lecroy, USA).

Temperature of a specimen during a tensile test with a pulsed electric current was measured using a FLIR-E40 infra-red (IR) thermal imaging camera (FLIR, Sweden). Surface of specimen was sprayed with black thermal paint to

stabilize the emissivity and thus to improve the accuracy of temperature measurement.

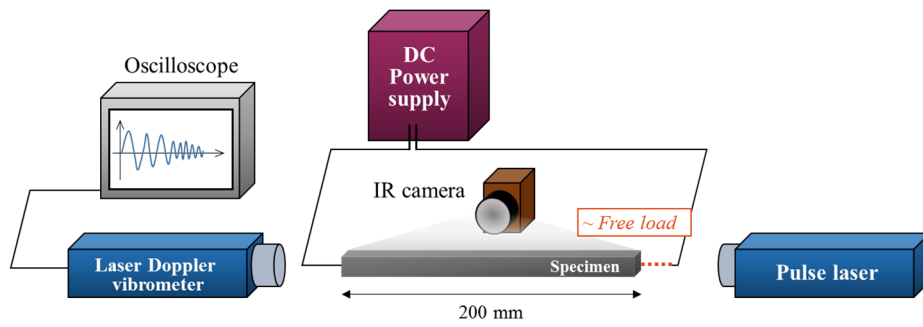


Figure 4. 4 Instrumental set-up for laser based ultrasonic with applying electric current.

## 4.4 Effect of electric current on elastic modulus

### 4.4.1 Temperature dependence on elastic modulus

In order to study the effect of electric current on elastic modulus, two kinds of lightweight alloy were selected, which are Al-Mg alloy (or simply, Al alloy) and Mg-Al-Zn alloy (or simply, Mg alloy). Inverse pole figure maps of Al alloy and Mg alloy are described in Figure 4. 4. The grain size of Al alloy and Mg alloy was  $50 \pm 17 \mu\text{m}$  and  $7 \pm 3 \mu\text{m}$ , respectively. For Al alloy with a grain size of  $50 \mu\text{m}$  is simply called as Al50 and for Mg alloy with a grain size of  $7 \mu\text{m}$  is simply called as Mg07 in this study.

By applying electric current to the specimen, temperature of the specimen increases due to Joule heating. When the temperature increases, the atomic thermal vibrations increase, and this will cause the changes in lattice potential energy state and average atomic distance. So the elastic modulus at corresponding atomic distance will also change.

To consider the Joule heating effect by applying electric current, temperature-dependent elastic modulus for Al50 and Mg07 was checked. The result of the effect of temperature on elastic modulus is shown in Figure 4. 6. It can be seen that the curves demonstrate linear relationship between elastic modulus and temperature. The plot shows approximately straight lines with a constant slope for any given temperature. For Al50 alloy and Mg07 alloy, the slopes of each specimen,  $dE/d(\text{Temp.})$ , are -0.04601 and -0.03451,

respectively. It is well known that a linear dependence has been observed for elastic modulus for aluminum alloy and magnesium alloy above room temperature. Table 4. 1 is the relationship between temperature and elastic modulus for aluminum alloy and magnesium alloy reported in literature. The result from our experiment can be said quite reasonable compared to reported results in literatures.

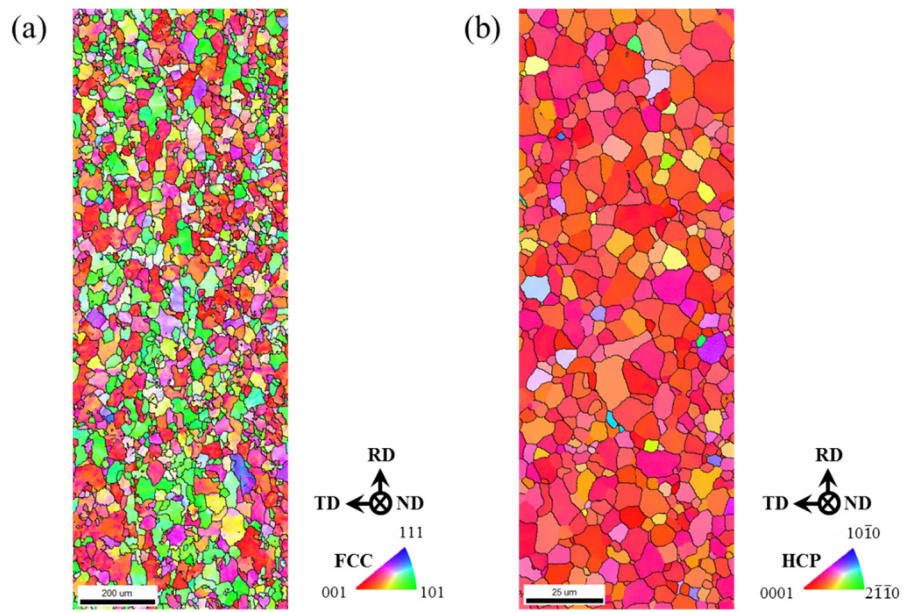


Figure 4. 5 Inverse pole figure ND map of (a) Al50 (grain size:  $50 \pm 17 \mu\text{m}$ ) and (b) Mg07 (grain size:  $7 \pm 3 \mu\text{m}$ ) based on critical misorientation angle of  $10^\circ$ .

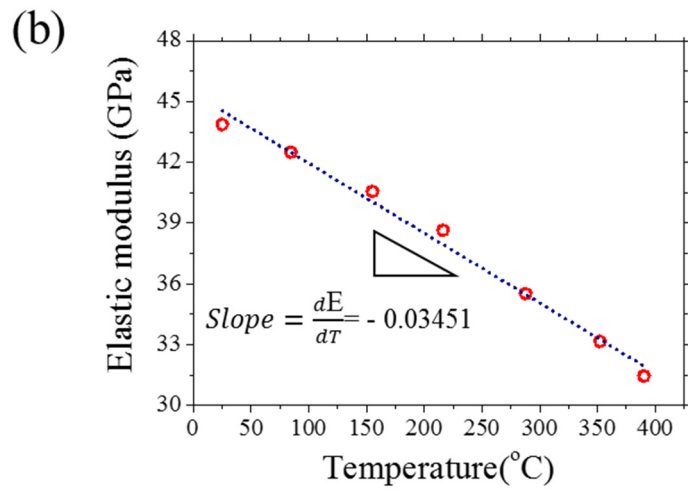
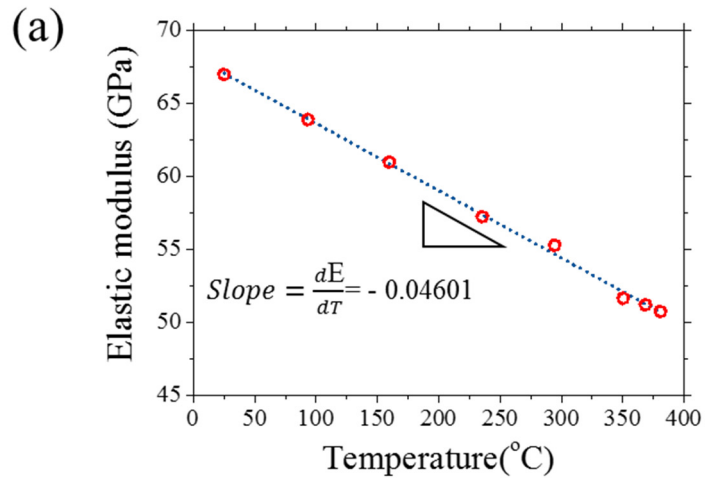


Figure 4. 6 Temperature dependence on elastic modulus of (a) Al50 and (b) Mg07.

	<i>Reference</i>	<i>Slope (dE/dTemp.)</i>	<i>Method of measurement</i>
Aluminum alloy	McLellan <i>et al.</i> , Journal of Physics and Chemistry of Solids, 48 (1987): <b>99.999%Al</b>	-0.0422	Ultrasonic method
	Abe <i>et al.</i> , Journal of Japan Institute of Light Metals, 27 (1977): <b>99.99%Al</b>	-0.0486	Resonance frequency method
	Abe <i>et al.</i> , Journal of Japan Institute of Light Metals, 27 (1977): <b>Al-5wt.%Mg</b>	-0.0476	Resonance frequency method
Magnesium alloy	Watanabe <i>et al.</i> , Scripta Mater., 14 (2004): <b>AZ31</b>	-0.0209	Resonance frequency method
	Freels <i>et al.</i> , The United States department of energy report (2011): <b>AZ31</b>	-0.0383	Resonant ultrasound spectroscopy

Table 4. 1 Linear relationship of temperature dependence on elastic modulus in literature.

#### 4.4.2 Electric current ‘itself’ effect in electroplasticity

When electric current is applied to the specimen, the temperature of the specimen increases immediately even though the pulsing time is quite short as few ms. As mentioned in 4.4.1, elastic modulus will be influenced by increasing temperature. To distinguish the electric current effect on elastic modulus from Joule heating effect by applying electric current, elastic modulus was measured under the state of minimizing the temperature effect.

In order to decide when the ultrasonic wave is generated and detected after applying electric current, rise time of electric current to target value was checked. Figure 4. 7 is the result of rise time to target value in electric current. At various electric current levels of 100-400 A with pulsing time of 0.1 sec, rise time of electric current to target value was confirmed as less than 1 msec. Based on this result, the generation and detection of ultrasonic wave was set to 5 msec after applying electric current to minimize the temperature effect.

For Al50 specimen, electric current density of 50, 100, 150, 200, 250, 300, 350 and 400 A/mm<sup>2</sup> with a pulsing time of 0.1 sec was applied to specimen. Figure 4. 8 describes the result of measured elastic modulus (in blue triangle) of Al50 specimen at 5 msec after applying electric current. When electric current is applied to specimen, the measured elastic modulus decreases with increasing electric current density.

Even though elastic modulus was measured almost immediately after applying electric current, i.e. after 5 msec, temperature is increased which will

cause decrease in elastic modulus. Here, the decrease in elastic modulus due to Joule heating is also considered. Measured temperature under selective electric current density condition is represented as a rod graph in Figure 4. 8 (right axis). The change in elastic modulus due to Joule heating is calculated using measured temperature data based on linear relationship between temperature and elastic modulus shown in Figure 4. 6 (a) and it is described in Figure 4. 8 (in red circle). As shown in Figure 4. 8, all of the measured elastic modulus of Al50 specimen are lower than the calculated elastic modulus due to Joule heating at the region of given electric current density. In other words, electric current can induce additional decrease in elastic modulus in spite of considering the Joule heating effect.

Additionally, in order to check the electric current ‘itself’ effect distinguished from Joule heating effect, measurement of elastic modulus under the fixed electric current density at different pulsing time was also conducted. When electric current density of  $250 \text{ A/mm}^2$  with pulsing time of 0.1 sec was applied to the specimen, the time of generation and detection of ultrasonic wave was set to 0, 5, 25, 50, 75 and 93 during pulsing. Figure 4. 9 describes the result of measured elastic modulus (in blue circle) with the change in elastic modulus due to Joule heating based on linear relationship between temperature and elastic modulus shown in Figure 4. 6 (a) (in red circle). It shows the same result with discussion in Figure 4. 8 that additional change in elastic modulus is observed with a distinct effect of Joule heating, when electric current is applied

to the specimen.

In the same way, measurement of elastic modulus during pulsing was conducted for magnesium alloy. For Mg07 specimen, electric current density of 40, 80, 100, 120, 140, 160, 180, 200, 230 and 255 A/mm<sup>2</sup> with a pulsing time of 0.1 sec was applied to specimen. Figure 4. 10 represents the result of measured elastic modulus (in blue triangle) of Mg07 specimen at 5 msec after applying electric current. When electric current is applied to specimen, the measured elastic modulus decreases with increasing electric current density, which is the same trend observed in Al50 specimen. In the same way of considering the temperature effect on elastic modulus in Al50 specimen, the change in elastic modulus due to Joule heating was calculated using measured temperature based on linear relationship between temperature and elastic modulus shown in Figure 4. 6 (b) and it is described in Figure 4. 10 (in red circle). All of the measured elastic modulus of Mg07 alloy are lower than calculated elastic modulus due to Joule heating at the region of given electric current density.

Measured elastic modulus during applying electric current includes mainly two effects. One is the Joule heating effect and the other is electric current 'itself' effect. As shown in Figures 4. 8-10, all measured elastic modulus are lower than that of calculated elastic modulus considering the Joule heating effect in both Al alloy and Mg alloy. In other words, electric current can induce additional decrease in elastic modulus more than Joule heating effect. It means

that when electric current is applied, the change of lattice potential energy can be more intensified to the direction of weaken the elastic modulus in comparison with the change of lattice potential energy due to temperature effect. When the potential energy is changed in the way of lowering the elastic modulus additionally as distinct from Joule heating effect by applying electric current, the atomic bonding energy can be decreased which results in easy state to diffuse.

Therefore, it can be suggested that electric current can induce the additional change in lattice potential energy with a discrete effect of Joule heating, which can cause the enhance of diffusion by weakening the atomic bonding force.

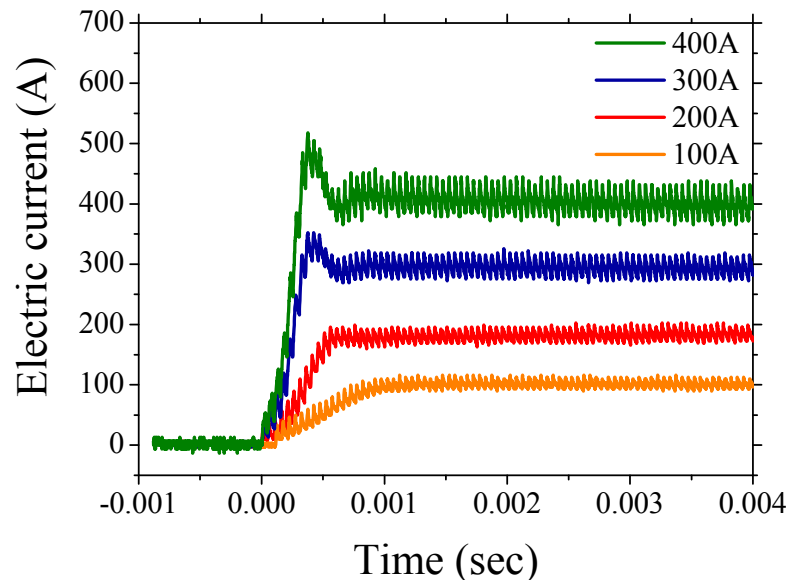


Figure 4. 7 Rise time of electric current to target value under the various electric current condition.

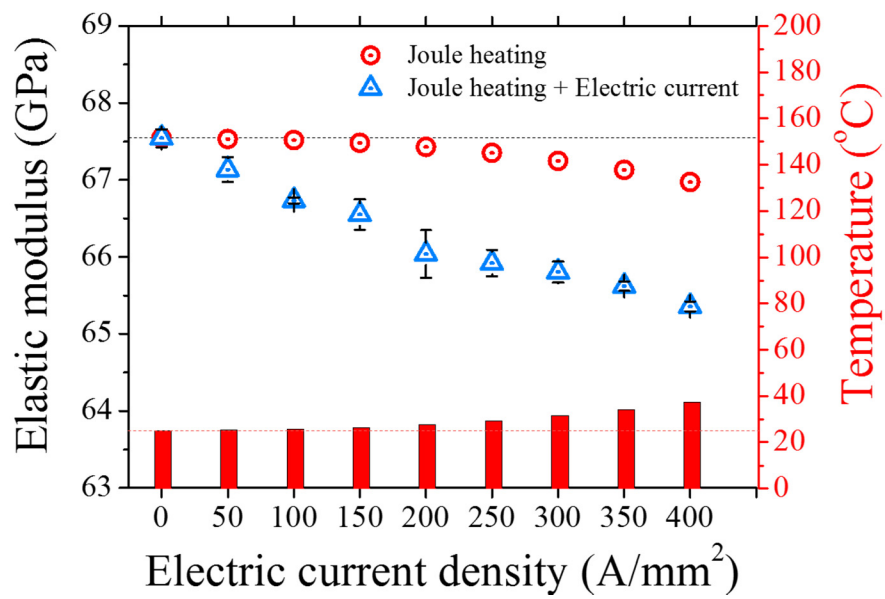


Figure 4. 8 Measured elastic modulus (in blue triangle, left-axis) and calculated elastic modulus due to Joule heating (in red circle, left-axis) with measured temperature (in red rod, right-axis) under the various electric current density for Al50 specimen.

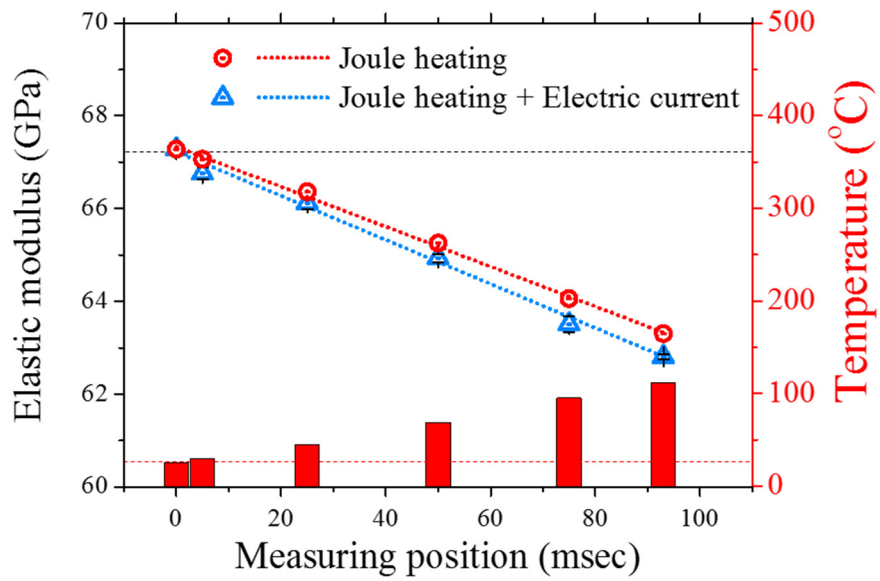


Figure 4. 9 Measured elastic modulus (in blue triangle, left-axis) and calculated elastic modulus due to Joule heating (in red circle, left-axis) with measured temperature (in red rod, right-axis) under the various measuring position at fixed electric current density of  $250 \text{ A/mm}^2$  for aluminum alloy.

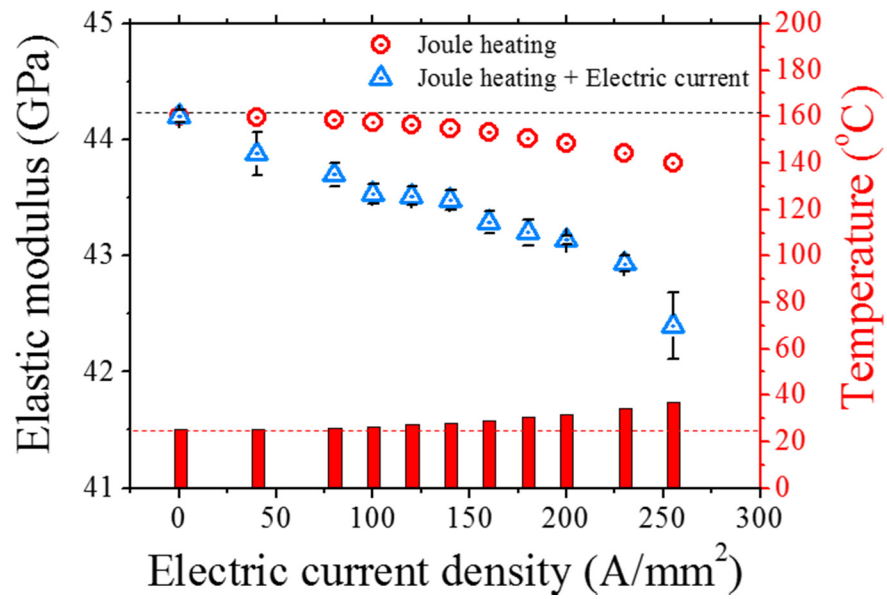


Figure 4. 10 Measured elastic modulus (in blue triangle, left-axis) and calculated elastic modulus due to Joule heating (in red circle, left-axis) with measured temperature (in red rod, right-axis) under the various electric current density for Mg07 specimen.

## **4.5 Origin of decrease in elastic modulus in electroplasticity**

### 4.5.1 Grain boundary and elastic modulus

In previous chapter, it was confirmed that electric current can induce additional decrease in elastic modulus with a distinct effect of Joule heating, which means the decrease in lattice bonding force additionally from temperature effect by applying electric current.

It is reported that grain boundary can influence the elastic modulus. Some experimental results indicate a decrease in elastic modulus with a decreasing grain size. It is more significantly observed in nanocrystalline material (Kim and Bush, 1999; Watanabe et al, 2014). Even though bulk specimen in present study is the sized in millimeter, grain boundary can influence the material property, i.e. elastic modulus, when electric current is applied. So, effect of grain boundary on decrease in elastic modulus by applying electric current is investigated.

To investigate the effect of grain boundary on decrease in elastic modulus by applying electric current, specimens with different grain size for each alloy were additionally prepared through heat treatment. For aluminum alloy, A150 specimen was placed in furnace at a temperature of 450°C during 7 hour followed by furnace cooling. For magnesium alloy, Mg07 specimen was heat treated at a temperature of 510°C during 1 hour with a furnace cooling. The

microstructure for heat treated specimens are shown in Figure 4. 11. The grain size after heat treatment of Al50 and Mg07 are  $100 \pm 36 \mu\text{m}$  and  $344 \pm 112 \mu\text{m}$ , respectively. The specimens after heat treatment of Al50 and Mg07 are simply called as Al100 and Mg344, respectively.

Bulk specimen is considered as composite material with a grain boundary phase and a matrix (inter-grain) phase. It can be assumed that grain boundaries are like thin layers. A simple model of specimen can be considered as follows based on this assumption (Figure 4. 12). Each grain is assumed to be a regular hexahedron with a side length as grain diameter. Grain boundary thickness is assumed to be 5 nm. The volume fraction of grain boundary ( $f_{gb}$ ) and matrix ( $f_m$ ) can be expressed as follow

$$f_{gb} = \frac{(\text{The number of grain in bulk specimen}) \times (\text{volume of grain boundary in unit cell})}{\text{Total volume of bulk specimen}}$$

and

$$f_m = 1 - f_{gb} .$$

The number of grain in bulk specimen can be calculated based on the grain size considering the size of bulk specimen ( $1 \times 1 \times 200 \text{ mm}$  for Al alloy and  $1.4 \times 1.4 \times 200 \text{ mm}$  for Mg alloy). From this simple model, calculated  $f_{gb}$  and  $f_m$  for Al50, Al100, Mg07 and Mg344 are listed in Table 4. 2.

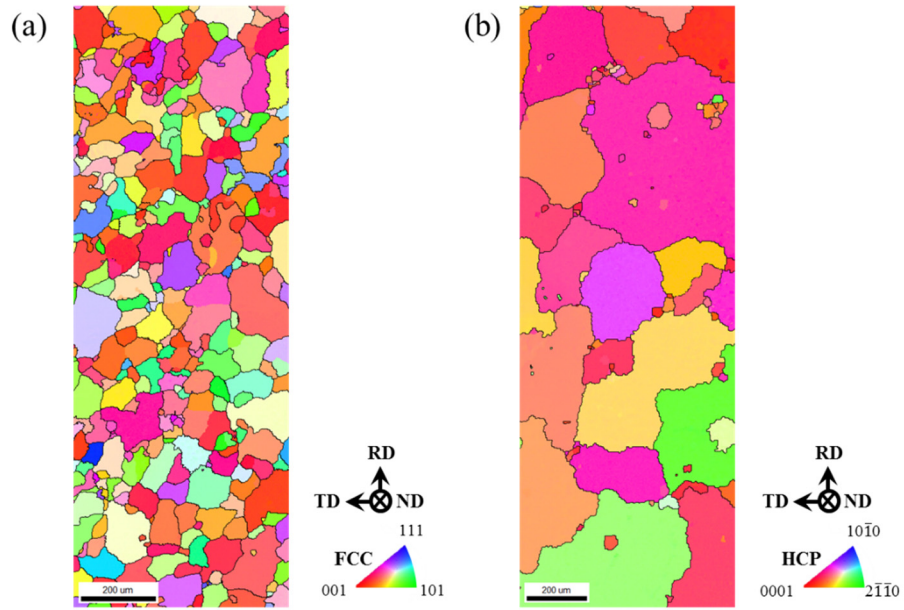


Figure 4. 11 Inverse pole figure ND map of (a) Al100 (grain size:  $100 \pm 36 \mu\text{m}$ ) and (b) Mg344 (grain size:  $344 \pm 112 \mu\text{m}$ ) based on critical misorientation angle of  $10^0$ .

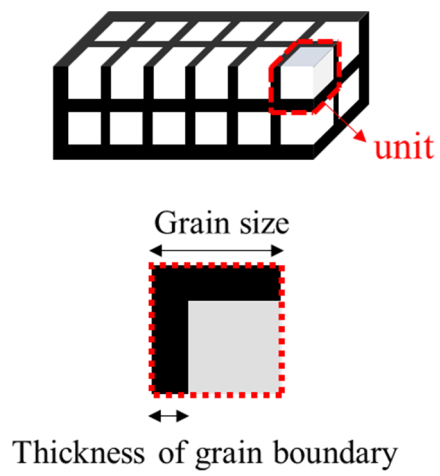


Figure 4. 12 A simple model of specimen for calculating  $f_{gb}$  and  $f_m$  ( $f_{gb}$ : volume fraction of grain boundary,  $f_m$ : volume fraction of matrix).

	$f_{gb}$	$f_m$
A150	0.0003	0.9997
A1100	0.00015	0.99985
Mg07	0.00214	0.99786
Mg344	0.000044	0.999956

Table 4. 2 Volume fraction of grain boundary and matrix.

#### 4.5.2 Effect of grain boundary on temperature dependence on elastic modulus

To consider the Joule heating effect by applying electric current, the characterization of temperature-dependent elastic modulus for Al50 and Mg07 was checked in chapter 4.4.1. In the same way, temperature dependence on elastic modulus for Al100 and Mg344 was also checked to consider the effect of grain boundary as shown in Figure 4. 13.

The curves of Al100 and Mg344 also demonstrate linear relationship between elastic modulus and temperature like those of Al50 and Mg07. For Al100 alloy and Mg344 alloy, the slopes of each specimen,  $dE/d(\text{Temp.})$ , are -0.03952 and -0.02759, respectively (Table 4. 3). By comparing with the result in smaller grain size for each alloy, the absolute value of slope,  $dE/d(\text{Temp.})$ , decreases with decrease in grain size. From this result, it can be said that grain boundary influences the bulk elastic modulus.

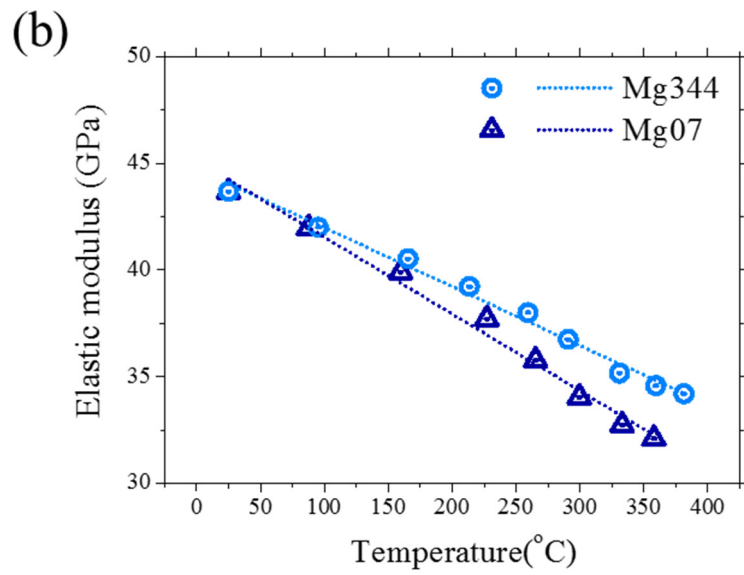
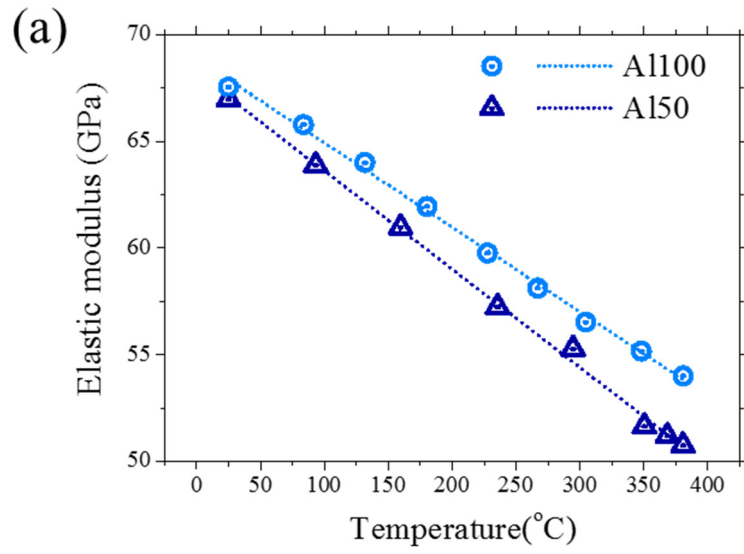


Figure 4. 13 Temperature dependence on elastic modulus of (a) Al150, Al100 and (b) Mg07, Mg344.

	$dE/d(Temp.)$
A150	-0.04601
Al100	-0.03952
Mg07	-0.03602
Mg344	-0.02759

Table 4. 3 Linear relationship of temperature dependence on elastic modulus.

#### 4.5.3 Electric current ‘itself’ effect in electroplasticity under the different grain size

In 4.4.2, electric current ‘itself’ effect in electroplasticity was investigated. Next, effect of grain boundary on electric current ‘itself’ effect in electroplasticity was studied for each alloy with different grain size of specimen as shown in previous chapter. Before discussing the effect of grain boundary on electroplasticity, effect of electric current in electroplasticity in bigger grain size was described first.

To measure elastic modulus in bigger grain size for each alloy, the generation and detection of ultrasonic wave was also set to 5 msec after applying electric current to minimize the temperature effect on elastic modulus.

For Al100 specimen, electric current density of 50, 100, 150, 200, 250, 300, 350 and 400 A/mm<sup>2</sup> with a pulsing time of 0.1 sec was applied to specimen, which is the same pulsing condition with Al50. Figure 4. 13 describes the result of measured elastic modulus (in blue triangle) of Al100 specimen at 5 msec after applying electric current. When electric current is applied to specimen, the measured elastic modulus decreases with increasing electric current density. The decrease in elastic modulus due to Joule heating is also considered. Measured temperature under selective electric current density condition was represented as rod graph in Figure 4. 13 (right axis). The temperature rise due to Joule heating in Al100 was same with the result in Al50, due to the identical pulsing condition and the same dimension of the sample. The change in elastic

modulus due to Joule heating was calculated using measured temperature data based on linear relationship between temperature and it is described in Figure 4. 13 (in red circle). As shown in Figure 4. 13, all of the measured elastic modulus of Al100 specimen are lower than the calculated elastic modulus due to Joule heating at the region of given electric current density. In other words, electric current can induce additional decrease in elastic modulus in spite of considering the Joule heating effect even in bigger grain size compared to Al50.

For Mg344 specimen, electric current density of 40, 80, 100, 120, 140, 160, 180, 200, 230 and 255 A/mm<sup>2</sup> with a pulsing time of 0.1 sec was applied to the specimen, which is the same pulsing condition with Mg07. Figure 4. 14 represents the result of measured elastic modulus (in blue triangle) of Mg344 specimen after 5 msec after applying electric current. Likewise other specimens in Al50, Al100 and Mg07, the measured elastic modulus decreases with increasing electric current density, when electric current is applied to specimen. The change in elastic modulus due to Joule heating was also calculated using measured temperature data based on linear relationship between temperature and elastic modulus shown in Figure 4. 12 (b) and it is described in Figure 4. 14 (in red circle). All of the measured elastic modulus of Mg344 alloy are lower than calculated elastic modulus due to Joule heating at the region of given electric current density.

From these results in Figures 4. 13 and 14 with the bigger grain size for each alloy, it was confirmed again that electric current can induce decrease in

elastic modulus more than Joule heating effect even in bigger grain size compared to the result in Figures 4. 8 and 10. It means that the change of lattice potential energy can be more intensified to the direction of weaken the elastic modulus in comparison with the change of lattice potential energy due to temperature effect, when electric current is applied. Therefore, the suggestion that mentioned in previous chapter in 4.4.2, is confirmed again that electric current can induce the additional change in lattice potential energy with a distinct effect of Joule heating, which can cause the enhance of diffusion process by weakening the atomic bonding force.

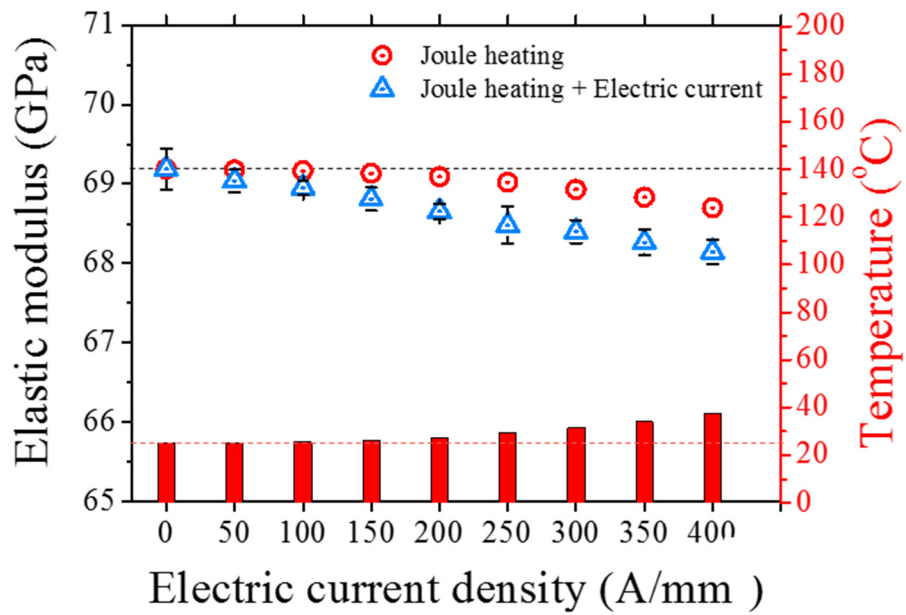


Figure 4. 14 Measured elastic modulus (in blue triangle, left-axis) and calculated elastic modulus due to Joule heating (in red circle, left-axis) with measured temperature (in red rod, right-axis) under the various electric current density for Al100 specimen.

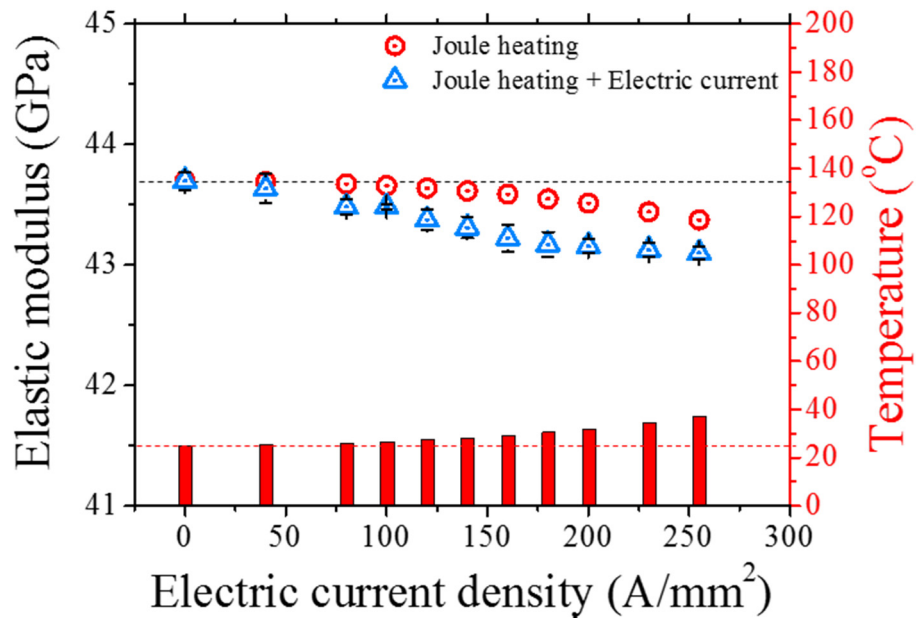


Figure 4. 15 Measured elastic modulus (in blue triangle, left-axis) and calculated elastic modulus due to Joule heating (in red circle, left-axis) with measured temperature (in red rod, right-axis) under the various electric current density for Mg344 specimen.

#### 4.5.4 Effect of grain boundary in electroplasticity

In order to investigate the effect of grain boundary on electric current 'itself' effect in elastic modulus, the measured elastic modulus was represented as an normalized value as shown in Figures 4. 16 and 17.

In Figure 4. 16, the measured elastic modulus of Al50 and Al100 shown in Figures 4. 8 and 14 under the various electric current density were represented in normalized value. The decrease in normalized value of Al50 due to Joule heating (symbol : ▲) with increasing electric current density is stiffer than that of Al100 (symbol : ●). Considering the almost identical increase in temperature due to the same pulsing condition, this difference of decreasing rate of elastic modulus by increasing electric current density between Al50 and Al100 is caused by the different temperature dependence on elastic modulus as discussed in 4.5.2. All of the measured elastic modulus of Al50 (symbol : ▲) is lower than that of Al100 (symbol : ●) in the given range of electric current density. It means that grain boundary could affect the decrease in elastic modulus by applying electric current. Also, the effect of grain boundary on decrease in elastic modulus increases by applying higher electric current density.

Figure 4. 17 shows the normalized elastic modulus of Mg07 and Mg344 using the data shown in Figures 4. 10 and 4. 15 under the various electric current density. The decrease in normalized value of Mg07 due to Joule heating (symbol : ▲) with increasing electric current density is stiffer than that of

Mg344 (symbol : ●), which is the same trend observed in aluminum alloy. Likewise in aluminum alloy, the different decreasing rate in elastic modulus with increasing electric current density due to Joule heating between Mg07 and Mg344 is caused by the different temperature dependence on elastic modulus as discussed in 4.5.2. All of the measured elastic modulus of Mg07 (symbol : ▲) is lower than that of Mg344 (symbol : ⊙) in the given range of electric current density. From this result, effect of grain boundary on decrease in elastic modulus is confirmed again in magnesium alloy. Also, the effect of grain boundary on decrease in elastic modulus increases by applying higher electric current density.

By comparing the normalized elastic modulus using different grain size of specimen, the decrease in elastic modulus by applying electric current increases with increasing the fraction of grain boundary in both aluminum and magnesium alloy. In addition, effect of grain boundary on decrease in elastic modulus is intensified by increasing electric current density. From these results, it can be said that the grain boundary region is dominantly influenced by applying electric current to decrease in elastic modulus, even though the volume fraction of grain boundary in bulk sized specimen is quite small as  $10^{-3}$ - $10^{-1}$  %.

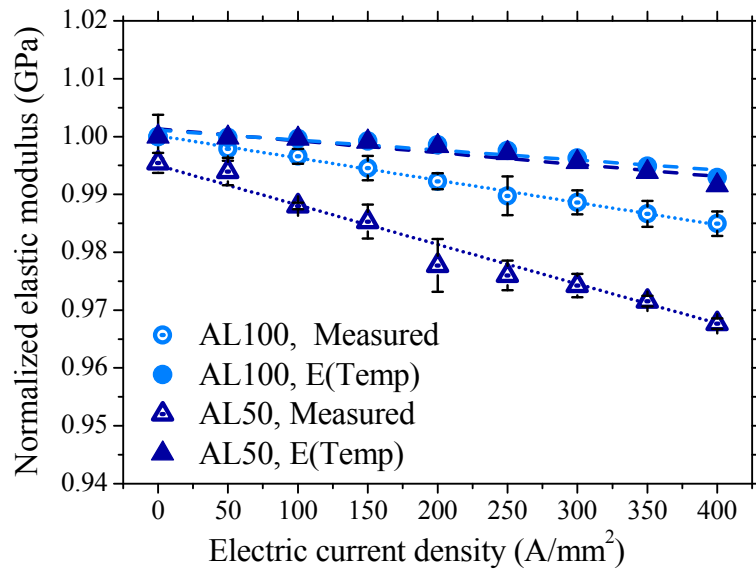


Figure 4. 16 Normalized elastic modulus of Al50 and Al100. The measured values (Al50 : ▲, Al100 : ○) and the calculated values due to Joule heating (Al50 : ▲, Al100 : ●) are represented.

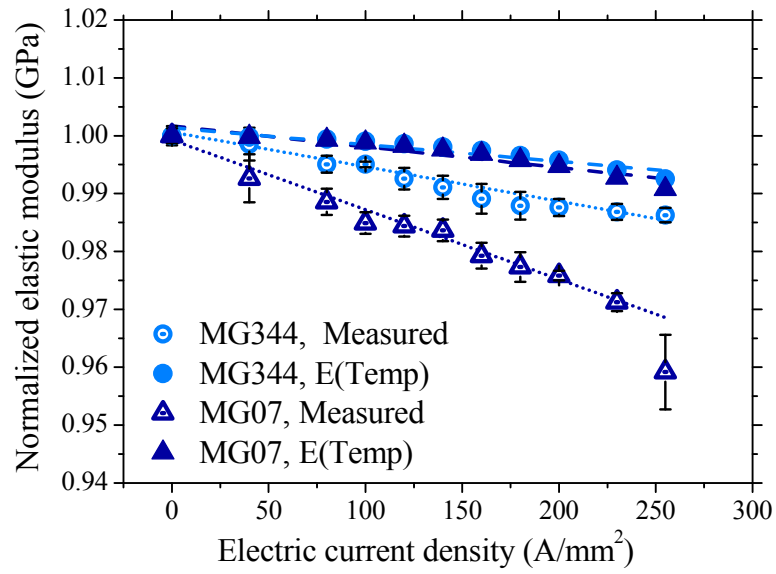


Figure 4. 17 Normalized elastic modulus of Mg07 and Mg344. The measured values (Mg07 :  $\blacktriangle$ , Mg344 :  $\odot$ ) and the calculated values due to Joule heating (Mg07 :  $\blacktriangle$ , Mg344 :  $\bullet$ ) are represented.

## 4.6 Summary

Underlying mechanism of electroplasticity was investigated based on effect of electric current on elastic modulus. In previous chapters, it was suggested that electric current can enhance the atomic diffusion with a distinct effect of Joule heating. For diffusion, bonding energy of atoms with neighbors is an important factor to activate the diffusion. Bonding energy is closely related to the lattice potential energy. When material is excited by external energy, it will cause the changes in lattice potential energy. The elastic modulus is closely related to material's potential energy, which is derived from the second derivative of the potential energy-atomic distance curve. Therefore, the change in potential energy can be expected by measuring an elastic modulus.

In the present study, to investigate the underlying mechanism of electroplasticity by measuring an elastic modulus, laser ultrasonic method was used as a non-contact with high accuracy measuring technique to detect change in elastic modulus. Joule heating effect on elastic modulus was also considered separately by measuring a linear dependence on elastic modulus with increasing temperature.

Firstly, electric current 'itself' effect in electroplasticity was investigated under the various electric current density conditions. Measured elastic modulus during applying electric current includes mainly two effects. One is the Joule heating effect and the other is electric current 'itself' effect. All measured elastic

modulus are lower than that of calculated elastic modulus considering the Joule heating effect in both aluminum alloy and magnesium alloy. In other words, electric current can induce additional decrease in elastic modulus more than Joule heating effect. It means that when electric current is applied, the change of lattice potential energy can be more intensified to the direction of weaken the elastic modulus in comparison with the change of lattice potential energy due to temperature effect. When the potential energy curve is changed in the way of lowering the elastic modulus additionally as distinct from Joule heating effect by applying electric current, the atomic bonding energy can be decreased which results in easy state to diffuse. Therefore, it can be suggested that electric current can induce the additional change in lattice potential energy with a discrete effect of Joule heating, which can cause the enhance of diffusion by weakening the atomic bonding force.

Secondly, effect of grain boundary on electric current ‘itself’ effect in electroplasticity was studied for each alloy between small and big grain size of specimen. By comparing the normalized elastic modulus using different grain size of specimen, elastic modulus by applying electric decreases more with increasing the fraction of grain boundary in both aluminum alloy and magnesium alloy. In addition, this effect of grain boundary on decrease in elastic modulus is intensified by increasing electric current density. From these results, it can be said that the grain boundary is dominantely influenced by applying electric current to decrease in elastic modulus, even though the

volume fraction of grain boundary in bulk sized specimen is quite small as  $10^{-3}$ - $10^{-1}$  %.

## 4.7 References

- Abe, K., Tanji, Y, Yoshinaga, H., Morozumi, S., J. Jap. Inst. Light Met. 27 (1977) 279.
- Antolovich, S.D., Conrad, H., Mater. Manuf. Proc. 19 (2004) 587.
- Conrad, H., Mater. Sci. Eng. A 287 (2000) 276.
- Freels, M., Liaw, P.K., Garlea, E., Morrell, J.S., Radiovic, M., Report for the U.S. department of energy (2011).
- Goldman, P.D., Motowidlo, L.R., Galligan, J.M, Scr. Metall. 15 (1981) 353.
- Hurley, D.H., Wright, O.B., Matsuda, O., Suzuki, T., Tamura, S., Sugawara, Y., Phys. Rev. B 73 (2006) 125403.
- Kim, H.S., Bush, M.B., Nanostruct. Mater. 11 (1999) 361.
- Klimov, K.M., Novikov, I.I., Strength Mater. 16 (1984) 270.
- Lian, J., Lee, S.-W., Valdevit, L., Baskes, M.I., Greer, J.R., Scripta Mater. 68 (2013) 261.
- Magargee, J., Morestin, F., Cao, J., ASME J. Eng. Mater. Technol. 135 (2013) 041003-1-10.
- McLellan, R.B., Ishikawa, T., J. Phys. Chem. Solids 48 (1987) 603.
- Motra, H.B., Hildebrand, J., Dimmig-Osburg, A., Eng. Sci. Technol. 17 (2014) 260.
- Padmavathi, D.A., Mater. Sci. Appl. 2 (2011) 97.
- Rose, J.L., J. Acoust. Soc. Am. 107 (2000) 1807.

Shewmon, P., Diffusion in solids, 2nd Edn. Mine. Met. Mater. Soc., warrendale, Pennsylvania (1989).

Sprecher, A.F., Mannan, S.L., Conrad, H., Acta Metall. 34 (1986) 1145.

Watanabe, H., Mukai, T., Sugioka, Masami, Ishikawa, K., Scripta Mater. 51 (2004) 291.

## **Chapter 5**

### **Total conclusion**

Electrically-assisted forming is a promising alternative forming technique, in which the mechanical property of a metal alloy is altered by simply applying electricity to the target alloy during deformation. The reduced flow stress and increased ductility, which are often called the electroplastic effect, are generally observed in electrically-assisted deformation.

Various theories have been suggested to explain the mechanism of electroplasticity. In some cases, the mechanical behavior under an electric current may be nicely described based on thermal effect caused by resistive heating without considering the electroplasticity theory. However, it also has been reported that the mechanical behavior under an electric current may not be clearly explained without considering the athermal electroplastic factor of the electron wind effect. However, the underlying material mechanism associated with electroplasticity still remains controversial. Also, even though a number of researches have been conducted on the effect of electric current on deformation, the amount of experimental data to clearly understand the phenomenon of electroplasticity is not sufficient yet.

The objective of present study is mainly consisted of two part. Firstly, the effect of electric current on lightweight alloy is investigated based on

microstructural analysis. Three kinds of alloy system are selected, which are Al-Mg alloy as a non-heat treatable alloy system and Al-Mg-Si alloy as a representative age hardening alloy system. Based on understanding of electric current-assisted phenomenon, finally, the underlying mechanism of electroplasticity is suggested.

Firstly, electroplasticity in non-heat treatable aluminum alloy was investigated with subsequent microstructural analysis. Al-Mg alloy was selected as a non-heat treatable aluminum alloy. The elongation of both as-received (H32 treated) and cold-rolled specimens increases drastically with softening of flow stress from the pulsed tensile test. Recrystallization and grain growth were observed after fracture from the pulsed tensile test and it could be expected that thermal effect would be dominant after severe necking. However, increase of formability before severe necking was still observed strongly and it could not be explained by usual thermal effect. It was confirmed that the recovery occurs at a given electric pulsing condition comparing with nonpulsed tensile test. This study proves that the electric current could induce annealing as a distinct role from Joule heating.

Secondly, electroplasticity in precipitation hardened aluminum alloy was investigated with subsequent microstructural analysis. Al-Mg-Si alloy was selected as precipitation hardened aluminum alloy. Specimens with three different heat treatments of solution treated, naturally aged, and artificially aged conditions are prepared. In solution treated specimen, the elongation and flow

stress increase by applying pulsed electric current during plastic deformation compared to the result of nonpulsed tension. The Portevin-Le Chaterlier (PLC) phenomenon, which is clearly observed in nonpulsed tensile test, nearly disappears by applying electric current during deformation. For the naturally aged specimen, the flow stress decreases while the elongation significantly increases under a pulsed electric current compared to the result of nonpulsed tensile test. In case of artificially aged specimen, both elongation and flow stress decrease under a pulsed electric current. From XRD analysis, it was observed that thermal and electric current-induced annealing occur in all the specimen under the electric current. Also, the formation of early stage of precipitation from a supersaturated state might be accelerated by applying electric current with a distinct effect of Joule heating, which causes the increase of flow stress and the disappearance of PLC phenomenon in the solution treated specimen. In addition, the microstructural observation shows that electric current accelerates the formation of microvoid around the precipitates at grain boundary, which results in earlier fracture in the artificially aged specimen. These experimental observations might be related to the hypothesis that the electric current may enhance the atomic diffusion.

Lastly, underlying mechanism of electroplasticity was investigated based on effect of electric current on elastic modulus. From the results discussed in Al-Mg alloy and Al-Mg-Si alloy, it was suggested that electric current can enhance the atomic diffusion with a distinct effect of joule heating. For

diffusion, bonding energy of atoms with neighbors is an important factor to activate the diffusion process. Bonding energy is closely related to the lattice potential energy. When material is excited by external energy, it will cause the changes in lattice potential energy. The elastic modulus is related to the shape of material's potential energy, which is derived from the second derivative of the potential energy-atomic distance curve. Therefore, the change in potential energy can be expected by measuring an elastic modulus.

Laser ultrasonic method was used as a non-contact with high accuracy measuring technique to detect change in elastic modulus during pulsing. Joule heating effect on elastic modulus was also considered separately by measuring a linear dependence on elastic modulus with increasing temperature.

Under the various electric current density conditions, electric current 'itself' effect in electroplasticity was investigated. Measured elastic modulus during applying electric current includes mainly two effects. One is the joule heating effect and the other is electric current 'itself' effect. All measured elastic modulus are lower than that of calculated elastic modulus considering the joule heating effect in both aluminum and magnesium alloy. In other words, electric current can induce additional decrease in elastic modulus more than joule heating effect. It means that when electric current is applied, the change of lattice potential energy and curvature of the potential energy curve can be more intensified to the direction of weaken the elastic modulus in comparison with the change of lattice potential energy due to temperature effect. When the

potential energy curve is changed in the way of lowering the elastic modulus additionally as distinct from joule heating effect, the atomic bonding energy can be decreased which results in easy state to diffuse. Therefore, it can be suggested that electric current can induce the additional change in lattice potential energy and curvature of the potential energy curve with a discrete effect of joule heating, which can cause the enhance of diffusion by weakening the atomic bonding force.

Also, effect of grain boundary on electric current ‘itself’ effect in electroplasticity was studied for each alloy with different grain size of specimen. By comparing the normalized elastic modulus using two different grain sized specimen for each alloy, the decrease in elastic modulus by applying electric increases with increasing the fraction of grain boundary in both aluminum and magnesium alloy. In addition, this effect of grain boundary on decrease in elastic modulus is intensified by increasing electric current density. From these results, it can be said that the grain boundary is dominantly influenced by applying electric current to decrease in elastic modulus, even though the volume fraction of grain boundary in bulk sized specimen is quite small as  $10^{-3}$ - $10^{-1}$  %.

This study provides an important insight to apply electric current-assisted forming. As a positive aspect, electric current-induced annealing makes material experience recovery during deformation by applying electric current, which can enlarge the capacity for deformation. Electric current-induced aging

also occurs during plastic deformation with less time and lower temperature compared to conventional aging condition. However, electric current can accelerate the formation of microvoid around the particles, which results in earlier fracture as a negative way in formability. Therefore, electric current should be carefully applied to material considering the microstructural features to obtain enhanced formability without degradation of mechanical property.

From this study, electroplasticity in lightweight alloy was investigated well. Also, the underlying mechanism of electroplasticity, which has not been clear up to now, is suggested. The discussion on electroplasticity and suggested underlying mechanism can provide insight to apply electrically-assisted manufacturing in real industry as well as academic interests for electroplasticity.

## 국문 초록

통전 성형법 (Electrically-assisted manufacturing, EAM)은 소재의 변형 중에 전류를 인가함으로써 일반 변형 대비 향상된 연신율과 낮아진 유동응력을 이용하여 소재의 성형성을 획기적으로 향상시킬 수 있는 신 성형 기술이다. 전류 인가에 의한 향상된 연신율과 낮아진 유동응력의 현상은 ‘electroplastic effect’라 일컬어 지며, 성형 공정 외에 굽힘, 압출, 압연 등의 공정에 광범위하게 활용이 가능하다는 점에서 가능성이 무궁무진한 기술이라 할 수 있다.

자동차 업계에서는 경량소재의 적용비율을 넓혀가고자 하는 노력이 행해지고 있으나, 알루미늄과 마그네슘 합금 등의 소재들은 일반적인 철강 소재에 비해 상온 성형능이 현저히 떨어진다는 단점이 존재한다. 따라서 이러한 소재에 통전 성형법을 적용하면, 상온 성형능을 현저히 향상시킬 수 있다는 장점이 존재할 뿐만 아니라 기존의 고온 공정에서 존재하는 단점들, 예를 들면 고온으로 열처리 노를 승온시키기 위해 발생하는 고비용의 문제 및 고온에서 장시간 열처리로 인해 발생하는 표면 산화의 문제 등을 극복할 수 있는 장점을 가지고 있기 때문에 통전 성형법은 타 성형법의

대안으로 떠오르고 있다.

이러한 통전 소성 효과 즉, 'electroplastic effect' 는 1959년 미국의 Machlin 에 의해 처음 보고가 되었으며, 최근에는 통전의 효과를 이용한 실용화를 위한 연구 및 통전 메커니즘에 대한 연구가 활발히 행해지고 있다. 통전 메커니즘은 현재 크게 두 가지로 알려져 있는데 저항발열에 의한 것으로 보는 관점과 고전류밀도의 전류 인가로 인한 electron wind 가 원자의 이동을 촉진시킨다고 보는 관점으로 나누어 볼 수 있다. 하지만 통전의 메커니즘에 대해서는 학문적으로 아직 명확히 규명된 바가 없는 상황이다.

따라서 본 연구에서는 경량소재에서의 통전 소성 거동을 미세조직 분석 더불어 행하여, 다양한 실험적 방법으로 전류의 효과를 평가해 보았다. 또한, 현재까지 규명되지 않은 통전 소성의 메커니즘을 실험적으로 규명해 보았다.

먼저, Al-Mg 합금계에 대해 통전 인장을 진행하면서 기계적 거동을 분석하고, 미세조직 변화를 분석함으로써 non-heat treatable 알루미늄 합금재에 대한 통전 소성 효과를 분석하였다. 실험에서 선택된 전류 인가 조건에 의해 통전 인장 시의 연신율이 일반 인장 시의 연신율에 비해 약 3배 증가하였으며, 통전 인장 시

유동응력 또한 일반 인장 시에 비해 낮아지는 것이 관찰되었다. 이를 통해 전류 인가에 의해 소재 내부에 회복이 일어나고 있다는 것을 예상해 볼 수 있었고, EBSD (Electron Back-Scattered Diffraction) 를 활용한 미세조직 분석 및 온도 측정 결과를 통해 저항발열 만으로는 이를 설명할 수 없음을 확인하였다. 따라서 온도의 효과와 구분되는 전류 자체의 효과를 파악하고자, 동일한 변형이 인가된 시편에 통전 인장 시와 동일한 온도이력이 행해진 시편을 준비하여 경도 측정 및 XRD (X-ray diffraction) 의 반가폭 분석을 시행하였다. 그 결과, 소성 변형에 의해 생성된 전위들이 열처리에 의해 소둔이 되는 것이 확인되었지만, 통전 인장시의 시편에서 더 많은 전위의 소멸이 일어나는 것을 실험적으로 분명히 확인할 수 있었다. 이를 통해, 변형 시 전류가 인가되면 저항발열에 의한 현상과 구분되는 전류 자체의 효과로 인해 소재의 소둔 (Electric current-induced annealing) 현상이 일어날 수 있음을 증명하였다.

다음으로, Al-Mg-Si 합금계에 대해 통전에 의한 기계적 거동을 분석하고, 미세조직 변화를 분석함으로써 석출 경화형 알루미늄 합금계에 대한 통전 소성 효과가 분석되었다. 해당 소재에 대해서는 열처리를 각각 다르게 진행하여, 과포화상태의 시편 (solution

treated), 자연시효 상태의 시편 (naturally aged) 그리고 인공 시효 상태의 시편 (artificially aged) 을 준비하여 동일한 전류 조건을 인가하면서 전류의 효과를 평가해보았다. 그 결과, 자연시효된 시편의 경우 통전 인장 시 일반 인장에 비해 연신율이 약 1.5배 증가하고 유동응력이 낮아지는 등 앞서 Al-Mg 소재에서 관찰된 현상과 동일한 통전 소성 거동이 관찰되었으며, 반가폭 분석을 통해 출발열에 의한 소둔과 함께 전류에 의한 소둔 현상이 일어나고 있음이 확인되었다. 과포화 상태의 시편의 경우, 통전 시 일반 인장에 비해 연신율이 소폭 증가하였으며, 반가폭 분석을 통해 출발열에 의한 소둔과 함께 전류에 의한 소둔 현상이 관찰되고 있었는데, 그럼에도 불구하고 유동응력은 통전 인장 시 오히려 일반 인장에 비해 증가하는 것이 관찰되었다. 더불어 일반 인장 시에 관찰되는 PLC (Portevin-Le Chatelier) 거동이 통전 시에는 변형량이 증가함에 따라 약화되는 것이 관찰되었다. 이는 과포화상태 시편이 통전 인장에 의해 시효가 일어나고 있음에 기인하는 것으로 확인되었으며, 다양한 조건의 열처리를 진행한 시편과의 경도 비교를 통해 통전 인장 시 더 낮은 온도 및 더 짧은 시간으로도 시효가 일어난다는 것, 즉 전류에 의해 시효 거동이 가속화될 수 있음이 확인되었다. 인공시효된 시편의 경우, 통전

인장 시 전류에 의한 소둔 현상이 마찬가지로 관찰되었지만, 오히려  
파단 연신율은 일반 인장에 비해 감소하는 것으로 측정되었다. 파면  
분석을 통해 확인한 결과, 이는 인공시효된 시편의 결정립계에  
편석되어 있던 비금속 개재물 주변에 전류에 의해 공공 생성이  
가속화되는 것에 기인한 것으로 확인되었다.

마지막으로, 앞서 관찰된 통전 소성 거동 분석 결과를 바탕으로  
통전의 메커니즘이 규명되었다. 앞서 관찰된 통전 소성 거동 분석  
결과를 종합해보면, 전류 인가에 의해 저항발열과는 구분되는 전류  
자체의 효과로 원자의 확산 현상이 가속화 되는 것으로 정리해 볼  
수 있다. 확산 거동은 원자 간 결합에너지와 긴밀한 관계가 있으며,  
원자간 결합에너지는 포텐셜 에너지-원자거리 커브에서 포텐셜  
우물이 깊은 지점의 값을 의미한다. 이때, 포텐셜 에너지 커브를  
원자간 거리로 두 번 미분한 값은 탄성계수로 정의된다. 본  
연구에서는 전류 인가 시 탄성계수 값을 측정함으로써 역으로  
포텐셜 에너지 변화에 따른 원자간 결합에너지 값의 변화를  
추적하기 위해, 전류 인가 중에 소재의 탄성계수 변화를 측정해  
보았다. 알루미늄과 마그네슘 소재에 대해 전류 인가 중의 탄성계수  
변화를 측정해본 결과, 두 소재 모두 전류 인가 시 측정된 탄성계수  
저감이 저항발열에 의한 탄성계수 저감보다도 확연한 것을

관찰하였다. 이는 저항발열에 의한 원자 간 결합에너지의 저감보다도 전류가 인가되면 원자간 결합에너지가 더 낮아진다는 것을 의미하며, 결국 전류 인가 시 온도의 영향과는 구분되는 전류 자체의 영향으로 인해 확산 거동이 가속화 된다는 것을 실험적으로 증명한 결과이다. 더불어 두 소재에 대해 결정립 크기에 따른 탄성계수 변화를 관찰한 결과, 결정립 크기가 작을수록 전류에 의한 탄성계수 저감이 더욱 활발하게 일어나는 것을 확인하였다. 이를 통해 전류 인가 시, 결정립계 부근이 전류에 의한 확산거동 가속화에 주요하게 작용하는 것을 확인 하였다.

본 연구를 통해, 경량소재에 대한 통전 소성 거동이 미세조직 분석과 더불어 체계적으로 분석되었으며, 이를 바탕으로 아직까지 명확하게 밝혀지지 않았던 통전 소성 메커니즘이 규명되었다. 이를 통해 통전 소성 현상에 대한 근본적인 이해가 가능해 졌으며, 더욱이 본 연구를 통해 제안된 통전 메커니즘을 바탕으로 다양한 방면에 통전 현상을 적용함에 있어 충분한 통찰력을 제공할 수 있을 것으로 사료된다.

핵심어: 경량금속, 알루미늄 합금, 마그네슘 합금, 통전성형법, 통전소성, 1축 인장 시험, 유동응력, 연신율, 비커스 경도,

디지털이미지상관법 (Digital image correlation),  
후방산란전자선회절장치 (Electron backscatter diffraction),  
주사전자현미경 (Scanning electron microscope), 투과전자현미경  
(Transmission electron microscope), 집속이온빔 (Focused ion  
beam), X선 회절 (X-ray diffraction), 반가폭 (Full width half  
maximum), 초음파 측정법, 전위, 소둔, 회복, 재결정, 시효, 석출,  
파단, 공공, 저항발열, 포텐셜 에너지, 확산, 탄성계수, 결정립계.

**Student number: 2010-20579**